# ENABLING SOFT ROBOTIC SYSTEMS: NEW SOLUTIONS TO STIFFNESS TUNING, SENSING, AND ACTUATION CONTROL

By

Mohammed Al-Rubaiai

A DISSERTATION

Submitted to
Michigan State University
in partial fulfillment of the requirements
for the degree of

Electrical Engineering – Doctor of Philosophy

2021

## ABSTRACT

## ENABLING SOFT ROBOTIC SYSTEMS: NEW SOLUTIONS TO STIFFNESS TUNING, SENSING, AND ACTUATION CONTROL

By

Mohammed Al-Rubaiai

Soft robots have appealing advantages of being highly flexible and adaptable to complex environments. This dissertation is focused on advancing key enabling elements for soft robots, including providing new solutions to stiffness-tuning, integrated sensing, and modeling and control of soft actuation materials.

First, a compact and cost-effective mechanism for stiffness-tuning is proposed based on a 3D-printed conductive polylactic acid (CPLA) material. The conductive nature of the CPLA allows convenient control of temperature and stiffness via Joule heating in a reversible manner. A gripper composed of two soft actuators as fingers is fabricated to demonstrate localized gripping posture, passive shape holding, and the ability to carry load in a desired locked configuration.

Second, two types of integrated sensors are proposed. The first type is 3D-printed strain sensors that can be co-fabricated with soft robot bodies. Three commercially available conductive filaments are explored, among which the conductive thermoplastic polyurethane (ETPU) filament shows the highest sensitivity (gauge factor of 20) and working strain range of 0%–12.5%. The ETPU strain sensor exhibits an interesting behavior where the conductivity increases with the strain. In addition, the resistance change of the ETPU sensor in a doubly-clamped configuration in response to a wind stimulus is characterized, and the sensor shows sensitivity to wind velocity beyond 3.5 m/s.

We then present a soft pressure-mapping sensing system that is lightweight and low-cost, and can be integrated with inflatable or textile structures with minimal impact on the original substrate characteristics. The sensing system involves two layers of piezoresistive foil and three layers of conductive copper sheets, stacked on top of each other in an orderly manner, to detect the magnitude and the location of applied load, respectively. Extensive experiments on a sensor prototype with dimensions of 35×500 mm mounted on an inflatable tube are conducted to demonstrate

the capability of the proposed scheme in simultaneous measurement of deformation location and magnitude. In particular, it is shown that the specific design approach minimizes the coupling of location and magnitude measurements, resulting in minimal complexity for data processing.

Finally, we investigate the modeling and control of soft actuation materials, specifically accommodating their nonlinear dynamics. Polyvinyl chloride (PVC) gel actuators are considered in this work. A nonlinear, control-oriented Hammerstein model, with a polynomial nonlinearity preceding a transfer function, is proposed to capture the amplitude and bias-dependent frequency response of PVC gel actuators. A trajectory-tracking controller is developed, where an inverse is used to cancel the effect of the nonlinearity and a disturbance estimator/compensator is adopted to mitigate the influence of model uncertainties and disturbances. The efficacy of the proposed modeling and control approach is demonstrated experimentally in comparison with alternative methods, where the PVC actuator is commanded to track references of varying frequencies and waveforms.

*To my beloved parents*

## ACKNOWLEDGEMENTS

I would like to express my deepest gratitude to my advisor Professor Xiaobo Tan at Michigan State University for his guidance, caring, and patience, and for providing me with an excellent atmosphere for this work. He consistently steered me in the right direction whenever he thought I needed it.

I want to thank all my Ph.D. committee members: Professors Nelson Sepulveda, Tong Gao, and Wen Li at Michigan State University, for kindly joining my advisory committee and offering me insightful comments. I also thank our research collaborators, Zachary Frank and Professor Kwang J. Kim at University of Nevada, Las Vegas for their support and kind help in my research projects. I also want to acknowledge the funding support from Toyota Motor North America and MSU Foundation Strategic Partnership Grant Program (16-SPG-Full-3236) that made this work possible.

I am grateful to my friends at Michigan State University and my fellow labmates at Smart Microsystems Lab for their support, friendship, memories, and all the fun we have had in the last few years.

Finally, and most importantly, I would like to express my most profound gratitude to my parents for their endless love, consistent support, and encouragement throughout this research.

## TABLE OF CONTENTS

## LIST OF TABLES

## LIST OF FIGURES

# CHAPTER 1

# INTRODUCTION

The tight integration of sensing, actuation, and computation that biological systems exhibit to achieve shape and appearance changes (like the cuttlefish and birds in flight), adaptive load support (like the banyan tree), or tactile sensing at very high dynamic range (such as the human skin) has long served as inspiration for engineered systems. Soft robotics is an emerging field of robotics, and the key idea is to ensure that all the structural components in the robot are soft and flexible, to safely interact with living systems and function in complex and unconstrained environments. This field requires interdisciplinary research spanning areas such as materials science, control theory, flexible electronics, sensing, and energy storage. Soft robotics holds promise for various applications, such as industrial gripping, surgery, and assistive healthcare devices. In this chapter, the challenges of achieving stiffness tuning, soft/flexible sensing, and dynamic modeling and control for soft robotics are discussed. The state of the art in these areas is surveyed, followed by a summary of contributions.

## 1.1 3D-printed Stiffness Tuning Material

### 1.1.1 State of the Art

Rigid materials are used by engineers to build accurate, stable robotic systems, which are readily modeled as rigid members connected by joints. Soft and deformable structures found in nature, however, often outperform these rigid systems. The latter observation has inspired engineers to investigate the design and control of soft-body robots made from compliant materials [2]. Mechanisms with controllable, variable stiffness are of interest in soft robotic systems since they will allow components, such as a robotic joint, to soften actively and thus enable adaption to a wide range of tasks [3], [4]. Stiffness tuning can be used for adaptive vibration-damping [5], precise control of joints for manipulators [6], and mechanical modulation of cell growth [7]. The change

of stiffness can also be used for universal orthopedic casts, customized seatings, and adaptive, aerodynamic surfaces [8].

There have been a number of approaches reported for stiffness tuning, several of which involve the change of pressure input in pneumatic or hydraulic actuation. For example, compliance change for a McKibben actuator was realized via the switching of pneumatic and hydraulic actuation modes [9]. Another notable pneumatic approach to stiffness tuning is based on the jamming of granular material or thin sheets. Jamming is typically activated via the application of vacuum, which increases the relative shear stress experienced by the particles or layers within elastic membranes [10–12]. The ability to deform in the fluid state and the highly increased stiffness in the solid-state without a significant volume change makes particle jamming an intriguing approach [13]. However, it requires a large volume of granular material to achieve high stiffness variation. In comparison, layer jamming represents a better alternative for large-surface robots, where the application of vacuum results in increased friction between overlapping surfaces of a large contact area [13], [14]. One disadvantage of the aforementioned approaches is their requirement of the pneumatic or hydraulic source and valves, which increases the size and complexity of the overall system.

Several studies on tunable stiffness have used the thermoplastic properties of shape memory polymers (SMPs). A variable-stiffness fabric for wearable applications was presented in [15], which was made of shape memory alloy (SMA) wires coated with a thin film of SMP, where the transition from the glassy state to the rubbery state was accomplished by direct Joule heating of the embedded SMA wires. A 3D-printed SMP was used in [16] as an embedded layer in a silicone-based soft actuator to modulate the stiffness at three independent positions with external heating elements. The same group also demonstrated a 3D-printed multi-material substrate [17], composed of SMP and conductive elastomeric thermoplastic polyurethane (TPU), where the conductive TPU served dual purposes of Joule heating and providing feedback of the bending angles for the soft actuator joints. Another approach using conductive polymer for stiffness tuning was explored by mixing propylene and carbon black to form so called conductive propylene-based elastomer (cPBE) [18].

### 1.1.2 Contribution

Compared to the state of the art reviewed above for stiffness tuning, the contribution of this work is the proposal of a cost-effective (3D-printable with inexpensive printers), compact mechanism (electrically activated, exploiting the inherent thermoplastic property and Joule heating capability of the printed material without additional elements for stiffness tuning, and its application to shape modulation for soft actuators. For the latter, we further show that the desired shape, with load-carrying capability, can be maintained even if the actuation inputs are turned off. Specifically, the proposed approach exploits a conductive polylactic acid (CPLA) material, readily printed with a FDM (Fused Deposition Modeling) 3D printer. The conductive nature of the material allows thermal activation through Joule heating. The CPLA shows 98.6 % reduction of Young's modulus, from 1 GPa at room temperature (which is about 25 °C) to 13.6 MPa at 80 °C, which is fully recovered when it is cooled down to its initial temperature. The material has a glass transition temperature (Tg) of 55 °C, at which the Young's modulus is at 60% of the value at the room temperature. Systematic experiments are conducted to characterize the thermal, mechanical, and electrical properties of the CPLA. These properties are then used in finite element simulation to predict the thermal and mechanical behavior of the CPLA sheet under an applied voltage, and in the simulation of a soft pneumatic actuator embedded with a CPLA layer. The simulation results are validated against experimental data from a soft pneumatic actuator that has three stiffness-controlled joints enabled by CPLA. Finally, a two-finger gripper, made of two soft actuators with stiffness and shape tuning, is fabricated to demonstrate gripping objects of different sizes and shapes. Once a desired posture of the gripper is attained, one can turn off the Joule heating and let the CPLA cool down. Then the stiffness of the CPLA at room temperature is shown to enable shape-holding and load-carrying for the otherwise soft actuator even when the pressure input to the pneumatic actuator is turned off. Specifically, one actuator is shown to hold a maximum load of 800 g in the absence of pressure input.

## 1.2 Flexible and Stretchable Soft Sensor

### 1.2.1 State of the Art

Strain sensors, traditionally fabricated from metals or semiconductors, are devices that can convert mechanical deformation to measurable signals [19] and are widely used for detecting material fatigue in bridges, airplanes, and rails [20, 21]. To overcome the rigidity and limited sensing range for traditional strain gauges [19], new types of strain sensors have been designed for flexible textile materials to be used in wearable applications. Sports clothing that can track body movements [22, 23], remote health monitoring [24, 25], and soft robotics [26] are some application areas to date.

In soft robotics, highly deformable elastomers are widely used for developing stretchable sensors [27–29] and compliant actuators [30, 31]. Robots may increase their safety levels when combined with these types of soft components [32]. It is possible to make the structures of robots entirely of soft materials, as shown for soft manipulators [33–35] and wearable robots [36–38]. Another approach is to cover or build either designated parts or the entire robot body using inflatable structures. Ohta et al. have proposed such methods by using inflatable sleeves made of heat sealable polymer materials to cover the rigid bone structure of a robotic arm [39]. Qi et al. have developed lightweight inflatable arms for interactive robots [40], and Hawkes et al. have also used an inflatable structure for the extension and navigation of a robotic arm [41]. Although the above approaches provide a certain level of structural safety, most of them lack the capability to directly sense external contacts through their body structures, which would significantly increase robot responsiveness and autonomy through control.

3D-printable components with embedded sensing capabilities have the potential to be incorporated into a vast array of applications. Structures that can sense damage and predict failure, and airfoils that can change their aerodynamic profile are just two examples of many potential applications that have been proposed [42]. Embedded electronics facilitate the ability to manufacture devices with profound capabilities in a number of industries. Devices fabricated for specialized ap-

plications can be produced easily and effectively using conductive materials that can be embedded during the 3D printing process [43]. The incorporation of electronic functionality into 3D-printed parts using conductive filament material has allowed researchers to fabricate a variety of embedded sensors that can be incorporated into specimens with surfaces that would not allow for gauge installation [44]. The ability to 3D-print strain gauges into surfaces where gauge installation would be difficult makes embedded sensors applicable to more specialized applications than traditional strain sensors. By way of 3D printing, there is no need to install sensors on an object's surface since it is built directly into it as it prints. Eliminating the need for installation can help to eliminate errors that can arise from improper sensor installation.

### 1.2.2 Contribution

In this work, we propose two types of soft, flexible sensors. First, a material extrusion−based 3D printing technique with a dual−extruder configuration is presented for fabricating soft sensors directly with a bottom−up approach, which is expected to be lightweight and low−cost. In particular, soft strain sensors are printed through dual−extrusion, one for the conductive sensing element and the other for a hyper−elastic substrate. This technique does not involve any core to define and mold the geometry, and it facilitates the rapid customization of the sensor geometry by adjusting the printing parameters in the 3D printing software. Comparing to more advanced multi−material 3D−printers (such as the Connex series of Objet), material extrusion−based printers are much more affordable, with a larger array of material choices. Three different commercially available conductive filaments, Conductive Graphene PLA from Graphene 3D Lab, USA, Conductive PLA from Proto-Pasta, USA, and ETPU from Rubber3D Printing, Sweden, are used to fabricate stretchable strain sensors, which are subsequently characterized for extensibility and strain−sensing performance. These strain sensors show different limits in strain measurement from 6% to 25% with gauge factors ranging from 0.2 to 20. The sensor with the highest sensitivity, made from a conductive thermoplastic polyurethane ETPU, is used in a case study in a doubly−clamped configuration, to characterize the sensor output (resistance change) as the wind speed is varied in a wind tunnel.

Finite element method (FEM)−based modeling is further conducted on the wind sensor to compute the sensor strain distribution under different wind speeds, where experimentally characterized material stiffness values are used. Along with the characterized resistance−strain relationship, the modeling is shown to be capable of predicting the measured sensor output. This work thus shows the feasibility and promise of the proposed 3D-printed soft strain sensors.

Second, we propose using conductive materials and piezo-resistive films for fabricating flexible pressure mapping sensors that are lightweight and low-cost and can be integrated into inflatable or textile structures with minimal impact on the original substrate characteristics. Five different commercially available conductive plastic films are used to fabricate flexible kink sensors as a case study for inflatable devices. These flexible kink sensors show different sensitivity levels with kink measurement limits from 0-10 mm. The sensor with both high sensitivity and good stability, made with scs-1704 conductive film from Static Control, USA, is used for deformation localization and magnitude measurement in inflatable tube experiments. In particular, for a given deformation, the sensor output shows a monotonic relationship with the location and magnitude of the deformation and, thus, enabling the monitoring of the entire tube with a single sensor.

## 1.3 Polyvinyl Chloride (PVC) Gel Actuators: Characterization, Modeling, and Control

### 1.3.1 State of the Art

Soft actuators based on smart materials have been widely studied owing to their flexibility, compactness, and great potential in various applications [45–47]. As one type of electroactive polymers, Polyvinyl chloride (PVC) gel actuators exhibit attractive performance in displacement output, force output, response speed, and behavioral stability, which make them a promising artificial muscle technology [48–51], with application to optical focusing lenses, wearable assistive spats, tactile display, vibrotactile actuator, and micro gripper among others [52–56].

With the development of different structures and configurations for PVC gel actuators, underlying actuation mechanisms for PVC gels have been explored. The polarity of the PVC and

the plasticizer (typically, dibutyl adipate, or DBA) molecules allows them to rearrange and move under an electric field, generating the electrophoresis current from charge injection [57]. The close relationship between the formation of a plasticizer-rich layer and the gel creeping motion around a mesh-structured anode under an electric field is discussed [51]. Based on these assumptions and explorations, several analytical models have been proposed, including a bending deformation model with solvent-rich layer formation theory [58], a model for contraction type PVC gel actuator with equivalent circuit analysis [59], a force and deformation model based on Hill's muscle model [60], and an electromechanical model for PVC gel actuator with addition of ionic liquids [61]. Moreover, a numerical model has been developed by using the Maxwell stress tensor and nonlinear elastic material models for FEM simulations of the PVC gel actuators [62]. While these models are generally instrumental in predicting static deformation and force output of PVC gel actuators, little work has been reported on modeling nonlinear dynamic behavior for these actuators. Such models will be important for effective design of controllers for PVC gel actuators in their versatile applications.

### 1.3.2 Contribution

In this work, we present a data-driven modeling approach to capture the observed nonlinear dynamics of PVC gel actuators, where the voltage input – displacement output frequency response shows pronounced dependence on the input amplitude and bias. A Hammerstein-type model is proposed, where a polynomial nonlinearity precedes a linear system, and the identification procedure for the model is presented. In particular, the linear system is identified based on the empirical frequency response of the actuator at a relatively low input amplitude, and the coefficients of the polynomial nonlinearity are determined via a least-squares minimization procedure. The effectiveness of the proposed nonlinear model is supported by its capability to predict the experimentally observed dynamic responses under inputs of different amplitudes and biases. Finally, a trajectory-tracking controller is developed, where an inverse is used to cancel the effect of the nonlinearity and a disturbance estimator/compensator is adopted to mitigate the influence of model uncertainties and disturbances. Experimental results show the proposed controller outperforms the PID controller

and the controller combining PID and inverse compensation (but without disturbance rejection). From experiment, the average tracking error is reduced by (60.84%) from PID to inverse/PID, and by (82.7%) from PID to inverse/PID/disturbance-rejection.

# CHAPTER 2

## SOFT ACTUATORS WITH STIFFNESS AND SHAPE MODULATION USING 3D-PRINTED CONDUCTIVE PLA MATERIAL

In this chapter a compact and cost-effective mechanism for stiffness-tuning is proposed based on a 3D-printed conductive polylactic acid (CPLA) material, and its potential in soft robotics is demonstrated via a soft pneumatic actuator capable of stiffness and shape modulation. In particular, the conductive nature of the CPLA material allows convenient control of temperature and stiffness via Joule heating. Mechanical, thermoplastic, and electrical properties of the CPLA are first characterized. The experimentally identified material parameters are then used in finite-element modeling and simulation to investigate the behavior of a soft pneumatic actuator integrated with a CPLA layer. A soft actuator with three virtual joints enabled by CPLA is prototyped, and bending experiments are conducted to both demonstrate the effectiveness of stiffness tuning and shape control and support the efficacy of the finite element model. Finally, a gripper composed of two soft actuators as fingers is fabricated to demonstrate localized gripping posture, and the ability to carry load in a desired locked posture even when the pressure input is turned off, after the CPLA is cooled down. This work was co-authored with another researcher from my lab, Thassyo Pinto. He fabricated the soft pneumatic actuator and the gripper that were used as a case study in this chapter and helped with the bending and gripper experiments.

This chapter is organized as follows. The fabrication of CPLA and its integration with a soft actuator are first presented in Section 2.1. Experimental characterization of the relevant CPLA properties is discussed in Section 2.2. Finite element modeling and simulation of the CPLA and the soft actuator embedded with CPLA are described in Section 2.3, followed by experimental validation of the model in Section 2.4. Additional experimental results on gripping and load bearing are presented in Section 2.5. Finally, concluding remarks are provided in Section 2.6.

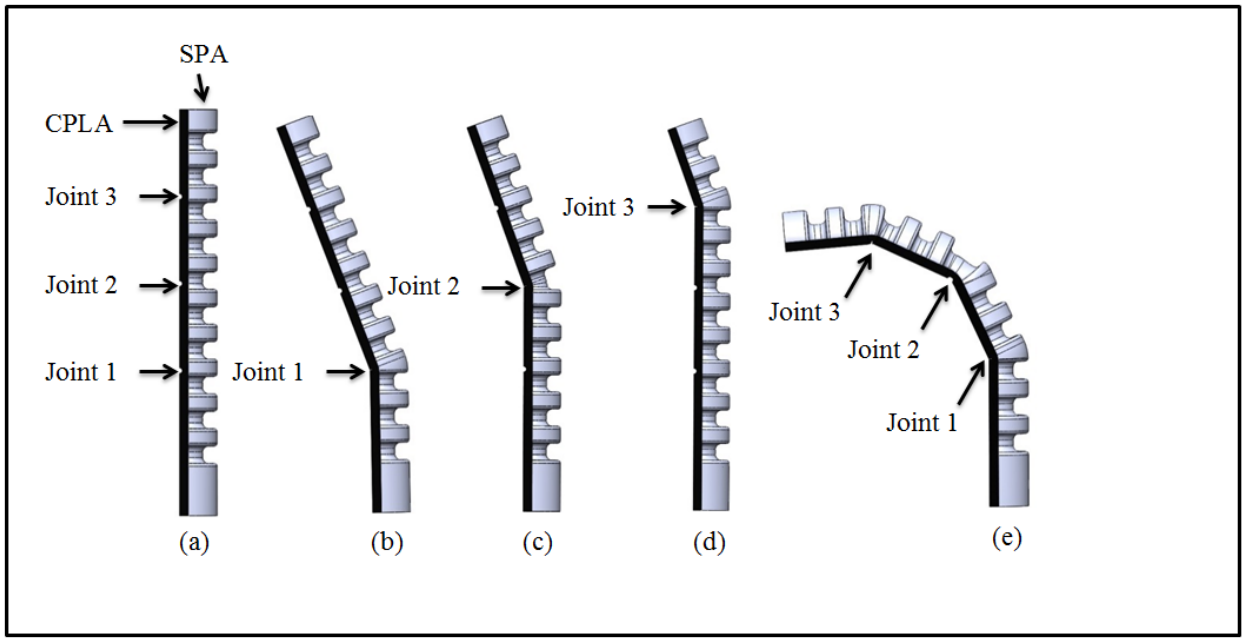


**Figure 2.1:** Illustration of the operating principle of CPLA-enabled soft actuator with stiffness and shape turning : (a) Main components of the actuator; (b) Actuator bending at Joint 1 when Joule heating is applied at location 1; (c) (c) Actuator bending at Joint 2 when Joule heating is activated at location 2; (d) Actuator bending at Joint 3 when Joule heating is activated at location 3; (e) Actuator bending at all joints when Joule heating is applied at locations 1, 2, and 3.

## 2.1 Fabrication of CPLA and Its Integration with a Soft Actuator

Figure 2.1 illustrates how CPLA is used to modulate the stiffness and bending shape of a soft pneumatic actuator (SPA). The CPLA layer is bonded to the flat side of the SPA. At the room temperature, due to the stiffness of CPLA, the SPA will not bend even when the pressure input is turned on. When Joule heating is activated at a given location on the CPLA, the material nearby softens and thus enables bending at that location, which essentially becomes a tunable "joint" or "hinge". The overall bending shape of the actuator can be tuned by controlling the CPLA temperature at different locations. The soft actuator can only bend at the joints due to their lower stiffness.

Figure 2.2 shows the fabrication process for the soft actuator with tunable stiffness and shape. The components are fabricated using two different procedures: casting and 3D printing. A casting process (silicone molding) is used for fabricating the SPA structure (Dragon Skin 30, Smooth-On)

in 3D-printed resin-based molds (Form 2, Formlabs). The SPA has a round profile shape (10 mm radius; 140 mm length) with topographical features, allowing fast actuation with low pressures values [63]. A thin layer of silicone is applied to the SPA bottom surface and cured for covering the hollow chambers and enabling fluidic actuation. In order to modulate the stiffness of the SPA, a flat sheet made of CPLA (CDP11705, Proto-pasta) is integrated to the device. Local indentations are designed in the flat sheet geometry to facilitate bending at the hinge locations. Since the material is supplied as a filament, a fused deposition modeling (FDM) 3D printer (QIDITECH I, QIDI Technology) is used to fabricate the conductive sheet.

Thin copper wires are soldered to each hinge using silver paste (Silver Conductive Wire Glue, Amazon), without affecting the device flexibility. The CPLA sheet is encapsulated through a silicone rubber bath to allow adhesion with the SPA. A single rectangular (20 mm $\times$ 140 mm) silicone sheet (2 mm thickness) is placed inside a glass container with the CPLA sheet laying on top. The silicone mixture is poured inside the container up to a margin of 2 mm above the CPLA sheet. The SPA and encapsulated CPLA are bonded together using uncured silicone. In order to prevent slippage during grasping experiments, an additional anti-slip feature enabled with surface texture is included in the design of the SPA-CPLA. This component is molded with the same silicone material as the SPA. Figure 2.3 shows the picture of a fabricated prototype. The dimensions of all parts in the actuator are listed in Table 2.1.

**Table 2.1:** The dimensions of parts in the fabricated SPA with embedded CPLA.

| Parameter | Dimension (mm) |
|---|---|
| SPA length | 140 |
| SPA width | 20 |
| SPA wall thickness | 2 |
| CPLA length | 135 |
| CPLA width | 16 |
| CPLA thickness | 3 |
| Anti-slip feature thickness | 2 |

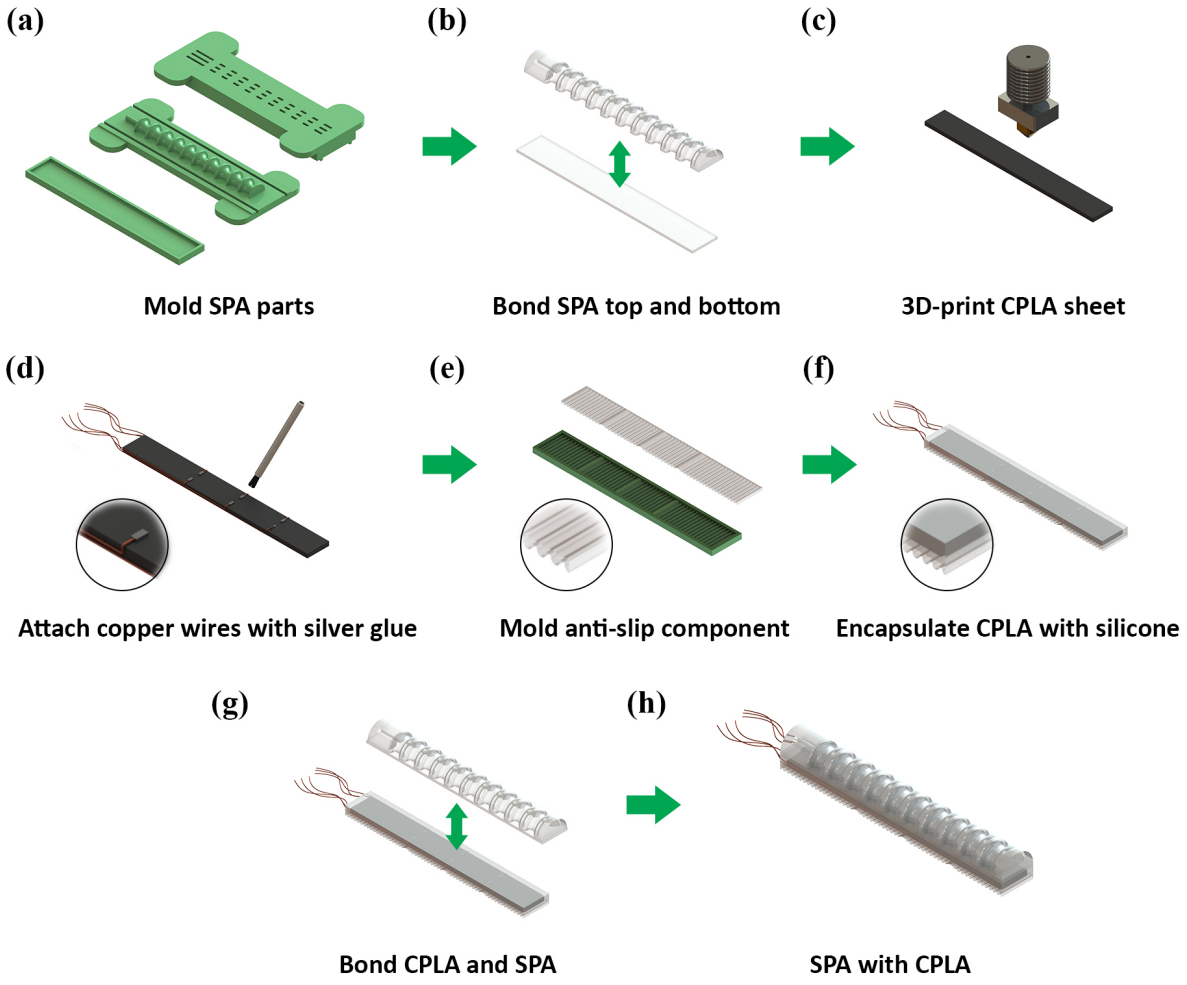


**Figure 2.2:** Fabrication of the SPA with a CPLA sheet integrated to its bottom layer. (a) 3D-printed mold parts for fabricating the SPA components; (b) Following curing, the upper and bottom parts of the SPA are bonded together; (c) The CPLA is 3D-printed using an FDM 3D-printer; (d) Thin copper wires are glued to the CPLA using a silver paste; (e) An anti-slip feature to prevent slippage during grasping; (f) The CPLA is encapsulated with uncured silicone; (g) The SPA and the encapsulated CPLA are bonded to complete the fabrication.

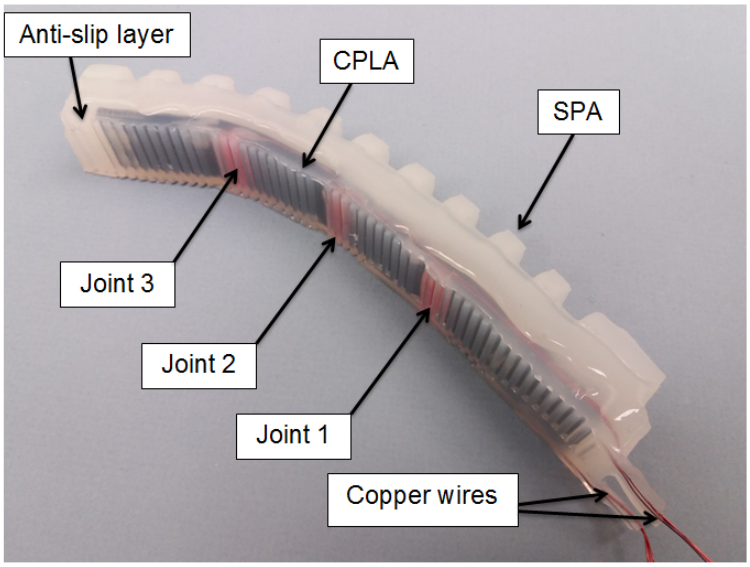


**Figure 2.3:** A fabricated soft pneumaric actuator (SPA) prototype with an embedded CPLA layer.

## 2.2 Characterization of the Thermomechanical Properties of CPLA

In this section, the thermal, mechanical, and electrical properties of 3D-printed CPLA samples are characterized, for the purpose of modeling, simulation, and analysis that will be presented in later sections.

### 2.2.1 Glass Transition Temperature

The glass transition temperature (Tg) is an important thermal property of polymers. The usual state of most polymers is hard and brittle at the room temperature and soft at the temperatures above Tg [64]. Differential scanning calorimetry (DSC) Q2000 from TA Instruments, Wilmington, DE, was used for determining the phase transition of the CPLA material. The following temperature conditions were used: heating from 35 °C to 185 °C at a rate of 10 °C/min. The DSC curves for the test sample of the CPLA are shown in Figure 2.4. A phase transition that sets in at 55 °C during the heating corresponds to the glass transition process when the polymer transforms to the highly elastic state. Two endothermic peaks observed at 124.4 °C and 154 °C correspond to melting [65].

Different melting temperatures were also observed in [66] due to the variation of size and level of perfection of the crystalline lamellae.

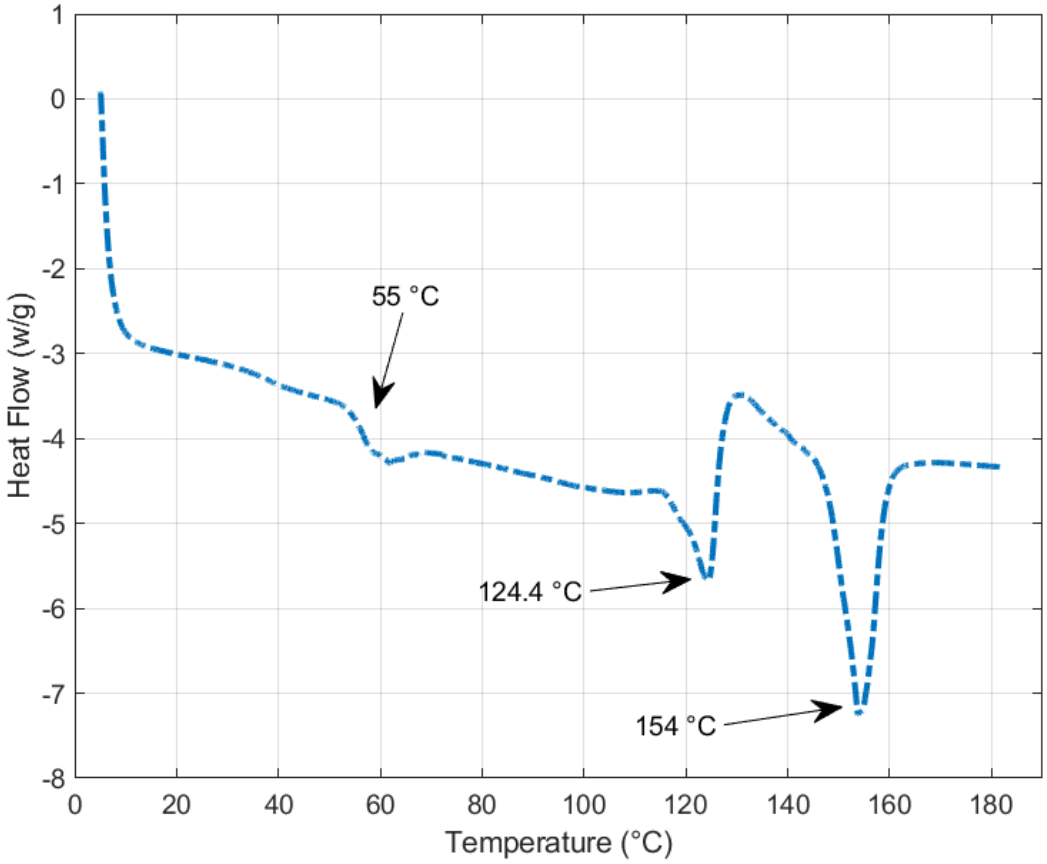


**Figure 2.4:** Differential scanning calorimetry (DSC) curve for the CPLA [1].

### 2.2.2 Temperature-dependent Stiffness

The stiffness of CPLA can be modulated with temperature. To measure the decrease in stiffness as a function of temperature, the tensile testing machine model SFM-20 (United Testing Systems inc., USA ) was used. The Young′s modulus at different temperatures (25 °C, 35 °C, 45 °C, 50 °C, 55 °C, 60 °C, 65 °C, 70 °C, 75 °C, 80 °C ) was measured. The specimen geometries followed specifications outlined in ASTM D-638 for the Type I tensile specimens. All samples were printed with a thickness of 2 mm. A loading rate of 3 mm/min was selected for all tensile tests. The

tension specimens were tested in batches of five for each temperature point, and the values of the Young′s modulus were averaged over the five trials. The Young′s modulus was calculated from the stress-strain ratio below the proportional limit of the material. One stress-strain graph under all ten temperatures is shown in Figure 2.5. Figure 2.6 shows the decrease of Young′′s modulus with temperature where a significant drop in modulus in the range of (55 - 70)°C is observed. This temperature range correlates to the region where the molecules undergo a transition from the glassy state to the rubbery state.

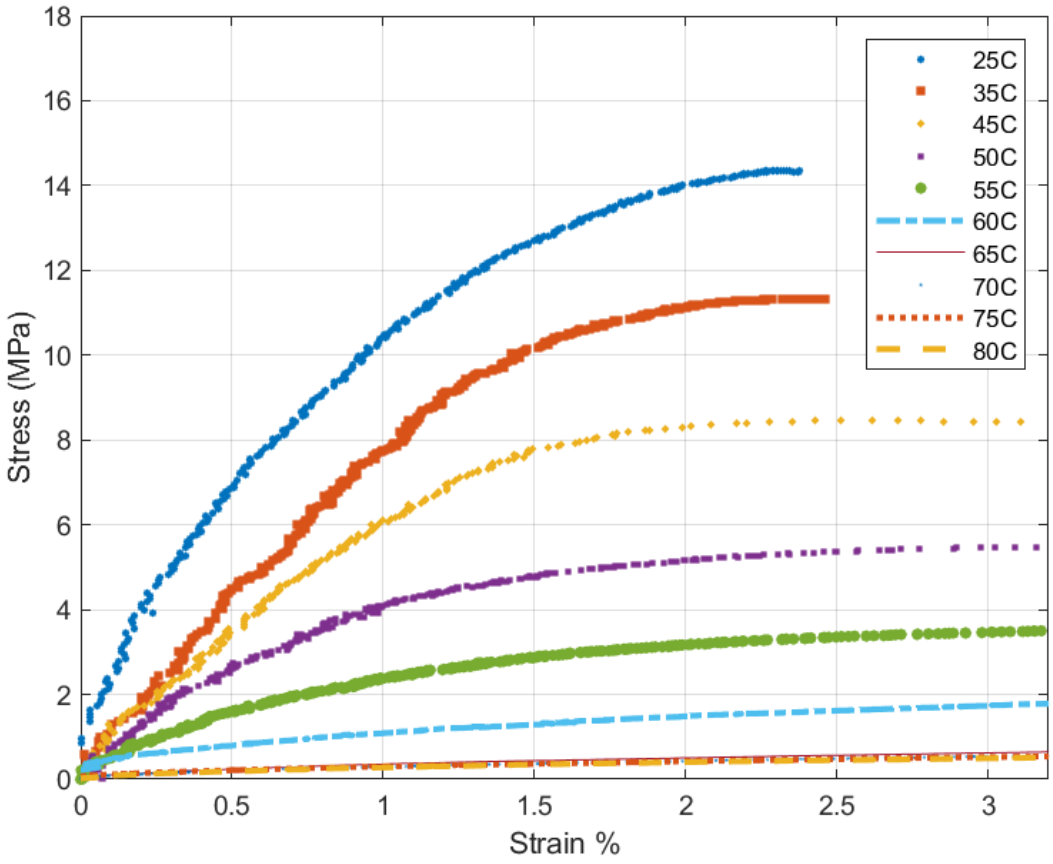


**Figure 2.5:** Stress-strain curves for all temperature points [1].

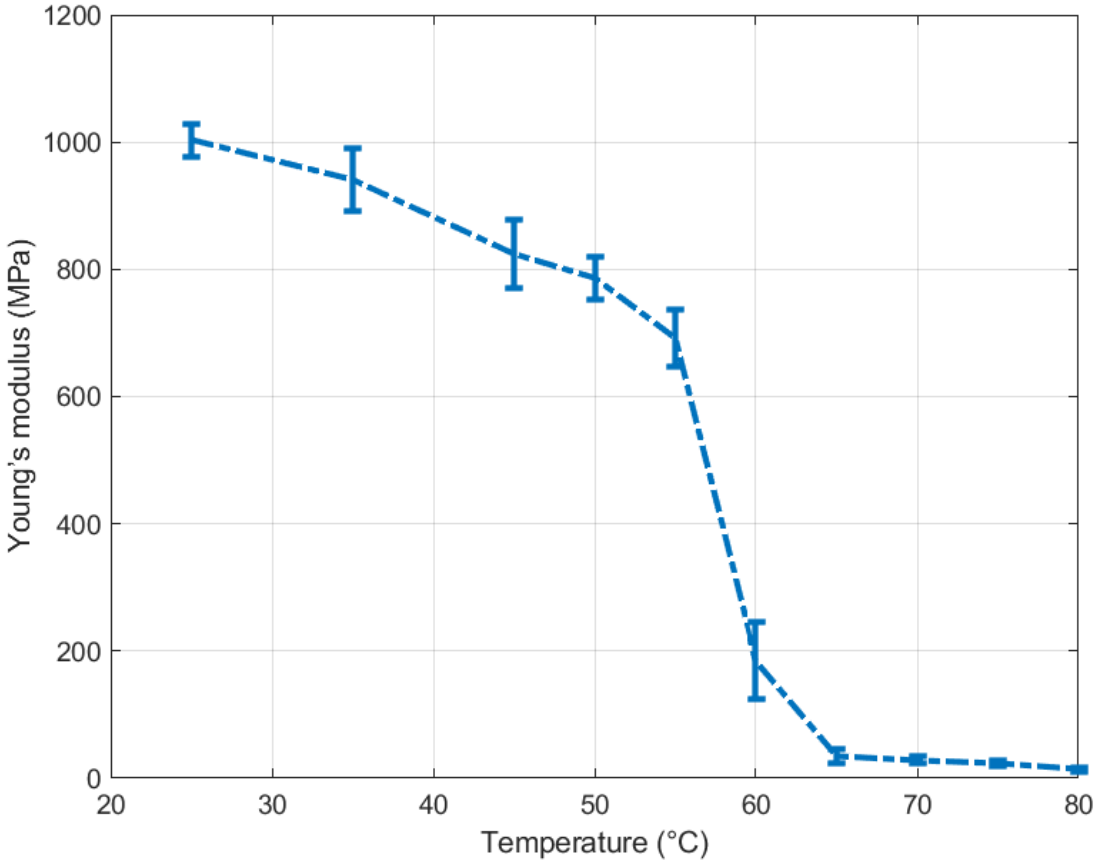


**Figure 2.6:** The decay in Young′s modulus as a function of temperature [1].

### 2.2.3 Thermal Expansion Coefficient and Thermal Conductivity

Thermomechanical analysis (TMA) is a widely used technique to measure dimensional changes of solid or liquid materials as a function of temperature. This method can be used to measure the coefficient of thermal expansion (CTE) for polymers [67]. TMA was performed with TMA Q400 from TA Instruments on samples with dimensions of approximately 12 mm × 12 mm × 1.7 mm. The samples were tested from the room temperature to 80 °C at a heating rate of 3 °C/min. Figure 2.7 shows an apparent change in slope at Tg, indicating an increase in thermal expansion coefficient above it. The coefficient of thermal expansion of the CPLA is the slope of the relative dimension change with respect to the temperature change divided by the initial sample height. The values of

the CTE below and above Tg are 169 $\mu$m/m°C and 420.16 $\mu$m/m°C, respectively.

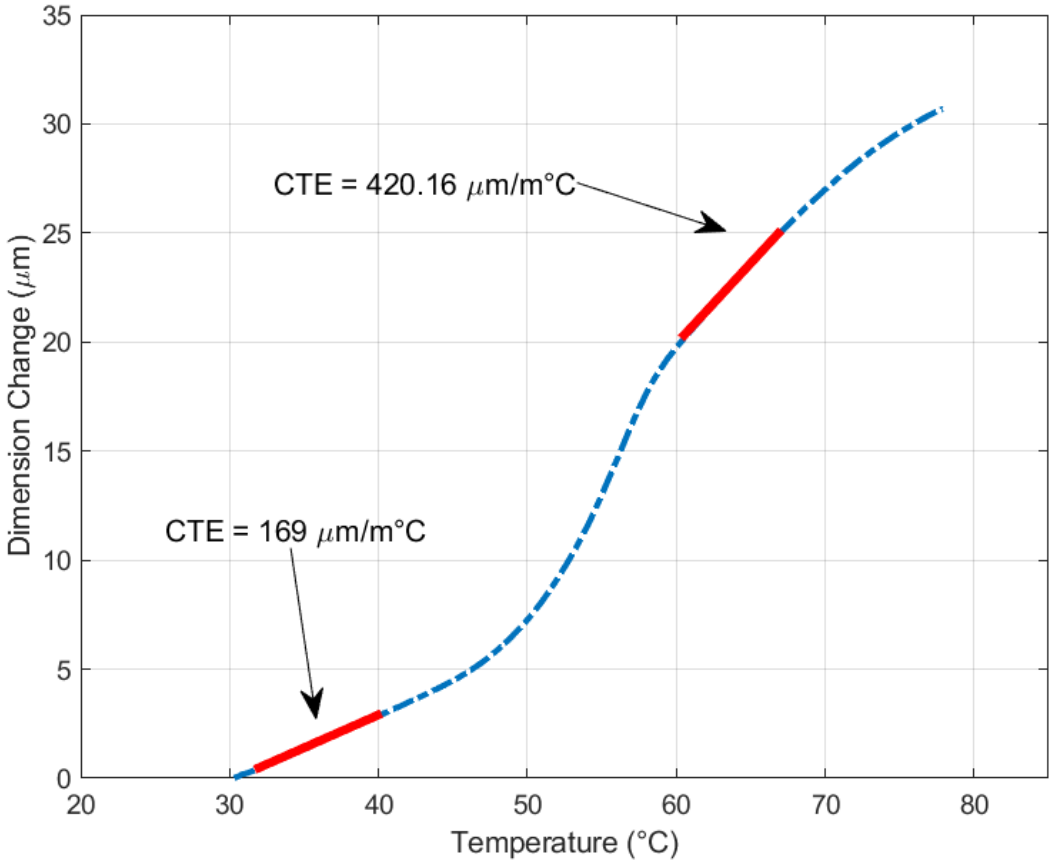


**Figure 2.7:** Thermomechanical analysis (TMA) curve for the conductive PLA [1].

Thermal conductivity describes the ability of a material to conduct heat. The instrument NETZSCH LFA 447 NanoFlash® was used to measure the thermal conductivity of the CPLA. Using the multi-property measurement capabilities of the NanoFlash®, both thermal diffusivity $a(T)$ and specific heat $c_P$ can be determined simultaneously on the same specimen, thus yielding thermal conductivity, $\lambda(T)$, if the density $\rho(T)$ is known:

$$\lambda(T) = a(T) \times c_P \times \rho(T) \tag{2.1}$$

The density of the conductive PLA is 1.21 g/cm$^3$. Three samples of dimensions 12 mm × 12 mm × 2 mm specimens were 3D-printed, and for each one, five measurements were taken. The

**Table 2.2:** Average thermal diffusivity and thermal conductivity values for three samples.

| Sample | Diffusivity $mm^2$ | Standard Deviation $mm^2$ | Specific Heat J/g· K | Thermal Conductivity W/m· K |
|---|---|---|---|---|
| 1 | 0.208 | 0.002 | 1.536 | 0.387 |
| 2 | 0.187 | 0 | 1.536 | 0.347 |
| 3 | 0.196 | 0.002 | 1.536 | 0.364 |

average of the five measured values for each specimen is shown in Table 2.2. It can be observed that for all the three cases the standard deviations were reasonably small.

### 2.2.4 Electrical Conductivity and Joule Heating

Since the proposed CPLA joints are activated electrically, it is of interest to characterize its electrical conductivity and understand the heating and cooling dynamics. Consider a rectangular CPLA sample, assumed to have a uniform temperature $\theta(t)$. A current $i$ is applied to the sample, passing through a (uniform) cross-section of area $A$ over a thickness of $d$. The temperature evolution of the CPLA can then be described with the following heat transfer equation for electrical heating [68]:

$$(\rho A d) C_p \frac{d\theta(t)}{dt} = i^2 R - h_c A_s [\theta(t) - \theta_\infty] \tag{2.2}$$

where $\rho$ is the density of the CPLA, $C_p$ is the specific heat. $R$ is the resistance, and $A_s$ is the surface area of the sample. The parameters $h_c$ is the heat transfer coefficient which is equal to the thermal conductivity divided by the thickness of the object [69]. The ambient temperature is denoted as $\theta_\infty$.

Experiments were first conducted to characterize the electrical resistance as a function of temperature. Figure 2.8(a) shows a schematic diagram of the experimental setup. A thermo-electrical generator (TEG) (model number CP081030-M, PELTIER) was used to control the temperature of the CPLA, and a resistance temperature detectors (RTD) (model number PTFM102T1G0, TE Connectivity) was attached to the CPLA sample with a thermally conductive paste for temperature measurement. The control of TEG and the data acquisition were coordinated with a microcontroller

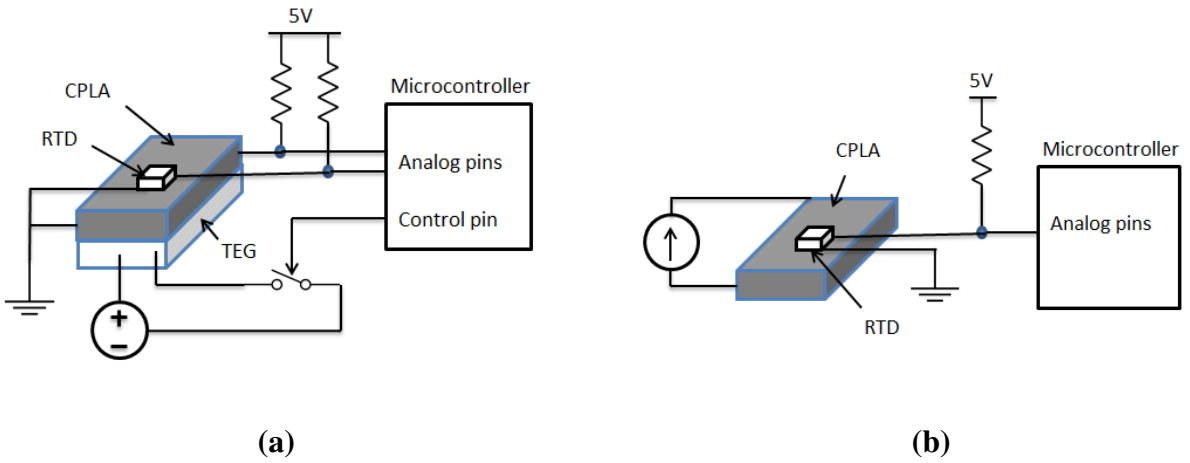


**Figure 2.8:** (a) Experimental setup for characterizing the temperature-dependent resistance of 3D-printed CPLA; (b) experimental setup for characterizing the speed of Joule heating and passive cooling of 3D-printed CPLA.

(model number A000073, Arduino). A CPLA sample with dimensions of 10 mm × 10 mm × 2 mm was used in this test. The samples were tested in the range from the room temperature to 55 °C. At each tested temperature, the resistance of the CPLA is measured with via a voltage divider circuit.

Figure 2.9 shows the measured resistivity as the temperature is raised and then lowered. One can see the hysteresis between the resistance and the temperature change, which is a nonlinearity commonly observed in phase-change materials. Since the hysteresis is relatively small, a linear fitting is found to capture the temperature-dependent resistivity, and such a linear approximation enables one to obtain an analytical solution to (2.2), which is important for computational efficiency of the model. The validity of the linear approximation is confirmed by the good fit between the experimental measurement and model prediction later shown in Fig. 2.10. The linear fitting between the resistivity $R_0$ and the temperature $\theta$ is as follows: $R = 0.01086\theta - 0.06138$.

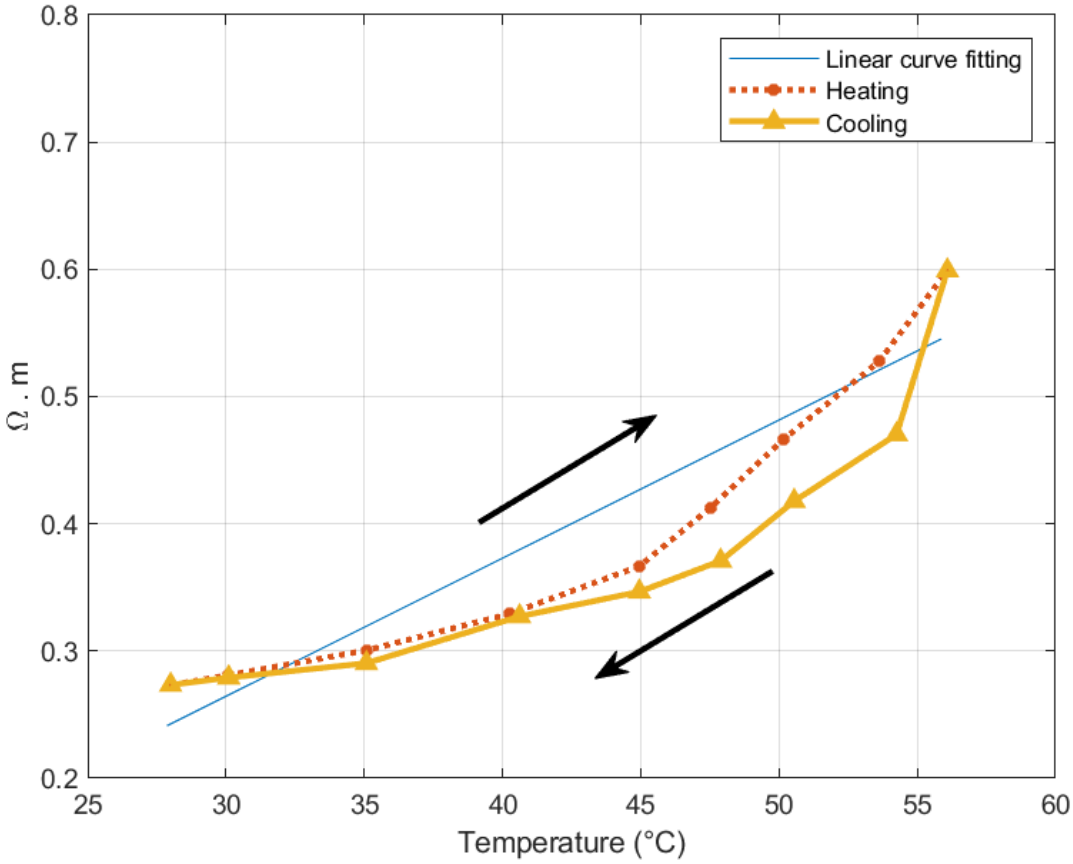


**Figure 2.9:** Measured resistivity of CPLA as the temperature is increased and then lowered. The linear line represents a linear approximation of the resistivity-temperature relationship.

Another test, with an experimental setup illustrated in Figure 2.8(b), was performed to measure the activation time for the CPLA to reach the glass transition temperature (Tg) in Joule heating, and the time it takes the CPLA to cool down passively to room temperature. For this purpose, a power amplifier (model number BOP 36-6D, KEPCO) was used as a current source. A current of 50 mA was applied to activate the CPLA while the temperature at the middle of the CPLA sheet was measured. Once the temperature reached the glass transition temperature (Tg), the current was turned off and the CPLA cooled down passively. This experiment was repeated five times. Figure 2.10 shows the evolution of the measured CPLA temperature along with the prediction from the model (2.2) during the heating and cooling process. It can be seen that, with

the experimentally characterized material parameters, the model is able to capture the heating and cooling behavior well. For this particular sample, passive cooling from the Tg to room temperature took approximately 120 seconds. While the heating speed can be controlled with the applied current, the cooling speed is limited by the speed of heat dissipation to the ambient environment The cooling speed, however, is a function of the geometry and dimensions of the CPLA sample. For example, Figure 2.11 shows the simulated cooling trajectories of CPLA samples of different thickness values, where the length and the width of each sample were fixed at 10 mm by 10 mm. From the figure, one can see that the cooling time could be significantly shortened with a thinner CPLA. For real robotic applications, proper dimensions of CPLA need to be designed to accommodate the corresponding load-bearing and speed requirements. For speed-critical applications, one could potentially adopt active air or liquid cooling by embedded fluid channels.

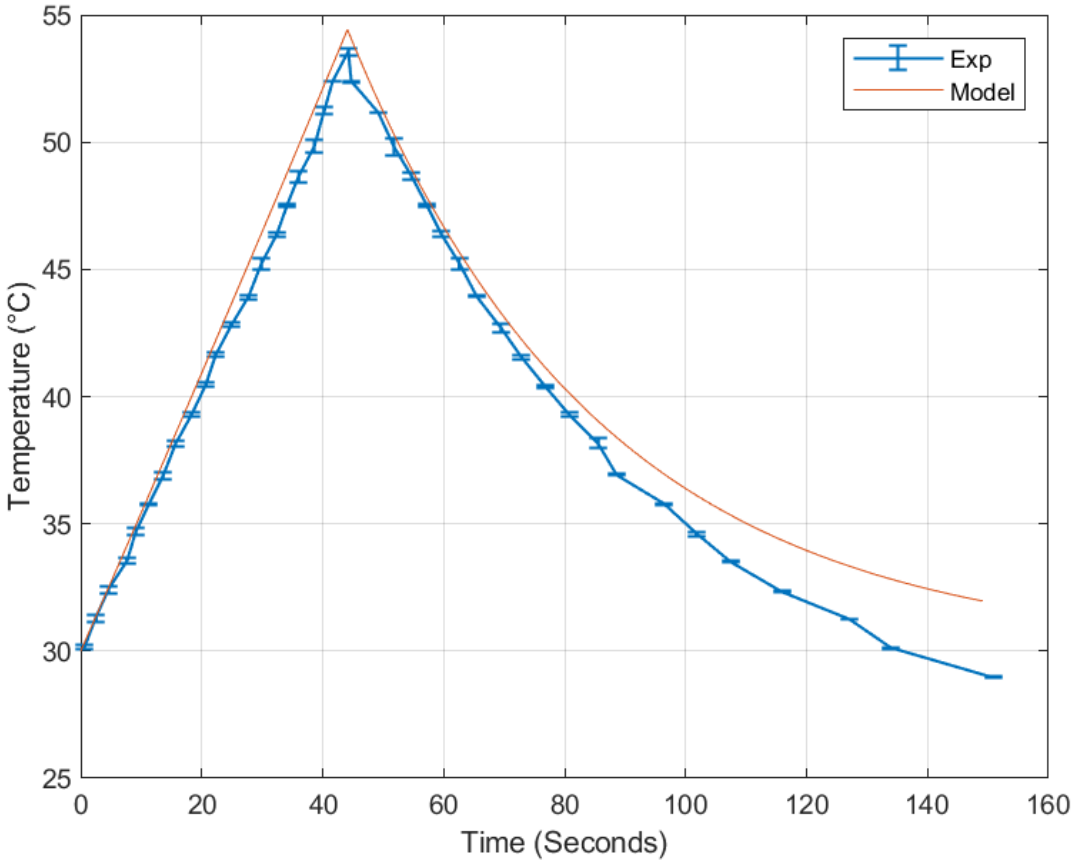


**Figure 2.10:** Measured and model-predicted temperature evolution of the CPLA sample under Joule heating (50 mA) and then natural cooling in air.

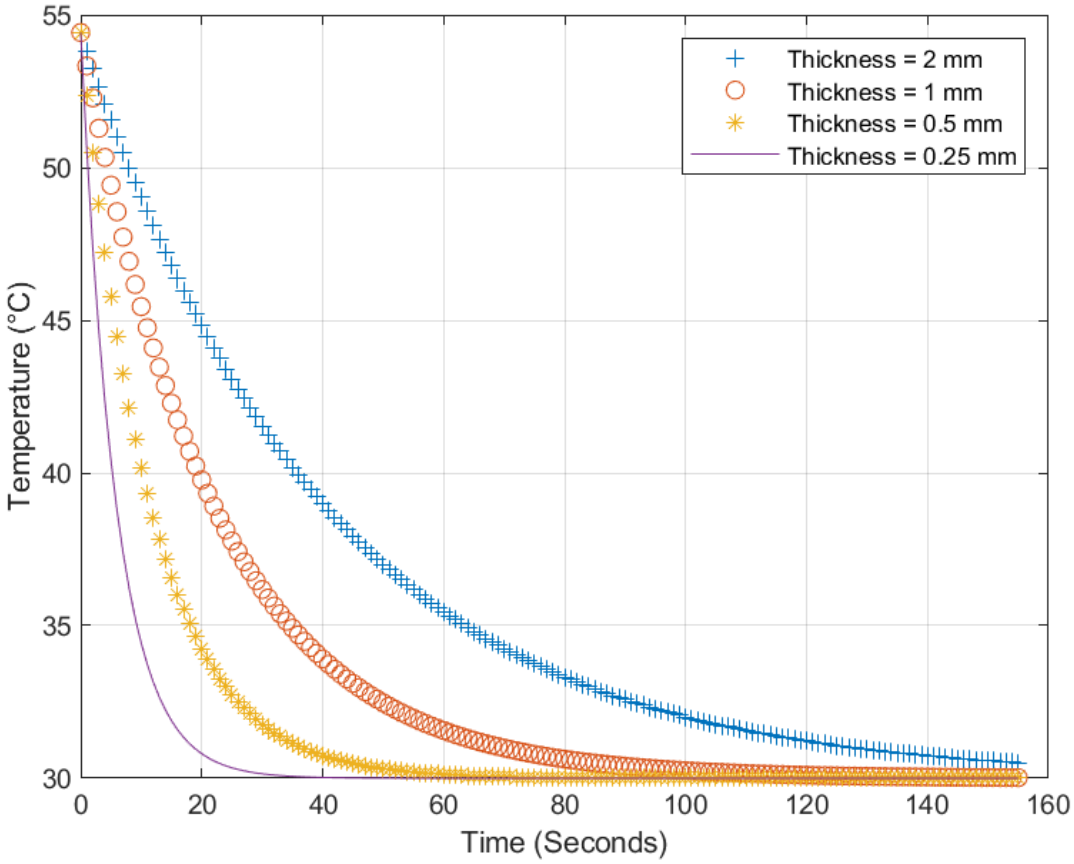


**Figure 2.11:** Simulated temperature trajectories of CPLA samples under natural cooling. The samples are assumed to have the same length and width (10 mm by 10 mm).

## 2.3 Finite Element Modeling and Simulation

The characterized mechanical, electrical, and thermal properties of the 3D-printed CPLA material are essential for understanding and predicting the behavior of CPLA-embedded soft actuators. As already shown in Section III, the measured electrical and thermal properties can be used to construct low-order dynamic models to predict the time response of Joule heating and cooling of CPLA. In this section, we use these material properties to create finite element model of a soft pneumatic actuator integrated with the CPLA, and examine its actuation response when individual CPLA virtual joints are activated, which will be further validated with experimental

measurement. Such actuators will also serve as fingers for the robotic gripper to be discussed in Section VI.

The finite element modeling analysis is conducted using the ANSYS Workbench. Three modules from ANSYS toolbox are used to conduct the simulation. The first one is the electrical system, which is used to compute Joule heating using the electrical resistivity of CPLA and the current applied to the CPLA hinges. The electrical analysis solution data is then passed as a load to the steady-state thermal analysis simulation, using an imported load to generate a temperature distribution profile for the actuator. The last module is the static structural system, where pressure on the inner walls of the actuator chamber can be specified to simulate the pneumatic input.

Two materials of interest are the CPLA and the silicone material (Dragon Skin 30, Smooth-On) for the soft actuator. The properties of CPLA used in the simulation are listed in Table 2.3. To characterize the material properties of the silicone, a uniaxial tensile test was performed following the D412-15a standard. The dumbbell test pieces were stretched at 500 mm/min. Five samples were stretched using a tensile tester (Universal Testing Machine 3345, Instron) and the average data obtained from the five samples were used in the FEM analysis. The averaged stress-strain data were fitted with a Ogden hyper-elastic model [70], which takes the following form for its strain energy function:

$$W = \sum_{i=1}^{N} \frac{\mu_i}{\alpha_i} (\lambda_1^{\alpha_i} + \lambda_2^{\alpha_i} + \lambda_3^{\alpha_i} - 3) \tag{2.3}$$

**Table 2.3:** CPLA parameters used in simulation.

| Property | Value | Unit |
|---|---|---|
| Density | 1.21 | g/cm$^3$ |
| Coefficient of thermal expansion | Tabular values from Figure 2.7 | $^\circ$C $^{-1}$ |
| Isotropic elasticity | Tabular values from Figure 2.6 | MPa |
| Isotropic thermal conductivity | 0.36 | W/m K |
| Isotropic resistivity | Tabular values from Figure 2.9 for heating | Ohm cm |

This model was used in fitting the experimental data of the mechanical tests in the strain range of

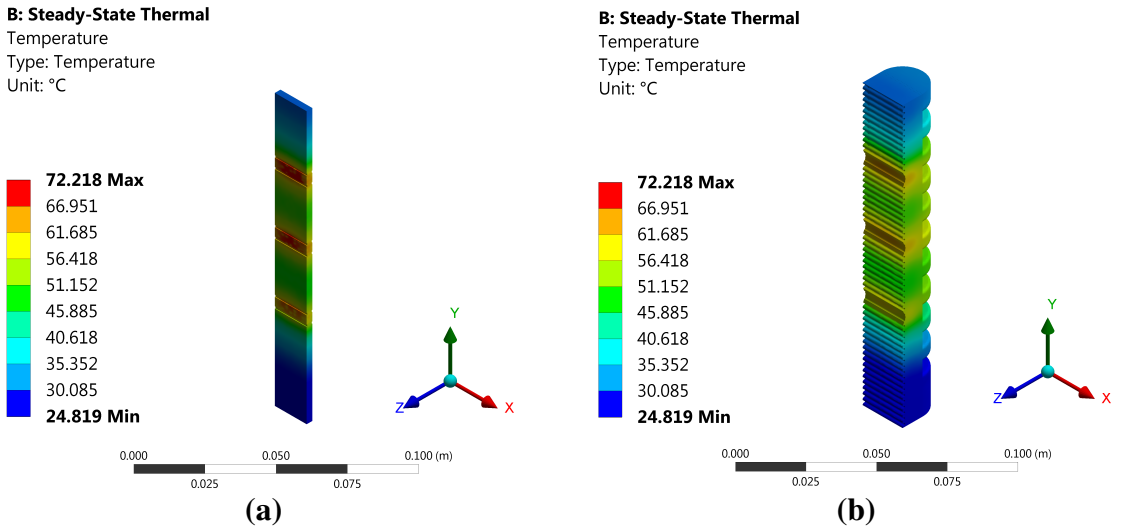


**Figure 2.12:** Simulated temperature distributions from the FEM thermal analysis for (a) CPLA, (b) SPA with embedded CPLA layer. The applied current is 60 mA

$(0 - 250)\%$. The least square curve fit was used to determine the parameters for each stress-strain data using ANSYS-Workbench. The Ogden model proved to be the best constitutive model with parameter values $N = 1$, $\alpha_1 = 2.7172$, $\mu_1$=0.1581 MPa.

In the simulation, an electric current is applied to the hinges and the air pressure is directly applied to all the walls of the pneumatic chamber. Figure 2.12 shows the temperature distributions at the steady state for both the CPLA layer and the SPA integrated with the CPLA, where the applied current is 60 mA and no pressure applied. The steady-state bending behaviors of the actuator under different air pressures obtained with the FEM simulation are illustrated in Figure 2.13. Pressure values of (4 psi, 8 psi, 12 psi, 16 psi, 18 psi) are applied in the simulation while different hinges are activated with Joule heating. In particular, it can be seen that, for each case, the actuator bends most appreciably around the location of the activated joint(s) while the remaining parts stay almost flat due to the rigidity of CPLA at the room temperature. Furthermore, for each configuration of activated hinge(s), the bending increases with the pressure applied to the actuator. The simulation results suggest that different bending shapes can be obtained via activating CPLA at proper locations, while the bending amplitude can be modulated with the pressure input. These observations will be further validated with experimental results in the next section.

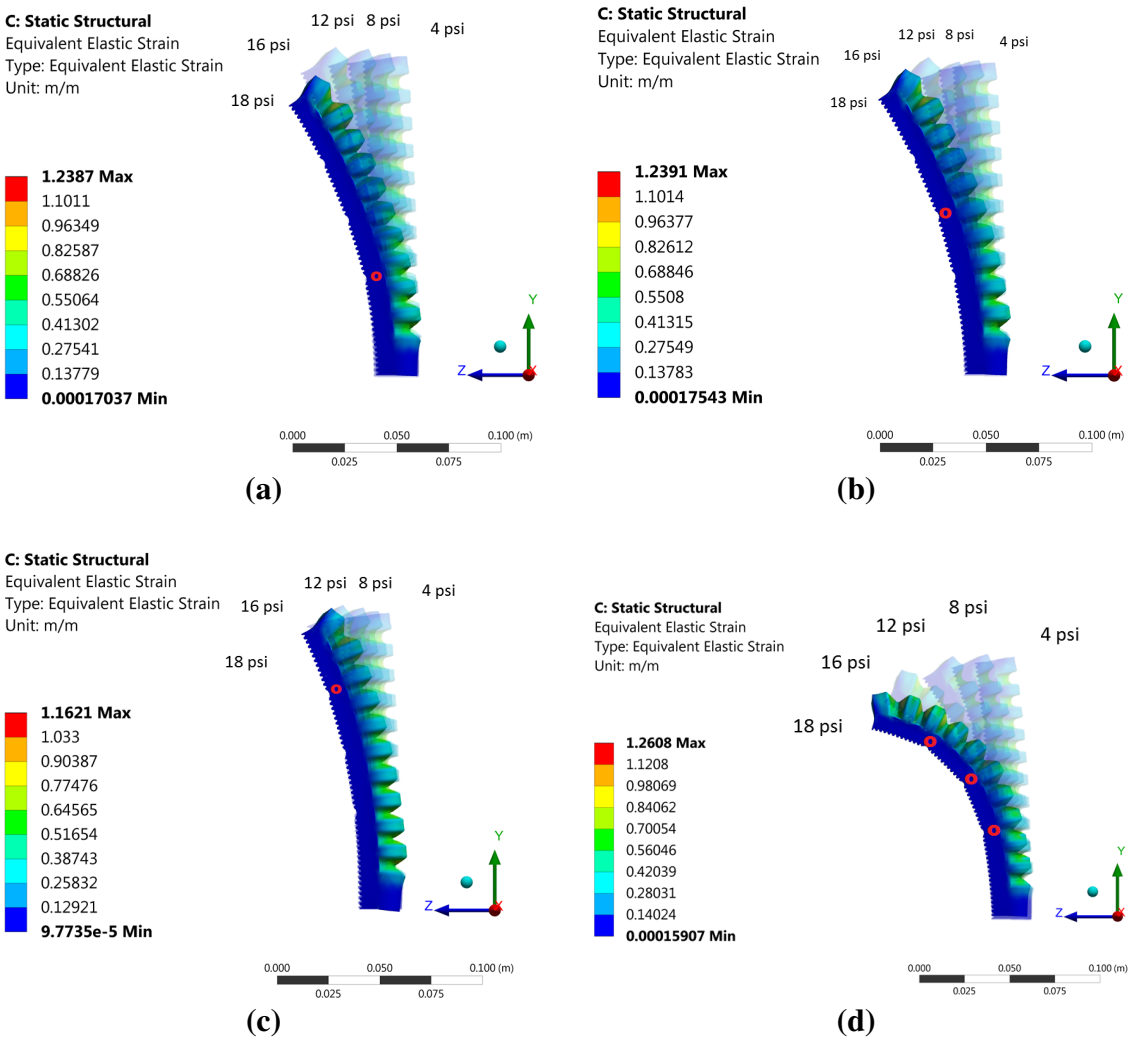


**Figure 2.13:** Simulated bending of the soft actuator under different pressure inputs, when (a) Hinge 1, (b) Hinge 2, (c) Hinge 3, (d) all hinges are activated with Joule heating. The red circles indicate the CPLA joints being activated with a current of 60 mA.

## 2.4 Experimental Model Validation

The SPA with embedded CPLA was clamped to an aluminum bar for testing the bending when different CPLA joints of the actuator were activated. For each configuration, a set of pressure values (4 psi, 8 psi, 12 psi, 16 psi, 18 psi, 20 psi, and 24 psi) was applied to the SPA. A pneumatic platform (Fluidic Control Board, Paradox Robotics™) [71] was used in combination with an integrated data-flow software (LabVIEW, National Instruments) to control the SPA inner pressure. To activate a given CPLA joint, a voltage of 12V was applied for over two minutes so the current could reach its steady state (around 60 mA). The temperature of each joint was measured using an infrared thermometer gun. Since the CPLA was encapsulated with silicone, the steady-state temperature detected at each joint was close to the CPLA Tg value (58 °C). Figure 2.14 shows the snapshots of the SPA with embedded CPLA, when different values of pressure (vertical axis) were applied to the SPA, for a given configuration of CPLA joint activation (horizontal axis). The snapshots were taken at the steady state of each configuration.

To quantitatively compare the results from FEM simulation and experiments, we define bending angles at the joints ($\theta_1$, $\theta_2$, $\theta_3$), as illustrated in Figure 2.15. In particular, angle $\theta_i$ captures the angle between the segment above hinge $i$ and the vertical line. Figures 2.16,2.17, and 2.18 show the comparisons of bending angles for Hinges $1-3$ from simulation and experiments when these hinges are activated at the same time, for the pressure range of 4 psi – 18 psi. It can be seen that, for all cases, the model-predicted bending angles show high consistency with the experimentally measured ones, with an error less than 2 degrees except for the case of Hinge 2 and 3 at 18 psi, where the error is around 4 and 7 degrees respectively. It is also noted that the bending angle at each hinge shows an increasing trend with the pressure, as expected.

## 2.5 Application to Grasping: Posture Reconfiguration and Shape Holding

Additional experiments were conducted to test the CPLA-embedded SPAs in a two-finger gripper configuration. The stiffness modulation in each finger could be controlled independently, allowing the generation of different bending angles to suit the shape of the object being manipulated.

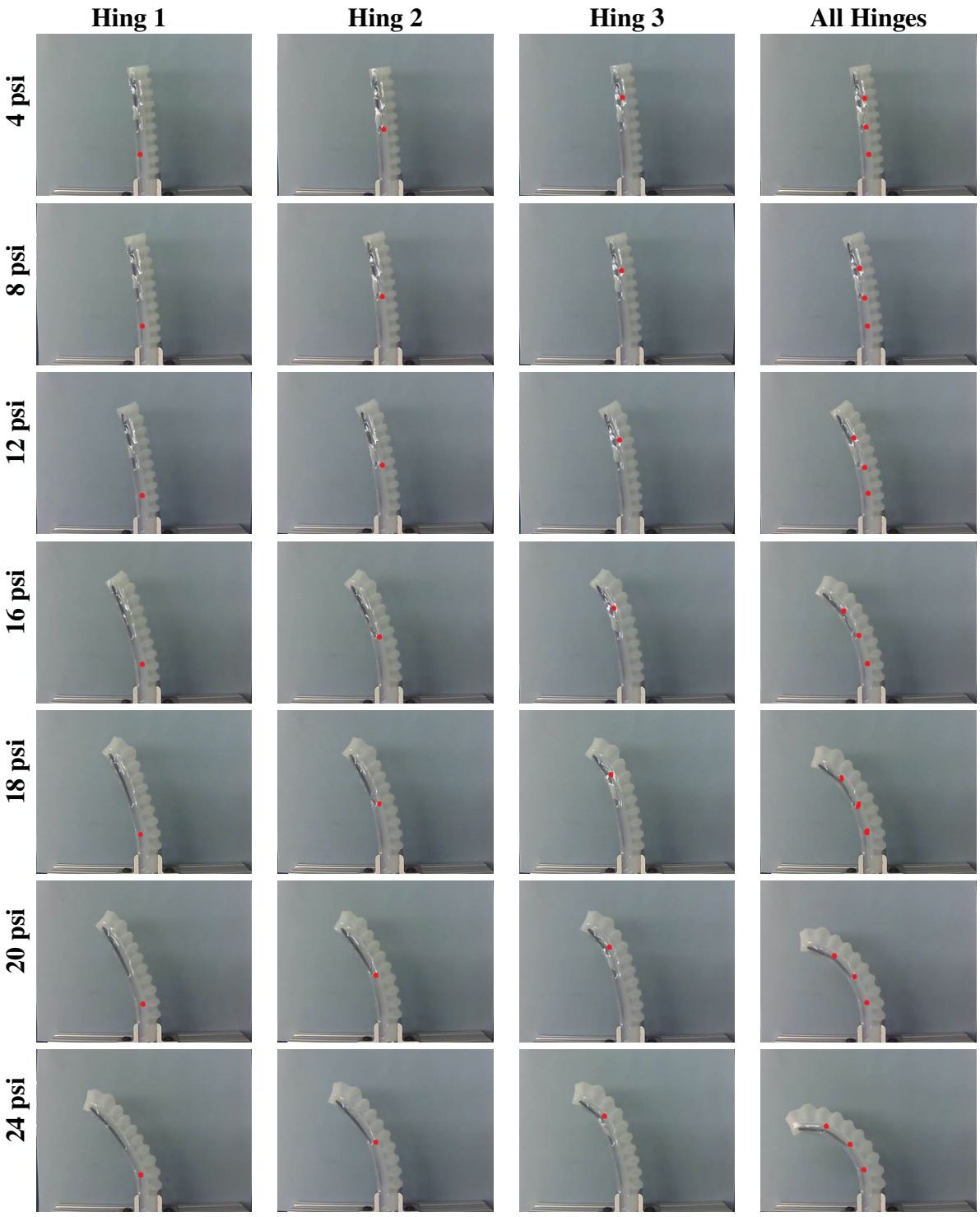


**Figure 2.14:** Snapshots of the CPLA-embedded SPA under different pressure values, when different CPLA hinges were activated. Each column shows the achieved shapes with a given configuration of hinge(s), under the pressures ranging from 4 psi to 24 psi (top to bottom). Four hinge activation configurations were used: individually activating joints 1 – 3, respectively, and activating all joints simultaneously. The red circles in each picture indicate the locations of activated hinges.

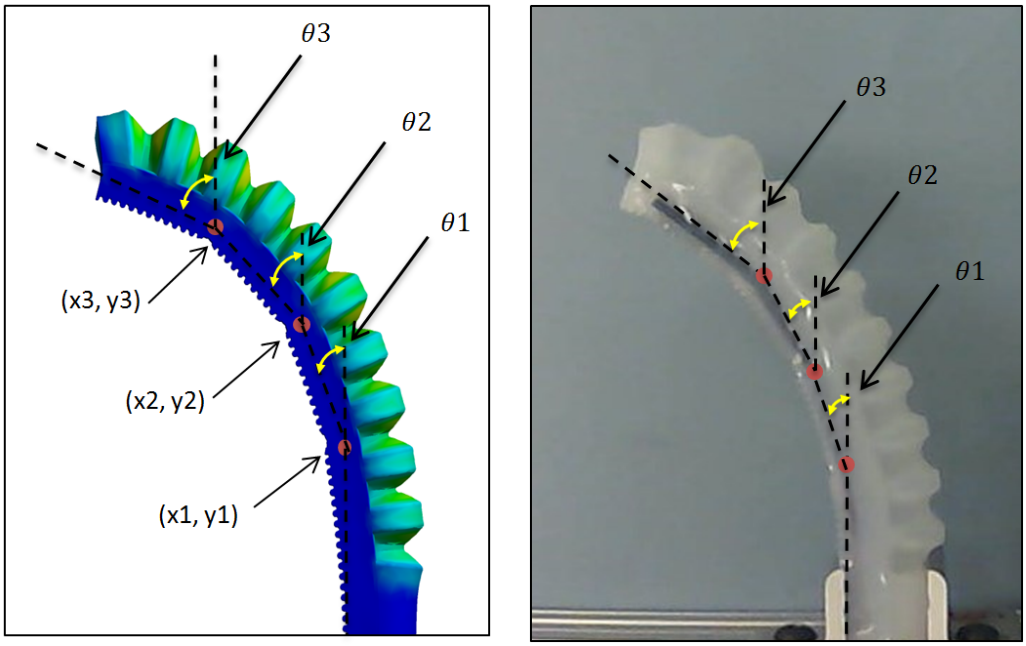


**(a)** **(b)**

**Figure 2.15:** Illustration of the bending angles at different hinges: (a) simulation scenario; (b) experimental scenario.

Multiple objects with various shapes and hardness were tested, where different grasping modes (e.g., scooping, pinching, grabbing.) were executed. In Figure 2.19 (a), (b), and (c), the soft gripper was holding a plastic container using the aforementioned modes, while in Figure 2.19 (d) and (e), a soft mini football and a plastic cup filled with candies were lifted. For Figure 2.19 (a) – (d), all joints in both fingers were activated, while for Figure 2.19(e), the left finger had all joints activated and the right finger had only the joint closest to the clamped end activated. All experiments were performed with a constant pressure of 20 psi for both fingers. Note that in these trials, CPLA enabled local shape reconfiguration of the actuators for the execution of different grasping modes.

In order to evaluate the payload capacity of the SPA integrated with CPLA, several weights were placed inside a plastic container, which was being held by a single finger. The masses ranged from 50 g to 500 g (Figure 2.20), and the total carried weight was increased in increments of 50 g. The tests were performed for a minimum of 50 g and a maximum of 800 g. Figure 2.21 (a) and (b) show the case where the SPA was actuated with a constant pressure of 22 psi while all hinges were activated (with a 12 V input). Experiments were further conducted to evaluate the load-carrying

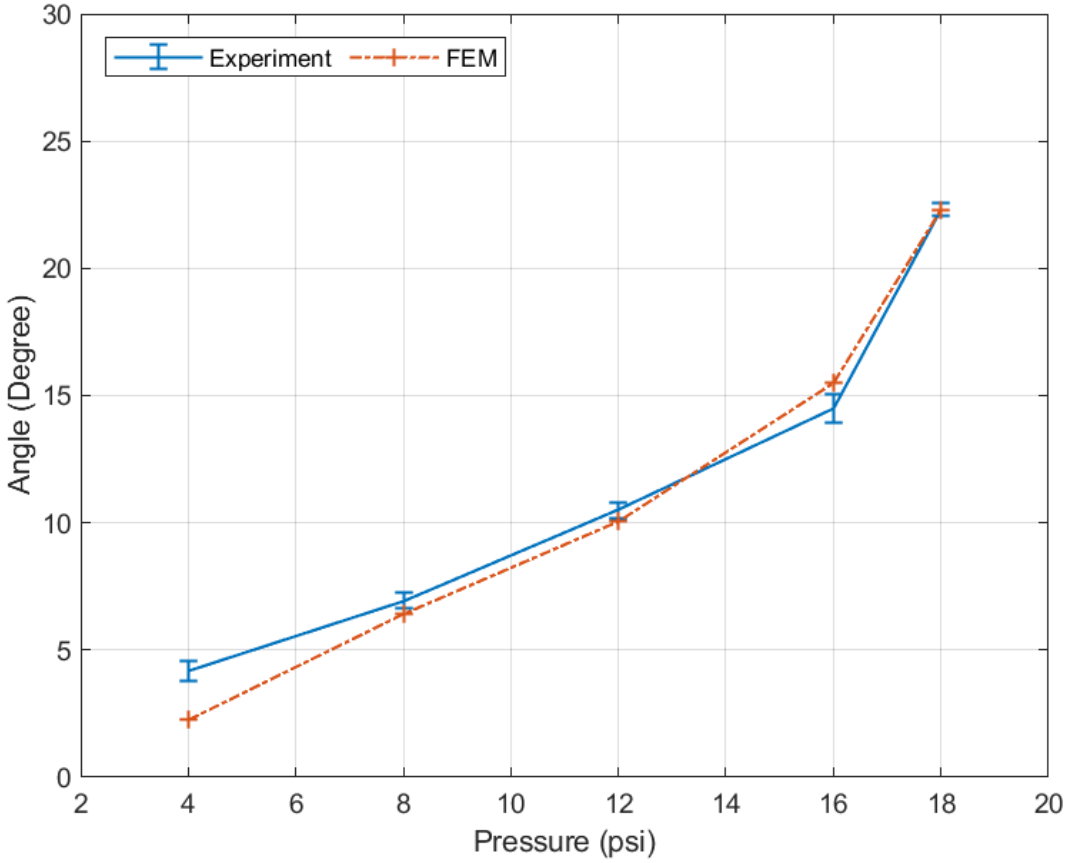


**Figure 2.16:** Comparison between model-predicted bending angle $\theta_1$ at Hinge 1 with the experimental measurement (standard deviation range: (0.24 – 0.58), when all hinges were activated with Joule heating.

capacity of the conductive PLA-embedded SPA when the actuation inputs were removed after it had achieved a given actuated shape. Specifically, the SPA was initially actuated with a pneumatic input of 24 psi, with all CPLA joints activated; with the pressure still on, the voltage input to the CPLA joints was removed to cool and "lock" the joints; once the CPLA joints were cooled down to the room temperature, the pressure input to the SPA was removed. Weights were then added to the SPA finger in this passive state (Figure 2.21 (c) and (d)). As shown in Figure 2.21, for both active and passive states, the soft finger was able to withstand the maximum payload of 800 g without causing any device failure or dropping the weights. The small difference in both shape and load-carrying capacity between the active and passive configurations is particularly important for

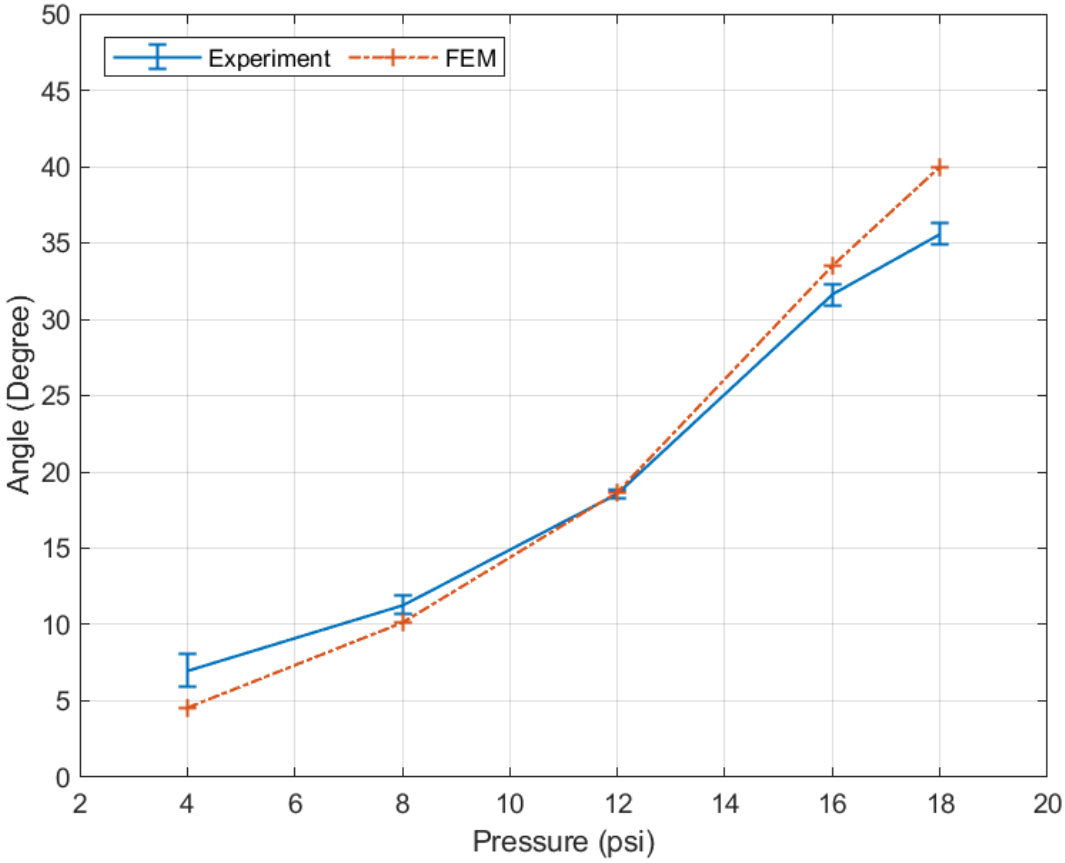


**Figure 2.17:** Comparison between model-predicted bending angle $\theta_2$ at Hinge 2 with the experimental measurement (standard deviation range: (0.29 – 1.1), when all hinges were activated with Joule heating.

applications that involve holding given postures for long periods of time, because one could use the passive configuration to save energy (without the need for pressure and electrical inputs) without compromising the performance. Note, however, one needs to first actuate the SPA and activate the CPLA to achieve a desired shape before deploying the passive configuration.

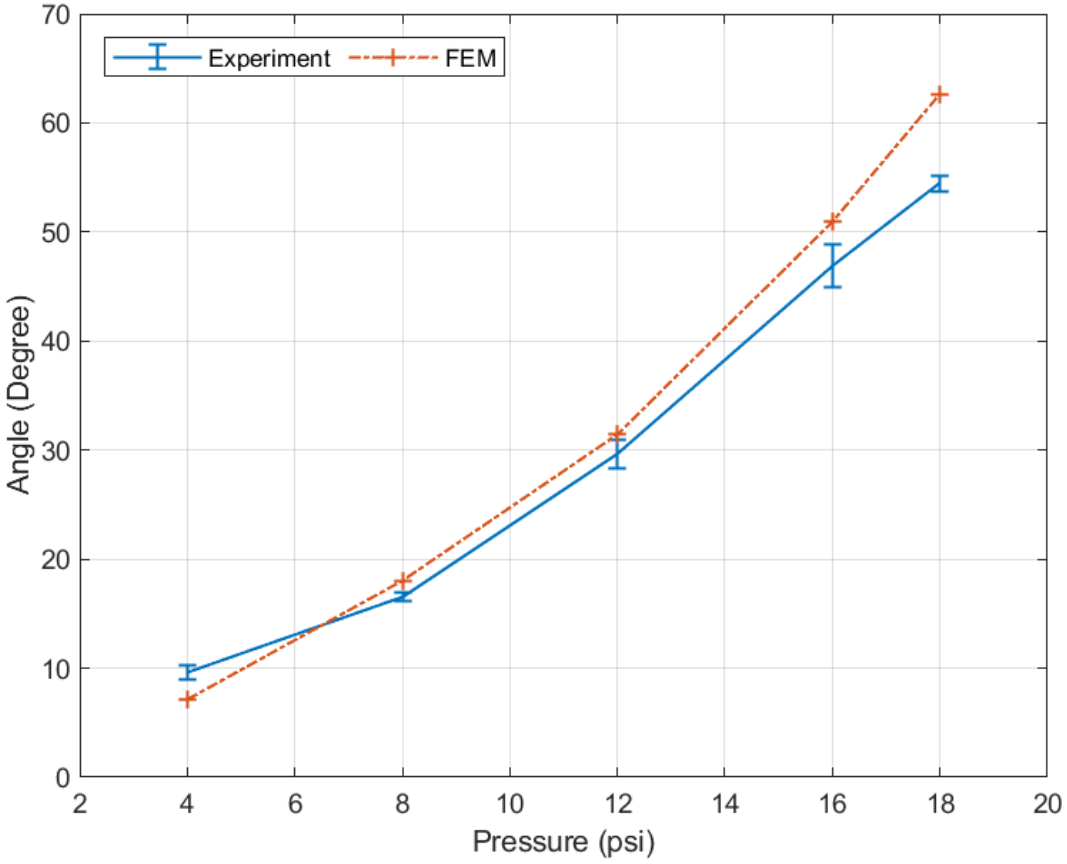


**Figure 2.18:** Comparison between model-predicted bending angle $\theta_3$ at Hinge 3 with the experimental measurement (standard deviation range: (0.39 – 1.9), when all hinges were activated with Joule heating.

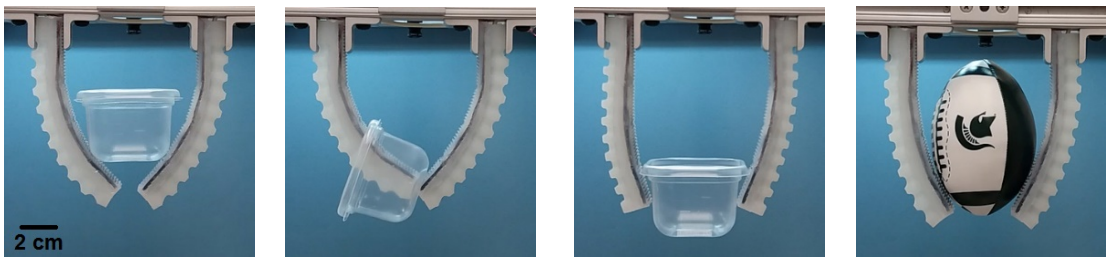


**(a)** **(b)** **(c)** **(d)**

**Figure 2.19:** Grasping of multiple objects using different grasping modes. A plastic container was grasped using (a) scooping, (b) pinching, and (c) parallel grabbing. Additional tests were conducted for grasping (d) a plushy mini football, and (e) a cup filled with candies.

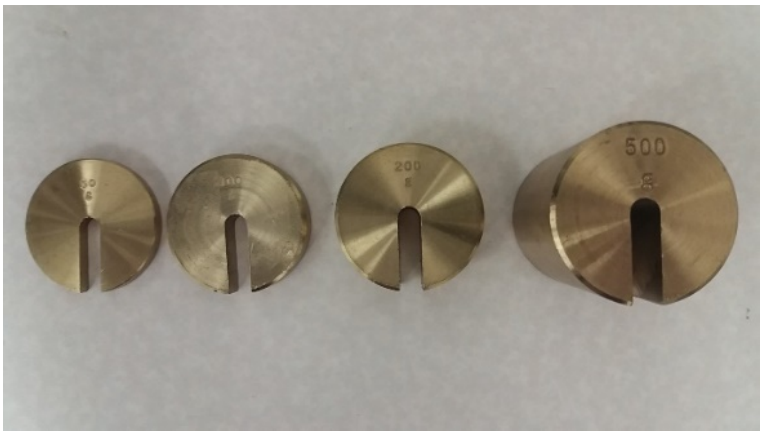


**Figure 2.20:** Metallic weights (50 g-500 g) used during the single-finger holding experiment.

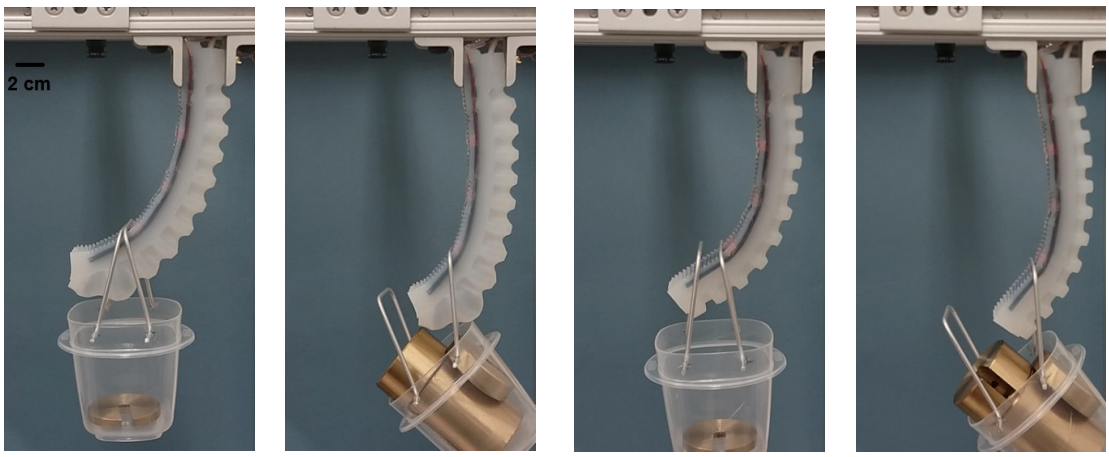


**Figure 2.21:** Testing load capacity of the SPA integrated with CPLA for both the active state and the passive state. A single-finger SPA-CPLA holding (a) a minimum weight of 50 g, and (b) a maximum of 800 g when the SPA was actuated with 22 psi and all CPLA joints activated with a 12 V input. A single-finger SPA-CPLA holding (c) a minimum weight of 50 g, and (d) a maximum weight of 800 g, when the SPA-CPLA was deployed in the passive state after first being actuated with 24 psi with all joints activated.

## 2.6 Conclusion

In this chapter, a novel selective stiffness modulation method was proposed and implemented on soft actuators. The method utilizes an FDM 3D printer to print a conductive PLA material (CPLA), the stiffness of which can be modulated by simply applying electrical current to areas of interest. Comprehensive experiments are conducted to acquire the CPLA thermomechanical and electrical properties. Results from FEM simulation and experimental measurements from a case study of a SPA embedded with CPLA show good match. Finally, a gripper, comprised of two CPLA-embedded SPAs, demonstrated the ability to grasp different objects by changing the stiffness of the gripper fingers. Furthermore, the SPA showed that it could be effectively locked in a desired bending configuration while carrying a weight even in the absence of pressure or voltage input.

# CHAPTER 3

# A 3D−PRINTED STRETCHABLE STRAIN SENSOR

In this chapter we report 3D−printed stretchable strain sensors that embed a flexible conductive composite material in a hyper−elastic substrate. Three commercially available conductive filaments are explored, among which the ETPU from Rubber3D Printing, Sweden, shows the highest sensitivity and working strain range. The ETPU strain sensor exhibits an interesting behavior where the conductivity increases with the strain. Finite−element modeling and simulation are conducted to investigate the behavior of the 3D−printed stretchable strain sensor when it is subjected to wind loading as a case study. The model-predicted sensor output at different wind speeds, obtained with the computed sensor strain and the experimentally characterized strain−resistance relationship, achieves good match with the experimental data.

The remainder of the chapter is organized as follows. The characterization of material properties and the procedure of 3D-printing the sensors are first presented in Section 3.1. Then the characterization of strain-sensing behaviors is discussed in Section 3.2. FEM modeling and simulation results are described in Section 3.3, followed by experimental characterization and model validation of wind-sensing for the ETPU strain sensor in Section 3.4. Finally, concluding remarks are provided in Section 3.5.

## 3.1 Material Characterization and Sensor Fabrication

The sensors are fabricated with a low−cost, desktop 3D−Printer (QIDI TECH I, QIDI TECHNOLOGY, China) with a customized dual−extruder setup. The use of dual extruders enables the integration of two different materials. The printer has a nozzle diameter of 0.4 mm and a layer resolution of 0.1 mm, Figure 3.1 shows a schematic diagram of dual−extruder 3D−printer. The software SIMPLIFY3D 4.1 is utilized for controlling the 3D−printer and adjusting the printing parameters. Detailed settings for the 3D−printing are provided in the appendix (Table 3.1).

Three types of electrically conductive filaments (conductive graphene PLA, conductive PLA,

**Table 3.1:** Filaments used for sensor fabrication.

| Filament name | Company | Volume resistivity (Ohm cm) | Tensile strength (MPa) |
|---|---|---|---|
| Conductive Graphene PLA | Graphene 3D Lab | 0.6 [72] | 2350 |
| Conductive PLA | Proto−Pasta | 15 [72] | 1000 |
| ETPU | Rubber 3D Printing | 800 [72] | 47.6 |
| X60 | Diabase | ∞ | 5.885 |

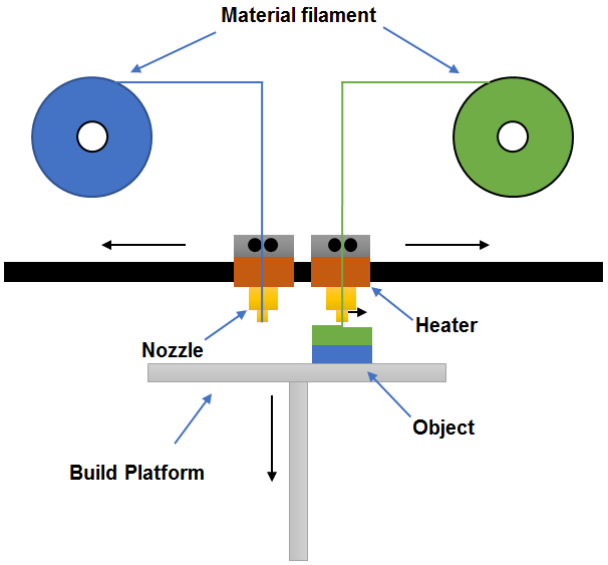


**Figure 3.1:** Schematic diagram of dual-extruder 3D−printer.

and ETPU) and one stretchable filament (X60 from Diabase, USA) were first mechanically characterized before fabricating the sensors. Additional information of each filament is listed in Table I. The resistivity value of each conductive material is provided by the manufacturer. And as shown in this work, the resistance of each shows strong dependence on the strain. The stiffness of each material is measured using a tensile testing machine (model SFM−20, United Testing Systems Inc., USA) at 25 °C. The specimen geometries followed specifications outlined in ASTM D412−15a [72] for the X60 filament and ASTM D−638 [72] for the three conductive filaments. All samples were printed with a thickness of 2 mm. The tension specimens were tested in batches of five for each material, and the values of Young's modulus were averaged over the five trials. The Young's modulus was calculated from the stress−strain ratio below the proportional limit of the material.

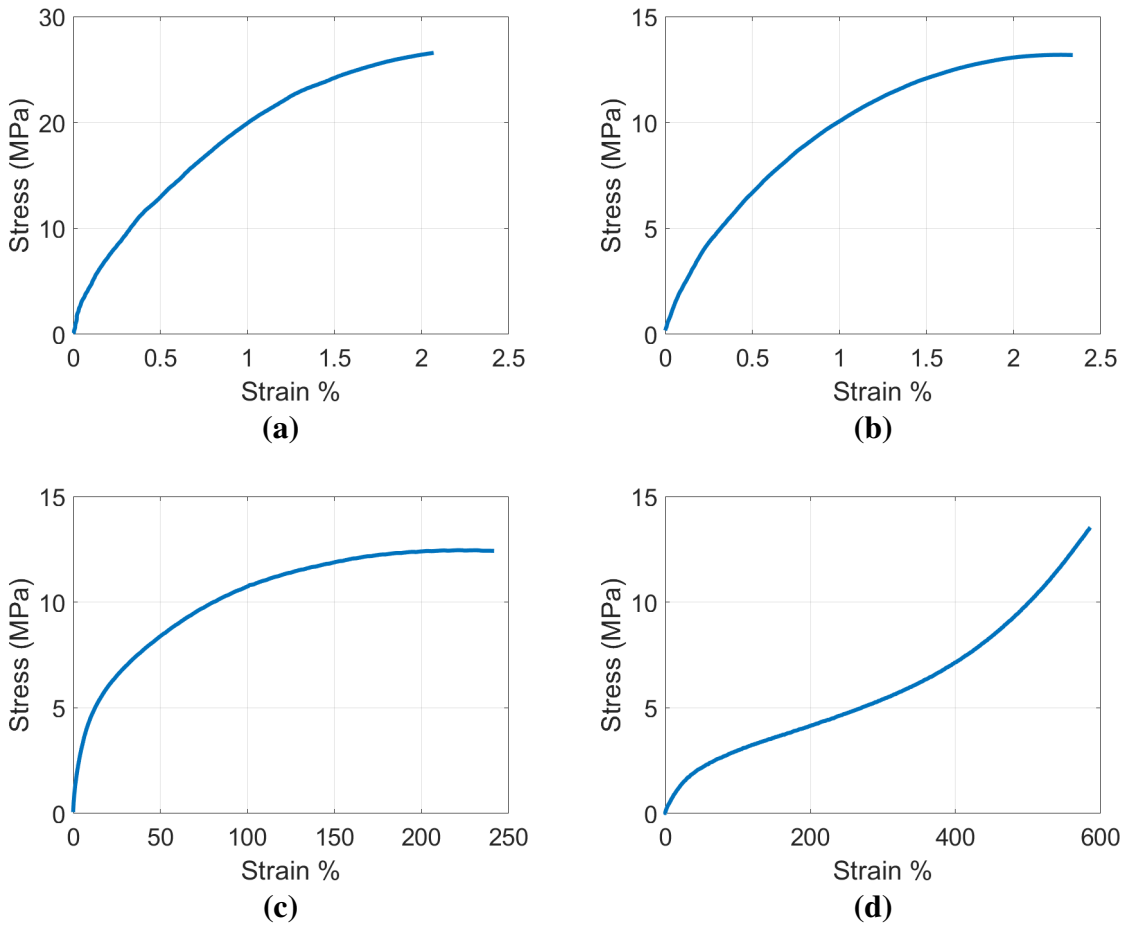


**Figure 3.2:** Experimentally characterized curve for the (a) Conductive Graphene PLA, (b) Conductive PLA, (c) ETPU, and (d) X60 filament.

Figures 3.2 shows the stress−strain graphs for all materials, and one can see that the ETPU has the lowest modulus among the conductive materials, and the X60 filament shows a typical hyper−elastic curve, which makes it a good candidate as a substrate to the sensors. Note that each material was subjected to a different range of strains, as determined by the stretchability of the corresponding material. Both ETPU and X60 have excellent stretchability (over 200% and 500%, respectively), while conductive graphene PLA and conductive PLA show much less stretchability. Table 3.1, lists the measured Young's modulus for each material.

In this work we explore a basic design where the conductive sensing element is printed on top of the ultra−flexible substrate. One could also consider using the substrate to completely encapsulate the sensing element. Figure 3.3 shows the dimensions of the sensors, with 0.5 mm

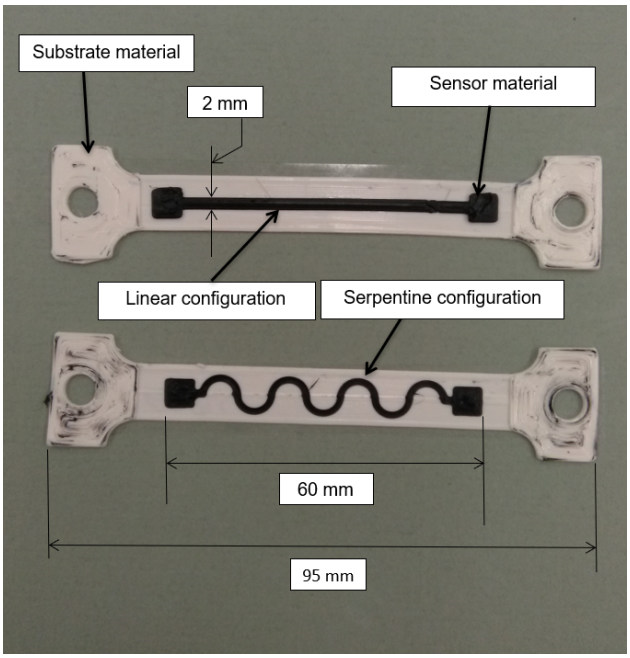


**Figure 3.3:** 3D−printed wind sensors with different shapes.

and 0.25 mm being the thicknesses for the hyper−elastic and the conductive filaments, respectively. Since conductive graphene PLA and conductive PLA are relatively stiff, both a straight line design and a serpentine design are investigated. The serpentine design allows the sensor to be stretched more before breaking, but its sensitivity will be lower [73]. During the tests, we 3D−printed both designs for each one of the conductive filaments, but it turns out that the Conductive Graphene PLA and Conductive PLA−based sensors in the straight line configuration would peel off the X60 substrate under the smallest deformation we could apply, so for these materials, only the results for the serpentine design are presented.

## 3.2 Characterization of Strain−Sensing Behavior

The proposed approach uses the change of resistance in response to tension to measure the wind velocity. Therefore, it is important to characterize the strain−sensing performance of the printed sensors. Figure 3.4 shows the experimental setup for this purpose. The setup consists of two clamps, one fixed and the other mounted on a linear guide slider, the position of which can be adjusted via a stepper motor. The control of the movement of the slider during the experiments and the data

acquisition were coordinated with a microcontroller (model number A000073, Arduino). Each sensor is mounted with the two clamps and its resistance is measured with via a voltage divider circuit as the sensor is stretched with the slider. During the experiments, the maximum strain applied before the sensor is mechanically broken, is 4% for the Conductive Graphene PLA and Conductive PLA−based sensors in the serpentine configuration, 25% for the ETPU−based sensor in the serpentine configuration, and 12.5% for the ETPU−based sensor in the linear configuration and the stretching speed for all the experiments is 0.33 mm/s.

The resistance change ratio $\Delta R/R_0$, where $R_0$ is the initial electrical resistance and $\Delta R$ is the change in electrical resistance, is measured as a function of quasi−static uniaxial strain. For each sensor, the normalized resistance change shows slight hysteresis with respect to the strain, as shown in Figures 3.5(a)−3.5(d). In each case, the resistance change vs. the strain demonstrates an approximately linear relationship for low strain values, and then transitions to a saturated relationship as the strain gets higher. To characterize the cyclic stability of the strain sensors, the 3D−printed sensors are tested by measuring the resistance under repeated cycles of stretching/releasing as shown in Figures 3.6(a)−3.6(d). To compare the performance among all the sensors, a maximum strain of 4% is applied during each stretching/releasing cycle. The Conductive Graphene PLA and Conductive PLA−based sensors show unstable behavior, where the value of the resistance change ratio keeps decreasing throughout the cycles strain test. While the ETPU−based sensors exhibit some transient behavior, the responses are largely stabilized after the first 600 cycles. Therefore, a preconditioning step can be implemented in sensor fabrication, during which cycles of stretching−releasing are applied, such that subsequent measurements will be reproducible. Table 3.2 shows the initial electrical resistance $R_0$ for each 3D−printed sensor.

To characterize the sensitivity of the 3D−printed sensors at different strains, the gauge factor (GF) values are calculated using the following equation for each cycle:

$$GF = \frac{\frac{\Delta R}{R}}{\epsilon} \tag{3.1}$$

where $\epsilon$ denotes the strain. The GF values of the 3D−printed sensors at different strains are plotted in

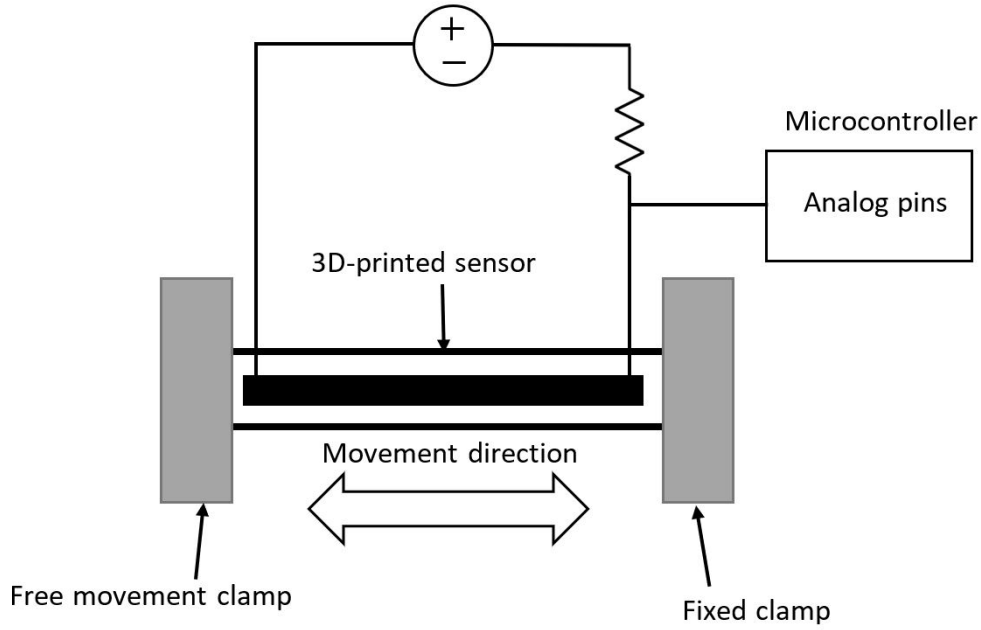


**(a)**

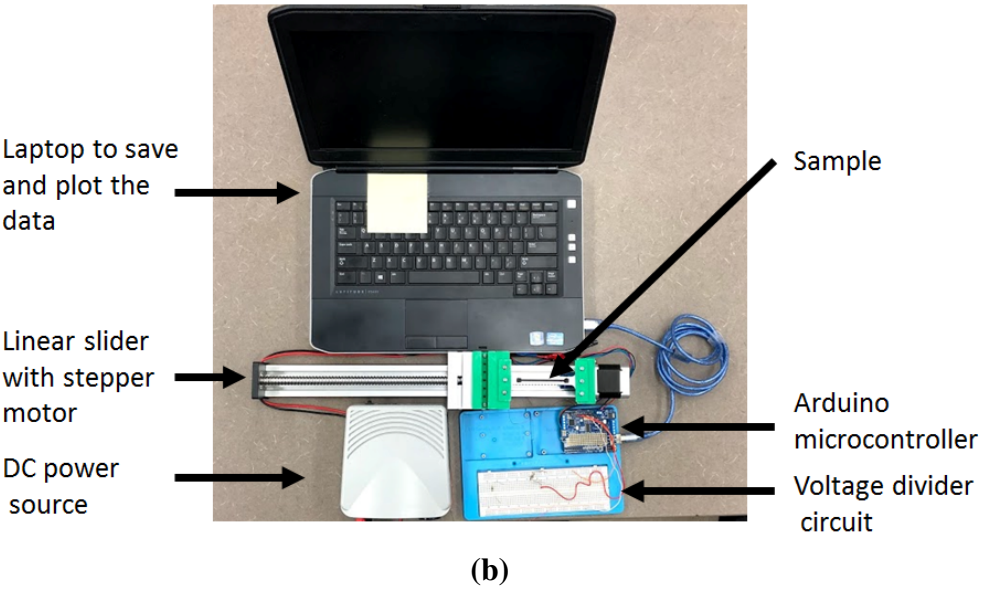


**(b)**

**Figure 3.4:** Experimental setup for characterizing the change of resistance with the mechanical strain applied by the linear slider. (a) Schematic, (b) actual setup.

Figure 3.7. The GF of each sensor is computed based on the average of the slopes of the normalized resistance change vs. the strain when the sensor is stretched and released, respectively (Figure 3.5), for the linear, low−strain range (< 2%). The ETPU−based sensor in the linear configuration shows the highest sensitivity (GF of 20) to strain, which makes it a good candidate for the proposed

**Table 3.2:** 3D–printed sensors initial electrical resistance.

| # | Sensor | $R_0$ ($k\Omega$) |
|---|---|---|
| 1 | Conductive Graphene PLA sensor (serpentine) | 2.62 |
| 2 | Conductive PLA sensor (serpentine) | 27.13 |
| 3 | ETPU sensor (serpentine) | 4884.43 |
| 4 | ETPU sensor (linear) | 4761.24 |

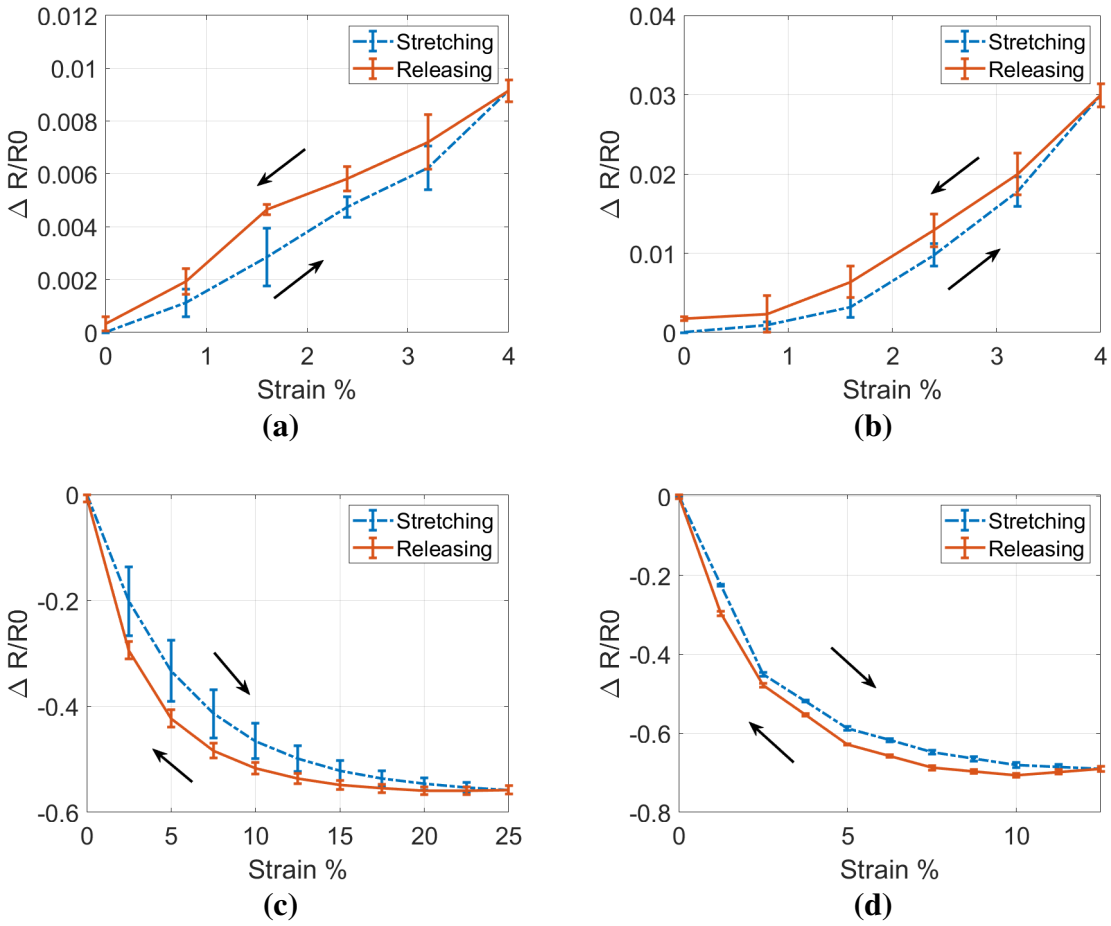


**Figure 3.5:** Normalized resistance change for the (a) Conductive Graphene PLA sensor (serpentine), (b) Conductive PLA sensor (serpentine), (c) ETPU sensor (serpentine), (d) ETPU sensor (linear) during five stretching/releasing cycles.

wind sensor. The GF for metallic foils are typically between 2 to 5 [74], which indicates the competitiveness of the 3D–printed strain sensors with respect to their metallic counterparts.

During the tests, conductive graphene PLA and conductive PLA–based sensors show an increase of resistance when the strain increases, but the ETPU–based sensors demonstrate an opposite trend.

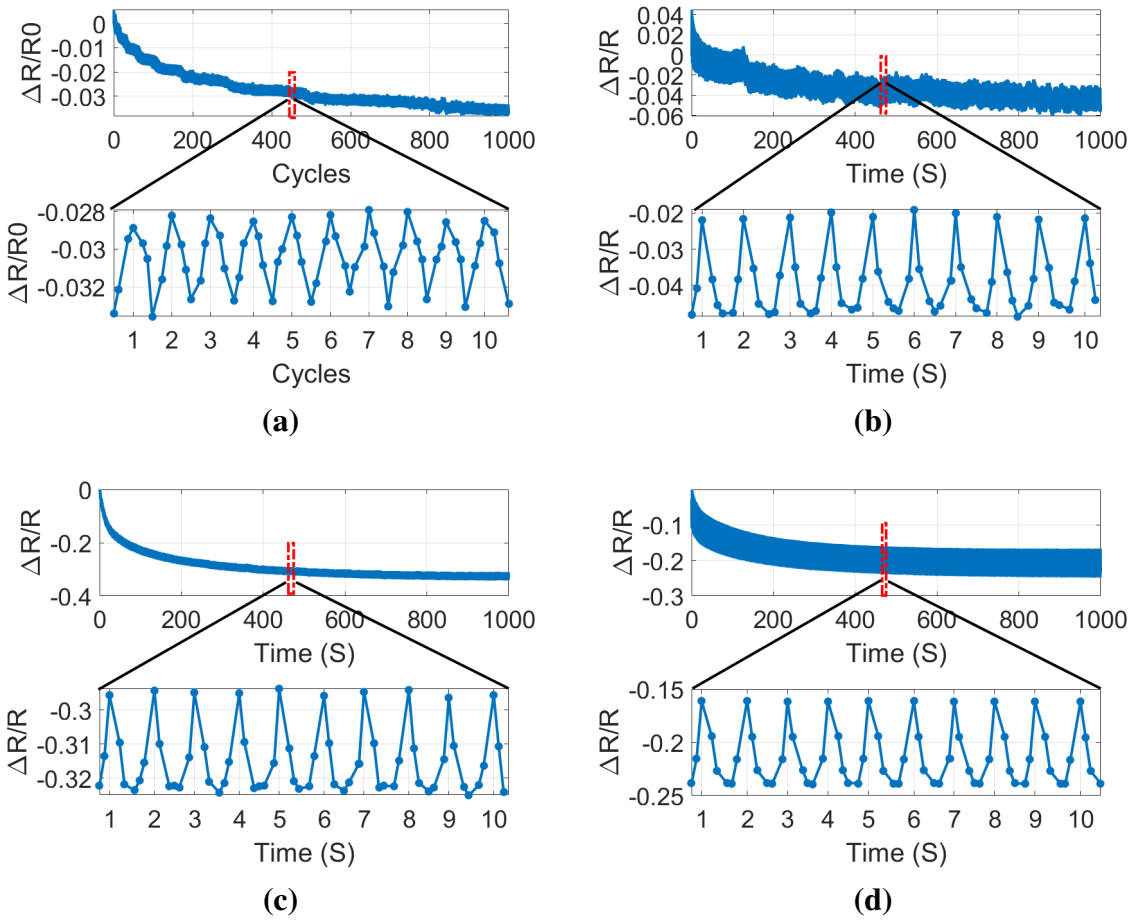


**Figure 3.6:** Stretching/releasing cycle tests of change in resistance with 4 % applied strains for the (a) Conductive Graphene PLA sensor (serpentine), (b) Conductive PLA sensor (serpentine), (c) ETPU sensor (serpentine), (d) ETPU sensor (linear).

This is a non−trivial material response, and similar behavior was reported for the stretchable sensor fabricated by Xie *e*t al. [75]. In their work, the origin of this behavior derives from the nanoscale micro−structural rearrangements under the stretching deformation. Similar experiments are needed for the ETPU−based sensors to investigate the origin of the decrease of resistance with an applied strain.

## 3.3 Finite Element Modeling and Simulation

In this section, we use the characterized material properties to create an FEM model of a 3D−printed wind sensor, and examine its deformation response when subjected to air flow, which

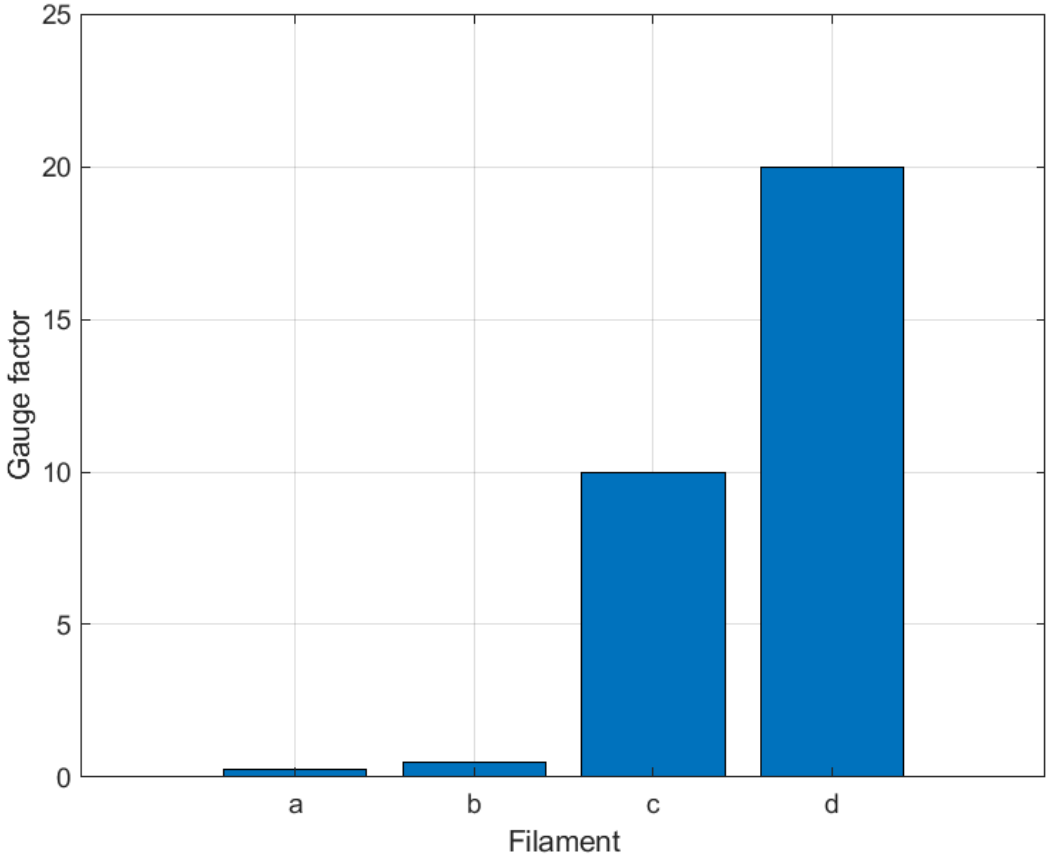


**Figure 3.7:** GF value for the linear, low−strain range (< 2%) for the (a) Conductive Graphene PLA sensor (serpentine), (b) Conductive PLA sensor (serpentine), (c) ETPU sensor (serpentine), (d) ETPU sensor (linear).

will be further validated with experimental measurement. The Ansys software is used for implementation of the fluid structure interaction (FSI) setup, which couples the Ansys fluid flow module (Fluent) and the Ansys static structural module. This setup allows both solvers to run simultaneously, exchanging data when needed without outputting intermediate results. Figure 3.8 shows the FEM simulation setup, where the sensor is fixed from both ends and the wind load is applied perpendicularly on the sensor.

In the simulation a wind velocity range (1−15) m/s is considered and the calculated force at the fluid−structure interface is transferred to the mechanical model and applied as load. Figure 3.9 shows the wind velocity profile in isometric view when an air flow of 15 m/s is applied to the

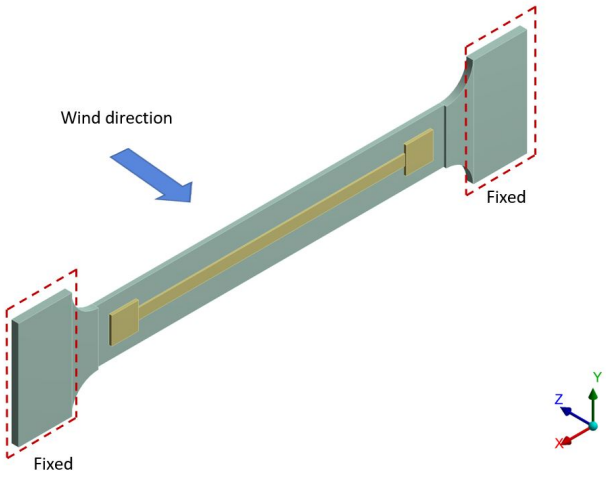


**Figure 3.8:** FEM simulation setup for the 3D−printed sensor.

3D−printed sensor. The wind inlet is from the x−y plane marked with dashed lines. The elastic strain profile on the conductive layer of the sensor at 15 m/s wind velocity is shown in Figure 3.10, which indicates that the maximum strain value is in the center of the sensor body. The deformation of the sensor will change when the wind velocity increases or decreases. For example, Figure 3.11 shows the simulated elastic strain profile for different wind velocity values (15, 10, 5 m/s). From the figure, one can see that the deformation will decrease significantly when the wind velocity drops

## 3.4 Experimental Characterization and Model Validation Of Wind−Sensing Performance

A wind tunnel (X−Stream, Pitsco) is used in experimentally characterizing the response of the 3D−printed ETPU strain sensor under different wind speeds. This wind tunnel has a low−restriction flow straightener, combined with a 6:1 compression ratio intake bell, which converts turbulent air flow into smooth, laminar flow for repeatable test results. The system has a total length of 180 cm and a test section of 30 cm. As shown in Figure 3.12, the wind tunnel is equipped with a handheld control unit to adjust the velocity of the air moving through the test chamber (up to 18 m/s), and a manometer to indicate the actual velocity.

The sensor is clamped to a standard precision dovetail Z−axis stage (ZDTLS80, Misumi USA)

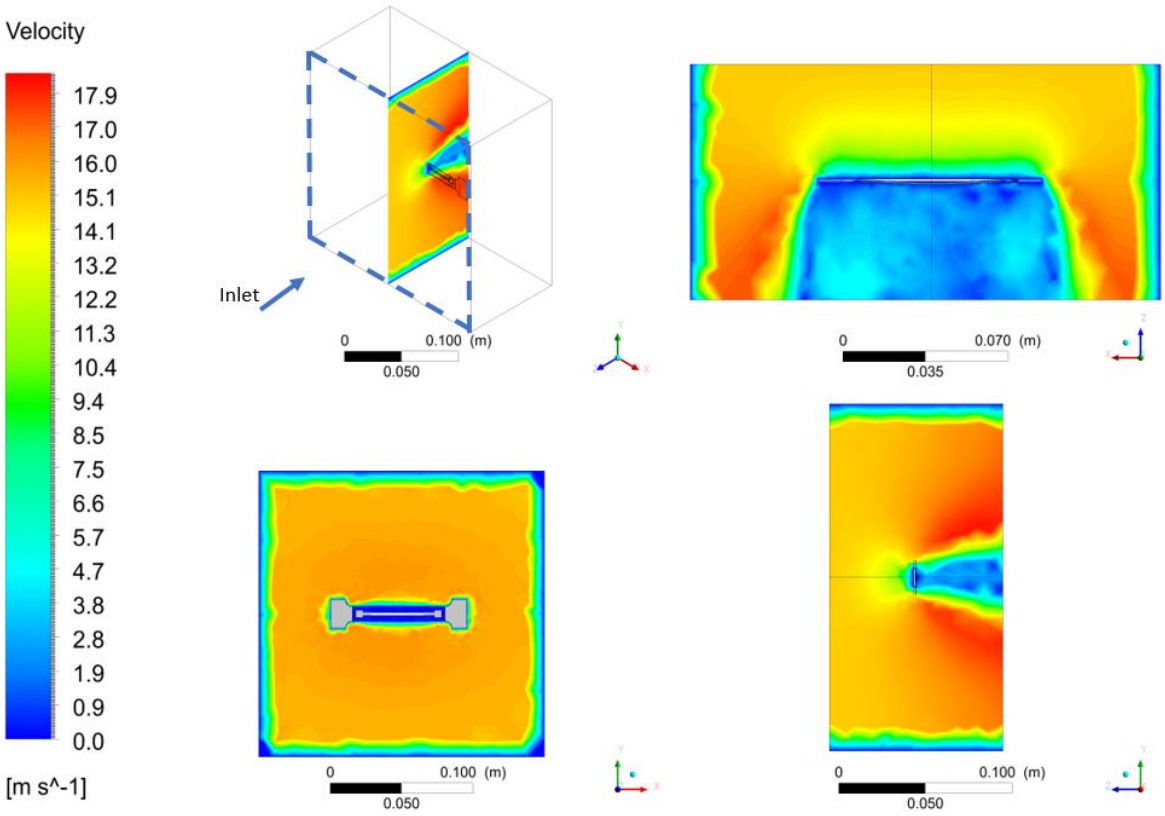


**Figure 3.9:** Isometric view of the wind velocity profile around the 3D−printed sensor.

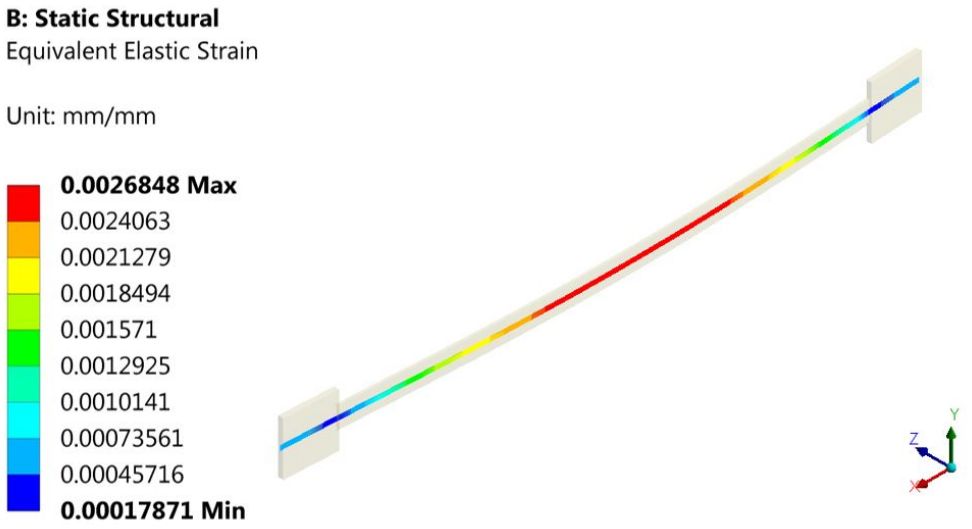


**Figure 3.10:** Strain distribution on the 3D−printed sensing layer at 15 m/s wind speed.

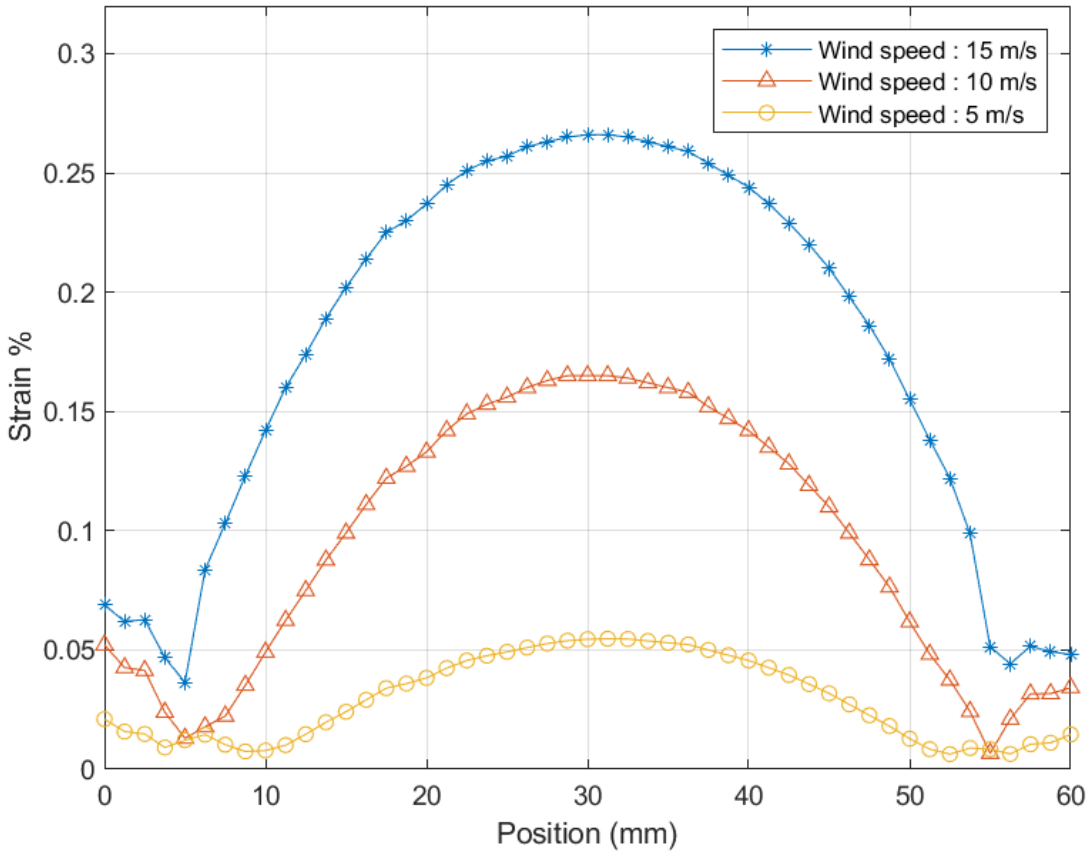


**Figure 3.11:** FEM simulation of the strain distribution on the 3D−printed sensing layer as the wind speed increases.

via a custom−made 3D−printed platform and a standard precision dovetail XY−axis stage (XY-DTS90, Misumi USA). The two stages are fixed on a setup plate (Misumi USA). This setup is fixed at the center of the test champer while its resistance change is measured. Only the ETPU−based sensor in the linear configuration is tested in this experiment due to its high GF (20 in the strain range of 0%−2%) relative to the other 3D−printed sensors.

To compare the simulated result with the FEM simulation, the experiment in Figure 3.5 was repeated with lower strain cycle of (1.25%) and a fitting is found to capture the strain−dependent normalized resistance. This approximation enables one to map the elastic strain from the FEM simulation to the experimental normalized resistance. The curve fitting between the normalized

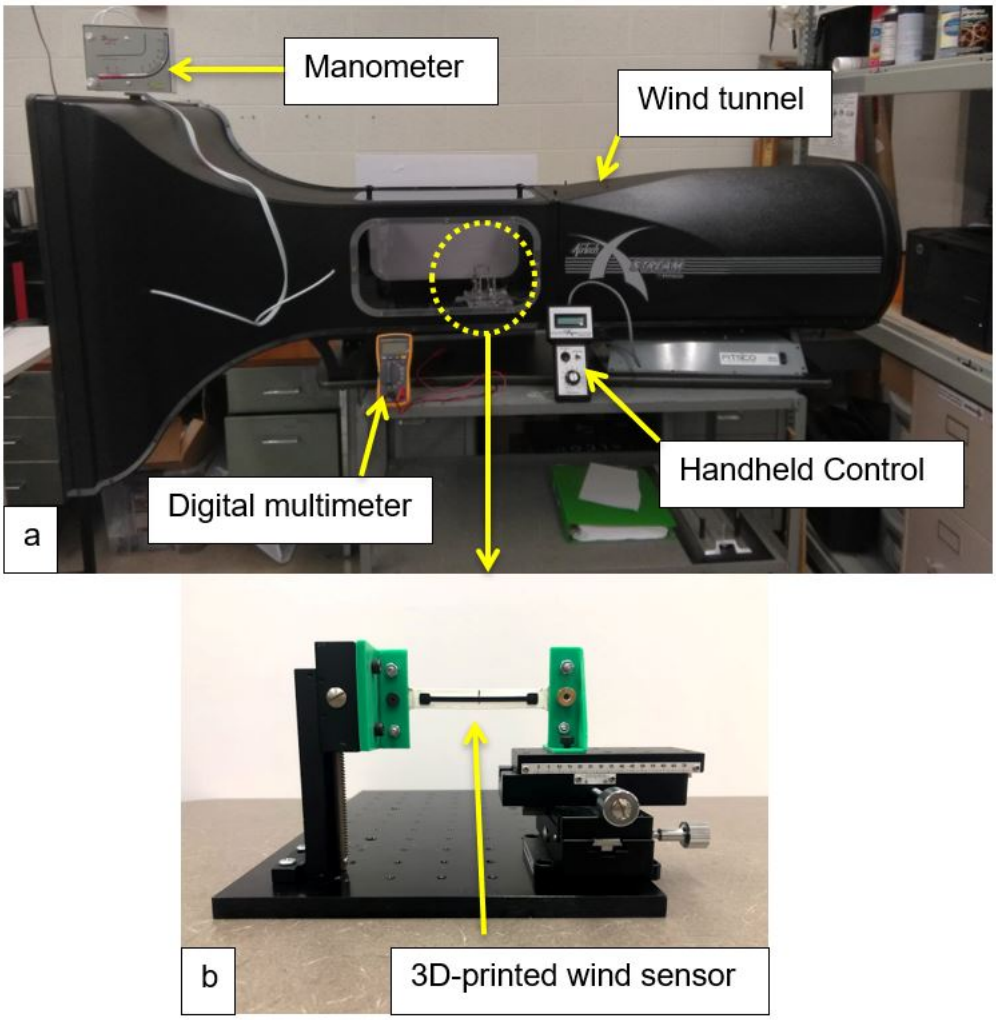


**Figure 3.12:** Wind velocity experiment: a) wind tunnel and b) structure for holding the sensor.

resistance $\Delta R/R$ and the elastic strain $\epsilon$ is as follows: $\Delta R/R = 0.09434\epsilon^2 - 0.261\epsilon + 0.00001254$ as shown in Figure 3.13. Figure 3.14 shows the normalized resistance as the wind velocity is increased and then decreased. It can be seen that the FEM simulation is able to capture the normalized resistance all the way up to the maximum wind velocity, approximately 15 m/s, produced by the wind tunnel.

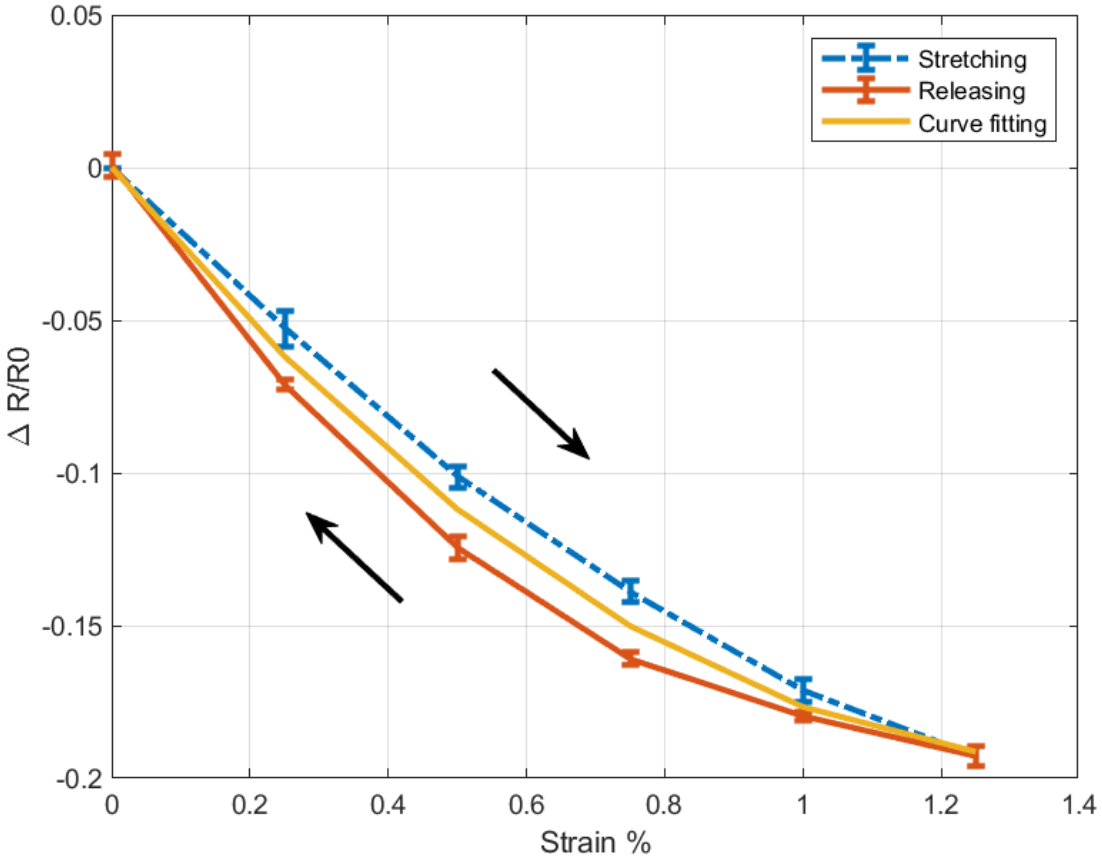


**Figure 3.13:** Normalized resistance change for the ETPU sensor (linear) during five stretching/releasing cycles. a curve is plotted in between the stretching, and releasing cycle which represents an approximation of the normalized resistance−strain relationship.

## 3.5 Conclusion

In this chapter, we proposed 3D–printed stretchable sensors with application to wind sensing. From the experiments results on the three conductive material explored in this work, ETPU was shown to be most promising due to its larger strain range and higher sensitivity. The ETPU–based sensor showed the ability to sense and measure wind speed beyond 3.5 m/s. Using the results from the mechanical tests, FSI simulation was used to couple the wind load with the mechanical deformation of the sensor. The simulation results on the elastic strain behavior of the sensor showed good match with experimental measurements conducted on a prototype in the wind tunnel

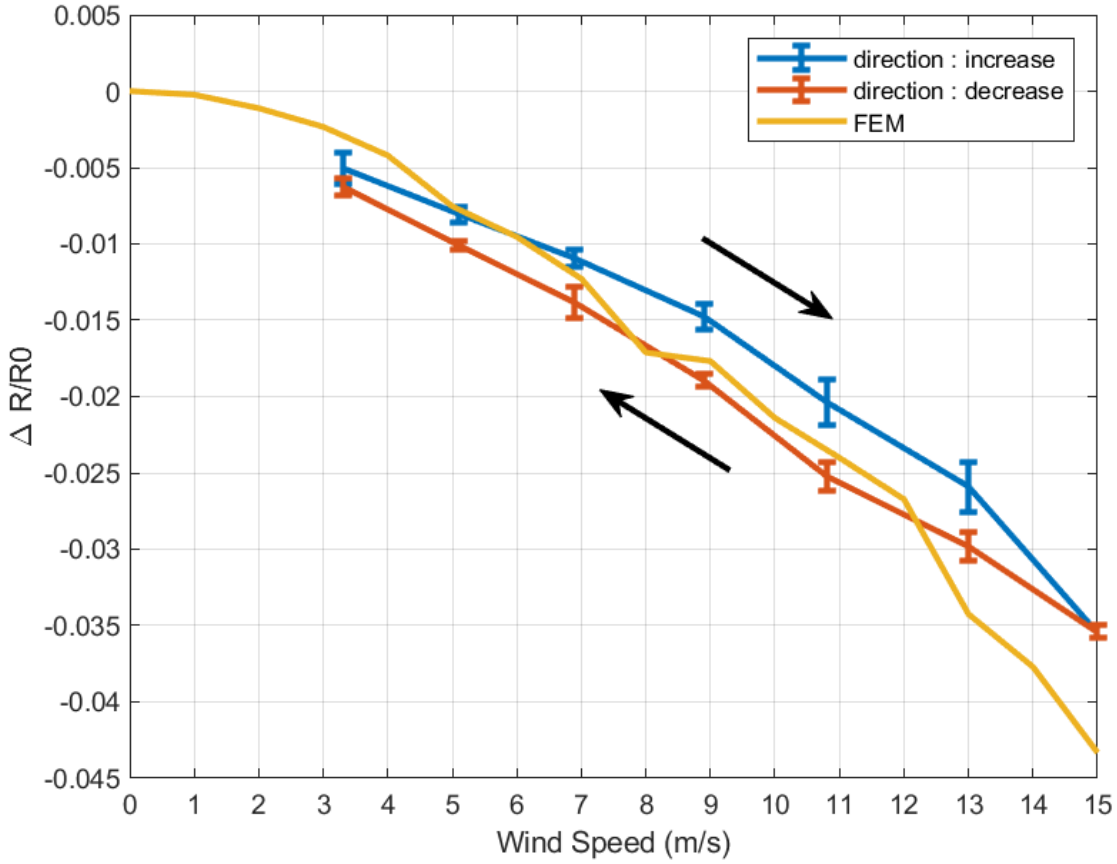


**Figure 3.14:** Measured and FEM prediction of the electrical resistance variation with respect to the wind velocity for the ETPU filament-based wind sensor in the linear configuration.

experiment.

# CHAPTER 4

# DISTRIBUTED MEASUREMENT OF DEFORMATION MAGNITUDE AND LOCATION WITH A PAIR OF SOFT SENSORS

In this chapter, we propose a novel lightweight, inexpensive, and easy-to-fabricate flexible sensor system that can simultaneously measure the magnitude and the location of deformation along a long strip. The system consists of vertical stacking of two sensors, one measuring the location of the deformation and the other measuring its magnitude. Both sensors utilize layers of soft piezoresistive films (Velostat) and copper sheets and their design ensures minimal cross-coupling of the two measured quantities. To put the discussion in context, we consider a configuration where the integrated sensor pair is mounted on an inflatable tube, which is subjected to a kink deformation, the location and magnitude of which can be independently controlled. Finite-element modeling is conducted to capture the deformation under an applied kink, which is subsequently used to predict the measured sensor output based on the characterized strain-resistivity relationship. The validity of the model is verified with data obtained under kinks of different magnitudes. Finally, we show experimental results obtained from a 500 mm long sensor, which support the sensor pair's capability to simultaneously capture the location and magnitude of the kink applied on the inflatable tube. While this work has demonstrated the applicability of the sensor to inflatable structures, with potential applications in extraterrestrial structure habitats [76], inflatable wings [77, 78], and inflatable antennas [79], the proposed sensor system can be readily tailored to custom dimensions and integrated with other substrates such as textiles and elastomers for wearable and soft robot applications.

The remainder of the chapter is organized as follows. The sensor design and the fabrication process of the soft sensing system are first presented in Section 4.1. Finite element modeling and simulation of the deformation and sensor output under a kink stimulus are discussed in Section 4.2, followed by experimental validation including simultaneous measurement of deformation location and magnitude over the long strip (500 mm) in Section 4.3. Finally, concluding remarks are

provided in Section 4.4.

## 4.1 Sensor System Design and Fabrication

Figure 4.1 illustrates the different layers of the proposed soft sensor system. The sensor system consists of a position sensor and a pressure sensor, both of which are fabricated from a commercially available, conductive polymer sheet-like material called Velostat (DESCO Industries), a carbon-impregnated polymer with piezoresistive properties. Its electrical resistance decreases when pressure is applied. The Velostat piezoresistive behavior is due to a change in the distance between conductive carbon particles that occurs when the material is under stress, as shown in Figure 4.2. With an applied pressure, these particles get closer together, and if this material is sandwiched between two conductors, the resultant structure can perform as a pressure or force sensor [80].

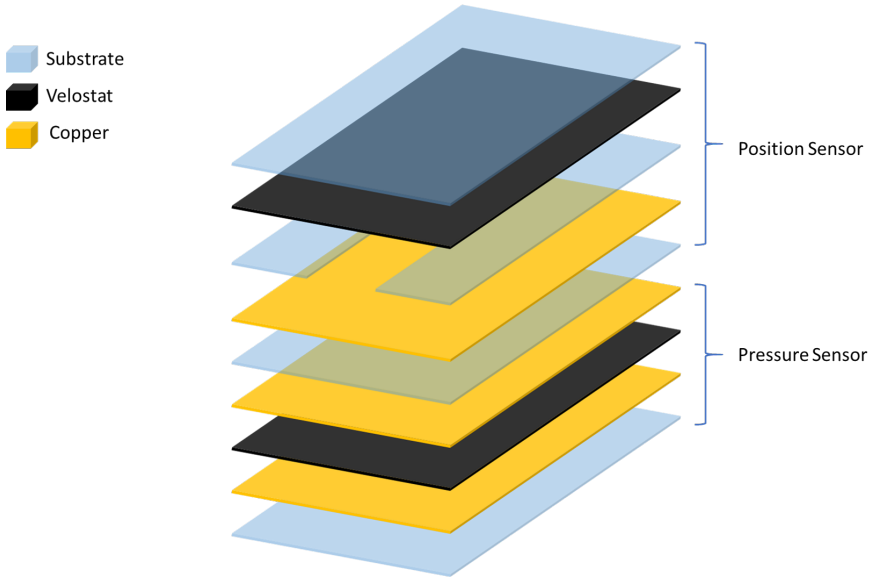


**Figure 4.1:** Illustration of the structure of the proposed flexible sensing system, which involves Velostat, copper tapes, and flexible insulating substrate (adhesive tape).

The pressure magnitude sensor involves one layer of piezoresistive foil sandwiched between two layers of conductive copper sheets. These layers of copper sheets have an extension for allowing the connection with the external measurement circuit. The layers of piezoresistive material are

always larger than the layers of the copper sheets. This is necessary in order to avoid a short circuit between the conductors. Finally, the resultant structure is wrapped with non-conductive adhesive tape (NOPI™, tesa tape inc.).

Since the conductivity of copper ($5.96\times10^7$ S/m) [81] is much higher than that of the piezoresistive layer (0.2 S/m) [82], the sensor resistance can be viewed as parallel connection of piezoresistive elements. As such, when an external loading is applied, it reduces the resistance of the corresponding element, the amount of which depends only on the magnitude of the loading. Due to the nature of parallel connection of the piezoresistive elements, the resulting sensor output will depend only on the loading magnitude, with negligible dependence on where the loading is applied.

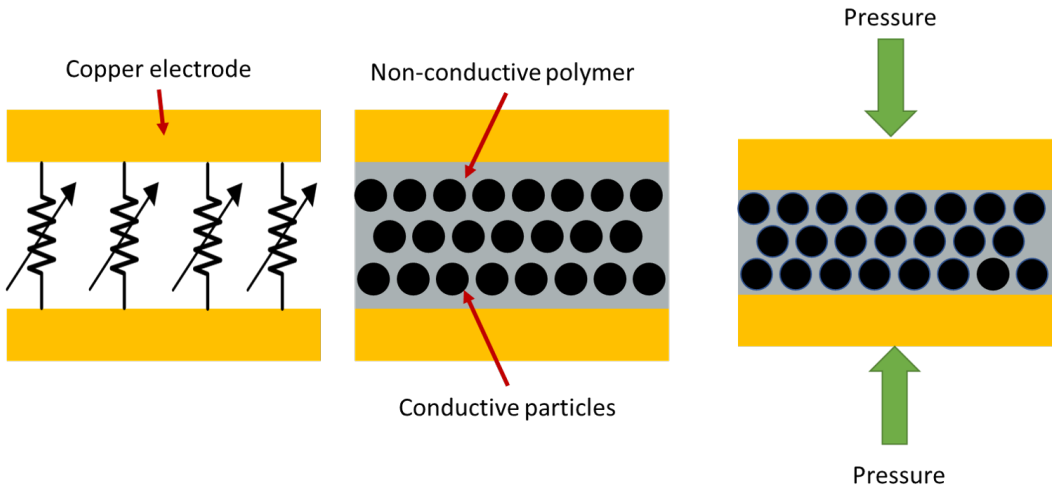


**Figure 4.2:** Schematic view of the piezoresistive pressure sensor.

The position sensor uses the concept of a potentiometer and acts as a variable resistor according to the position at which deformation or loading takes place. The sensor is composed of a fully conductive material (copper) layer, an insulated spacing material, and a flexible piezoresistive film, as shown in Figure 4.3. Once a contact results from the loading, the measured resistance is only dependent on the distance of the contact point C to the base point B, and thus expected to have a linear relationship with the loading point, with minimal influence from the magnitude of the loading (as long as a contact is established). The position-dependent resistance can be readily measured

with a voltage-divider circuit.

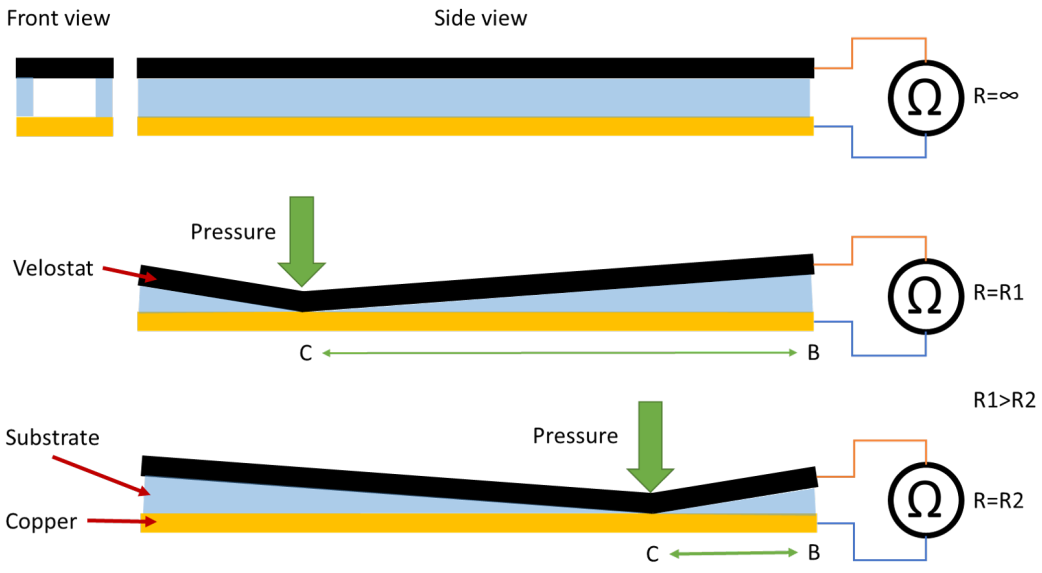


**Figure 4.3:** Schematic view of the piezoresistive position sensor.

## 4.2 Finite Element Modeling and Simulation

In this section, we use material properties to create a finite element method (FEM) model of the soft sensor system. The static structural module in Ansys software is used in this work.

### 4.2.1 Simulation of the Pressure Sensor

First, we study the soft pressure sensor (illustrated in Figure 4.2) and examine its strain response when subjected to deformation, which will be further validated with experimental measurement. Figure 4.4 shows the FEM simulation setup, where an inflatable tube is fixed from both ends, and the soft pressure sensor is bonded on top of it. Both the sensor and the tube are subjected to a deformation caused by a rigid plate that moves in the negative y-direction. The inflatable tube internal pressure is 3 psi and the dimensions and Young's Moduli of all parts in the FEM simulation are listed in Table 4.1.

**Table 4.1:** The dimensions and Young's moduli of the FEM simulation study.

| Part | Material | Length (mm) | Width (mm) | Thickness (mm) | Young's Modulus (MPa) |
|---|---|---|---|---|---|
| Piezoresistive layer | Velostat | 100 | 35 | 0.1 | 180 [83] |
| Spacer | Adhesive tape | 100 | 35 | 0.1 | 270 [84] |
| Conductive layer | Copper | 100 | 35 | 0.07 | 117000 [81] |
| Tube | Nylon | 500 | 150 | 0.4 | 3000 [85] |
| Kink plate | Aluminum | 100 | 150 | 2 | 70000 [81] |

Figure 4.5 shows the deformation profile in the isometric view when the rigid plate pushes in by 10 mm. In the simulation, the Velostat layer is studied as a grid of $7 \times 20$ elements with dimensions 5 mm $\times$ 5 mm $\times$ 0.1 mm for each element. The elastic strain profile on the Velostat layer of the sensor under the 10 mm deformation (at the point touching the rigid plate) is shown in Figure 4.6, which indicates that maximum strain values are in the proximity of the area of contact with the plate. The strain of the sensor will change when the deformation increases or decreases. For example, Figure 4.7 shows the simulated axial strain (average of the 140 elements) of the Velostat layer in the vertical direction for different deformation values, represented by how much (in mm) the rigid plate is pushed into the tube wall. From the figure, one can see that the strain shows a monotonic (and nearly linear) relationship with the magnitude of the applied deformation.

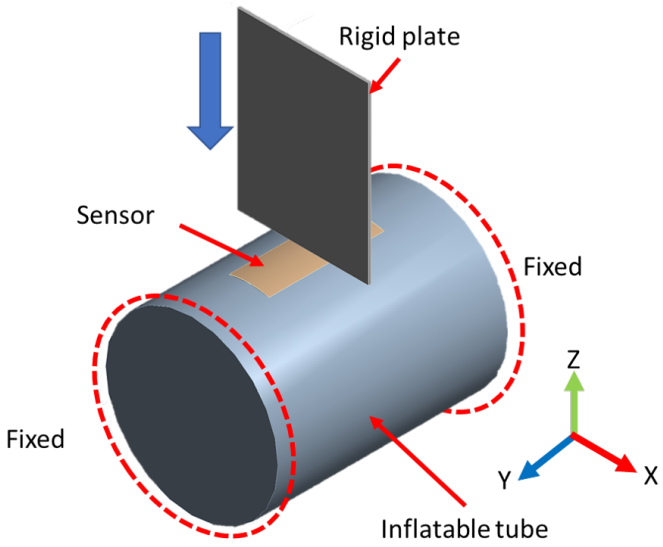


**Figure 4.4:** FEM simulation setup for the soft pressure sensor.

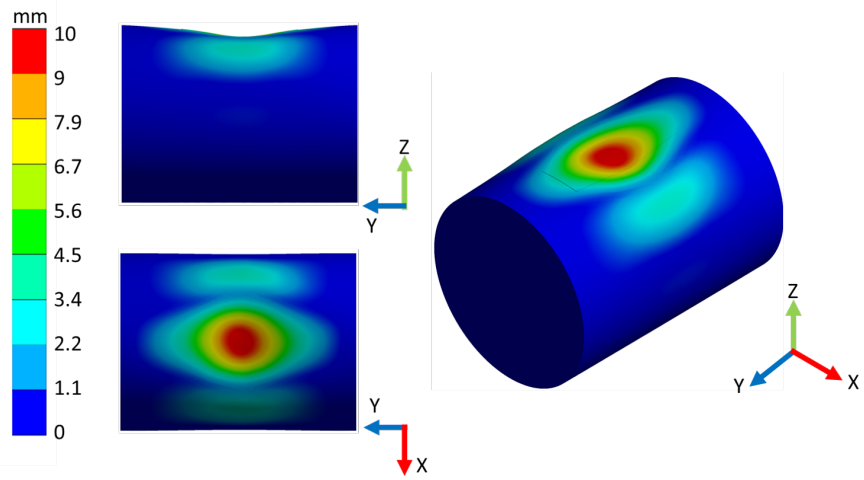


**Figure 4.5:** Isometric view of the deformation profile for the soft pressure sensor under a 10 mm kink imposed by the rigid plate.

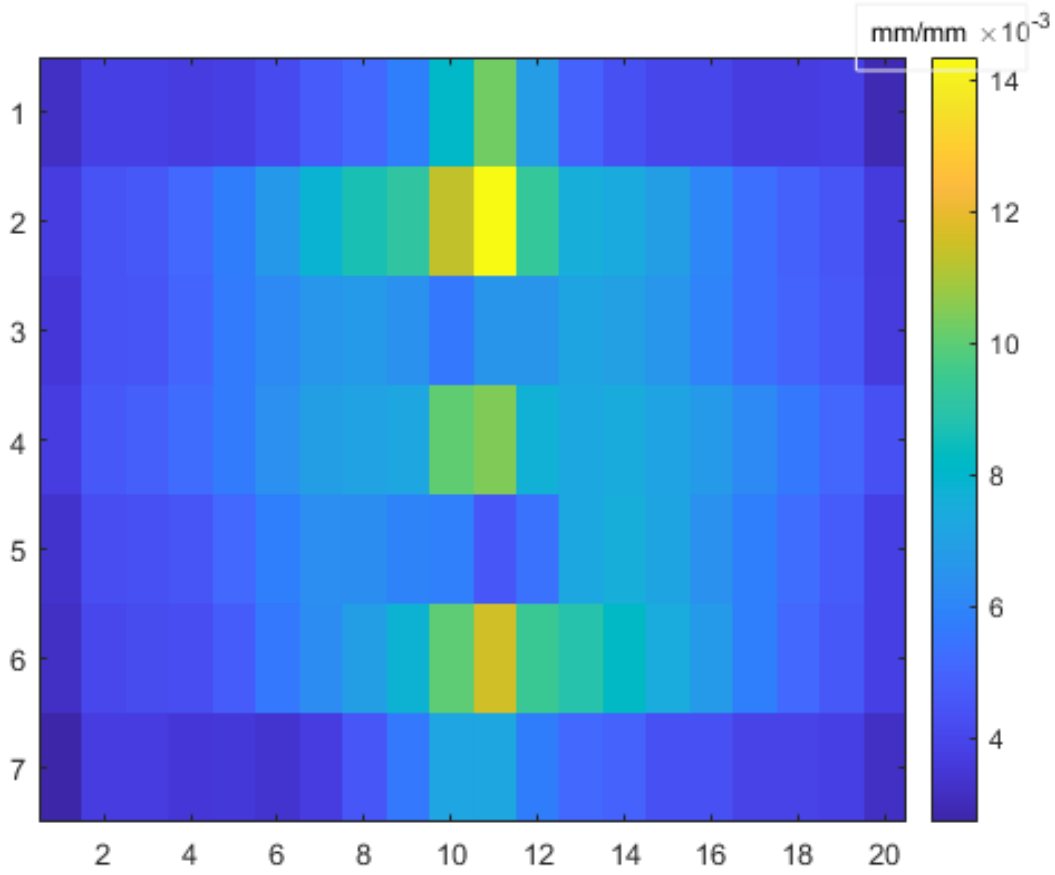


**Figure 4.6:** Strain distribution on the Velostat sensing layer under a 10 mm kink deformation caused by the rigid plate.

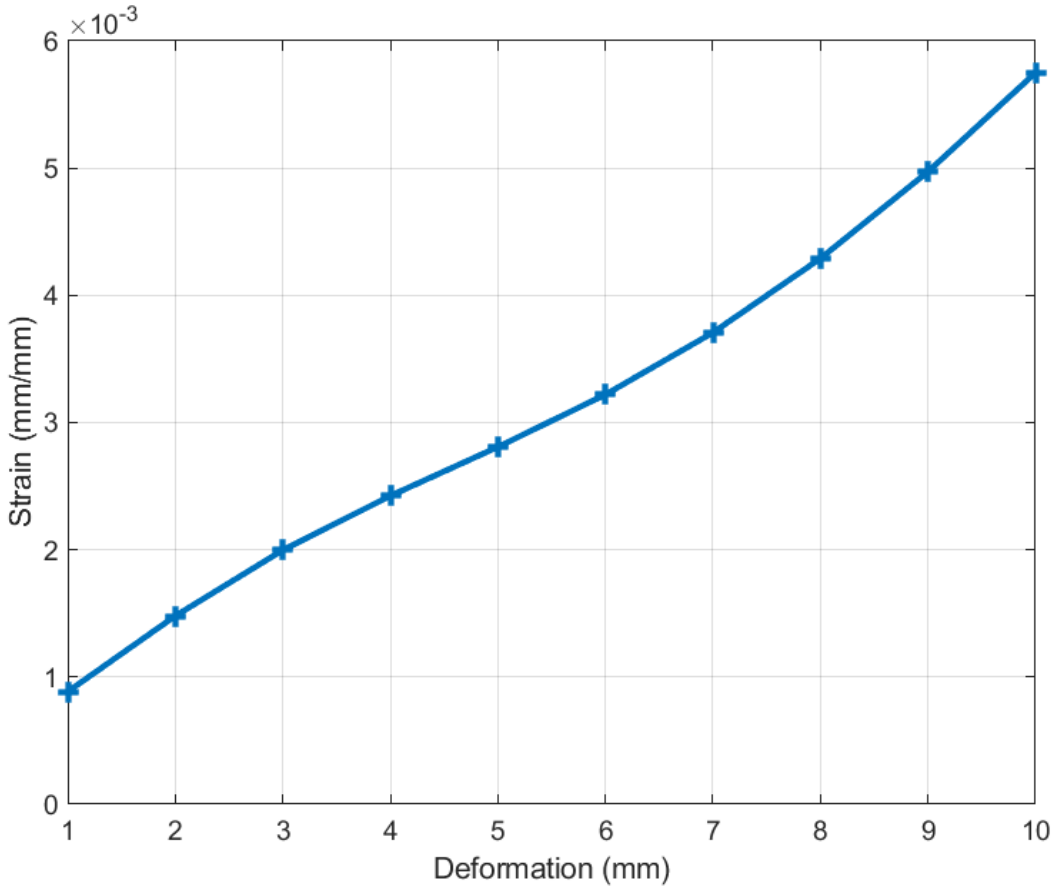


**Figure 4.7:** FEM simulation of the average strain distribution on the Velostat sensing layer as the kink deformation increases.

### 4.2.2 Simulation of the Position Sensor

In the second simulation, we study the soft position sensor (illustrated in Figure 4.3) and examine the contact area between the Velostat layer and the copper layer when subjected to deformation. This simulation uses the same setup as in Figure 4.4 but with focus on the soft position sensor. In particular, we are interested in examining how the kink (or pressure) magnitude might interfere with the contact position measurement. The Velostat and the conductive layers have the same dimensions (34 mm × 100 mm), which sandwich two spacers each with dimensions of 15 mm × 100 mm; refer to Fig 4.3 for illustration. In the simulation, the Velostat layer is studied as a grid of 4 × 100 elements with dimensions 1 mm × 1 mm × 0.1 mm for each element. The area of contact

between the Velostat layer and the copper layer under a given plate-induced kink deformation is simulated. Figure 4.8 shows the results when the imposed kink deformation is 1 mm, 5 mm, and 10 mm, respectively. From the figure, one can see that the applied deformation magnitude does have an impact on the size of the contact area, which subsequently can influence the measured resistance (the distance between the base point B and the closest contact point C in Fig. 3). However, simulation also shows that such impact is minor - for example, for a kink deformation of 10 mm, the position measurement error is at the order of 0.5 mm, which is consistent with experimental observations shown in Section IV.

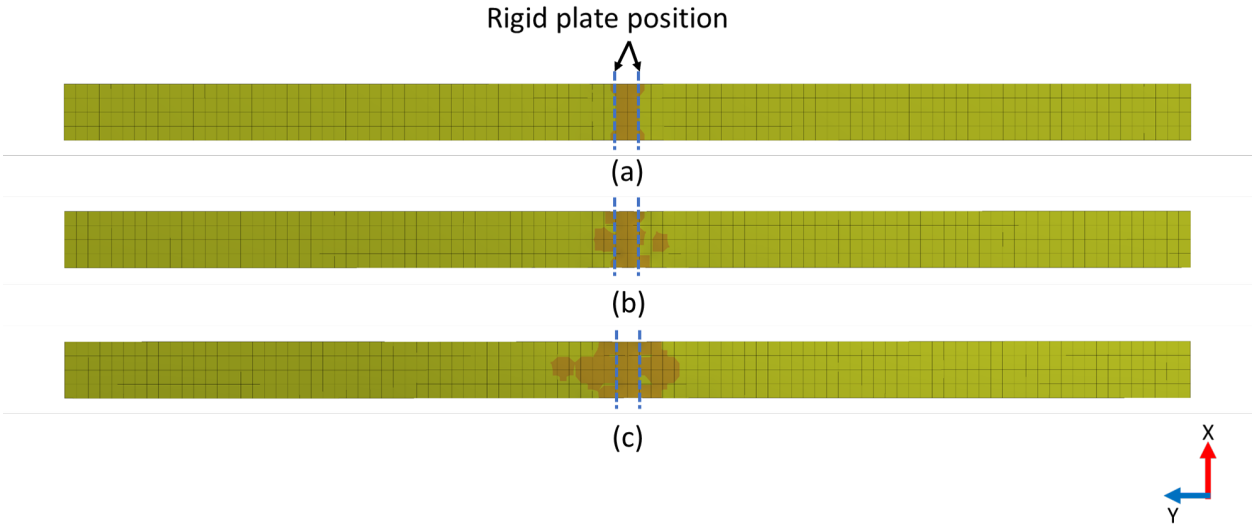


**Figure 4.8:** FEM simulation of the contact area distribution (in orange, shaded) on the Velostat sensing layer when the plate-induced kink deformation is (a) 1 mm, (b) 5 mm, and (c) 10 mm.

## 4.3 Experimental Characterization and Model Validation

To identify the sensitivity of the Velostat piezoresistive material, experiments are implemented to measure the change of resistance in response to the deformation applied. An inflatable tube made with 420D Nylon Fabric from DIY Packraft, USA, is used to test the performance of the flexible sensor system. The inflatable tube has a total length of 100 cm and a cross-sectional radius of 7.5 cm. To introduce deformation to the inflatable tube, an experimental setup shown in

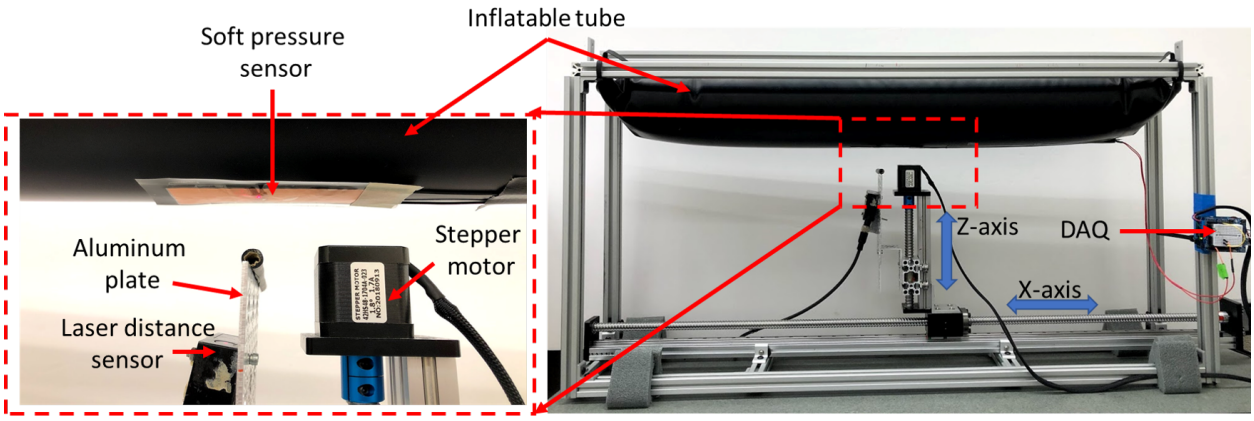


**Figure 4.9:** Experimental setup for exerting the deformation on inflatable tube with controlled position and magnitude.

Figure 4.9 is used. Two linear screw-driven guides, which can move in the vertical and horizontal directions, respectively, are amounted within a rigid cuboid aluminum frame, with both linear screw guides controlled by stepper motors. A rigid plate (150 mm width and 2 mm thickness) is fixed on the vertical linear screw-driven guide to exert a kink-deformation on the tube and the sensor, and the sensor resistances are measured with two voltage divider circuits. The control of the movement of the rigid plate during the experiments and the data acquisition are implemented with a microcontroller (model number A000073, Arduino).

### 4.3.1 Experiments on Magnitude Sensor

First we mount a soft pressure sensor patch alone with dimensions of 35 mm × 100 mm on the inflatable tube shown in Figure 4.10 to validate the FEM results from the previous section. A formulation developed by Zhang *et al.* [86] is further utilized to compare the experimental result with the FEM simulation. The formulation is developed for modeling the dependence of electrical resistivity of semiconductive polymer composites on an applied load:

$$\frac{R}{R_0} = (1-\varepsilon)e^{-\gamma D\varepsilon[(\pi/(6\phi))^{1/3}-1]} \tag{4.1}$$

$$\gamma = \frac{4\pi}{h}\sqrt{2m\varphi} \tag{4.2}$$

where $R$ is the resistance under an imposed strain, $R_0$ is the initial resistance, $\varepsilon$ is the strain, $D$ is the filler particle diameter, $\phi$ is the volume fraction of filler particles, $m$ is electron mass, $\varphi$ is the height of the potential barrier between two adjacent filler particles, and $h$ is Plank's constant. The parameters used in this works are listed in Table 4.2.

**Table 4.2:** Parameters for the model in Eq. (1) and (2).

| | | |
|---|---|---|
| Volume fraction of carbon particle | $\phi$ | 0.2873 [86] |
| Diameter of carbon particle | D | $500 \times 10^{-9}$ m [86] |
| Potential height of carbon black and polyethylene | $\varphi$ | $8.01 \times 10^{-21}$ Joule [86] |
| Planck's constant | h | $6.6 \times 10^{-34}$ $m^2$kg/s [87] |
| Electron mass | m | $9.1 \times 10^{-31}$ kg [88] |

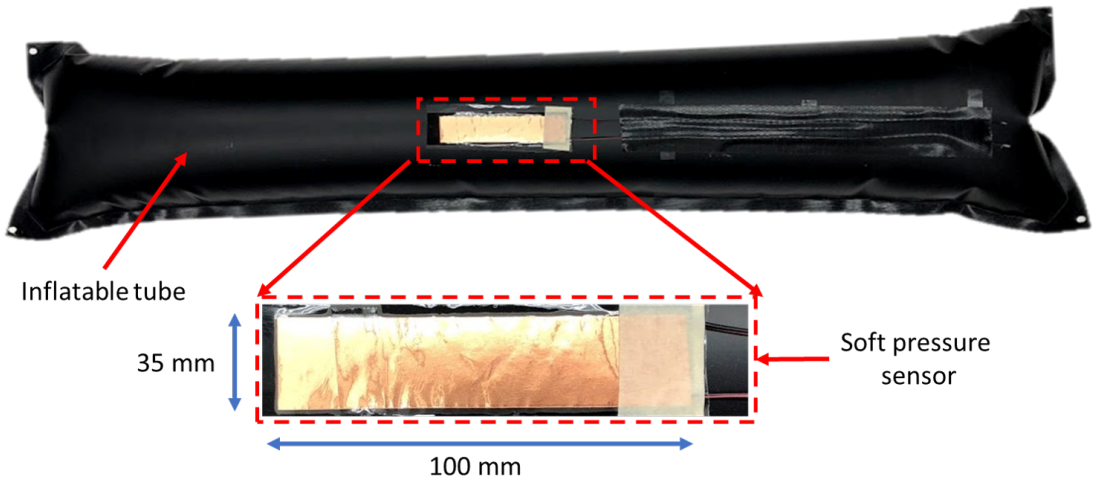


**Figure 4.10:** Experimental tube mounted with a 100 mm long soft pressure sensor patch.

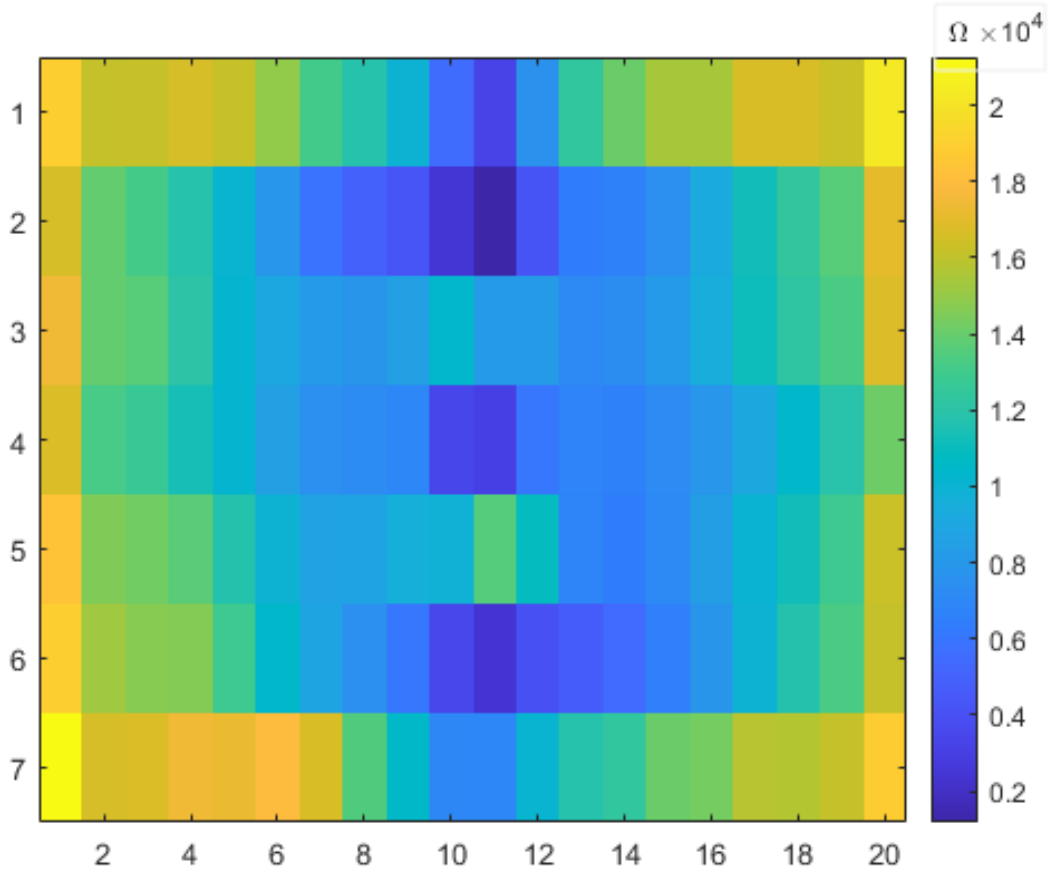


**Figure 4.11:** Calculated resistance distribution for the Velostat sensing layer at 10 mm deformation.

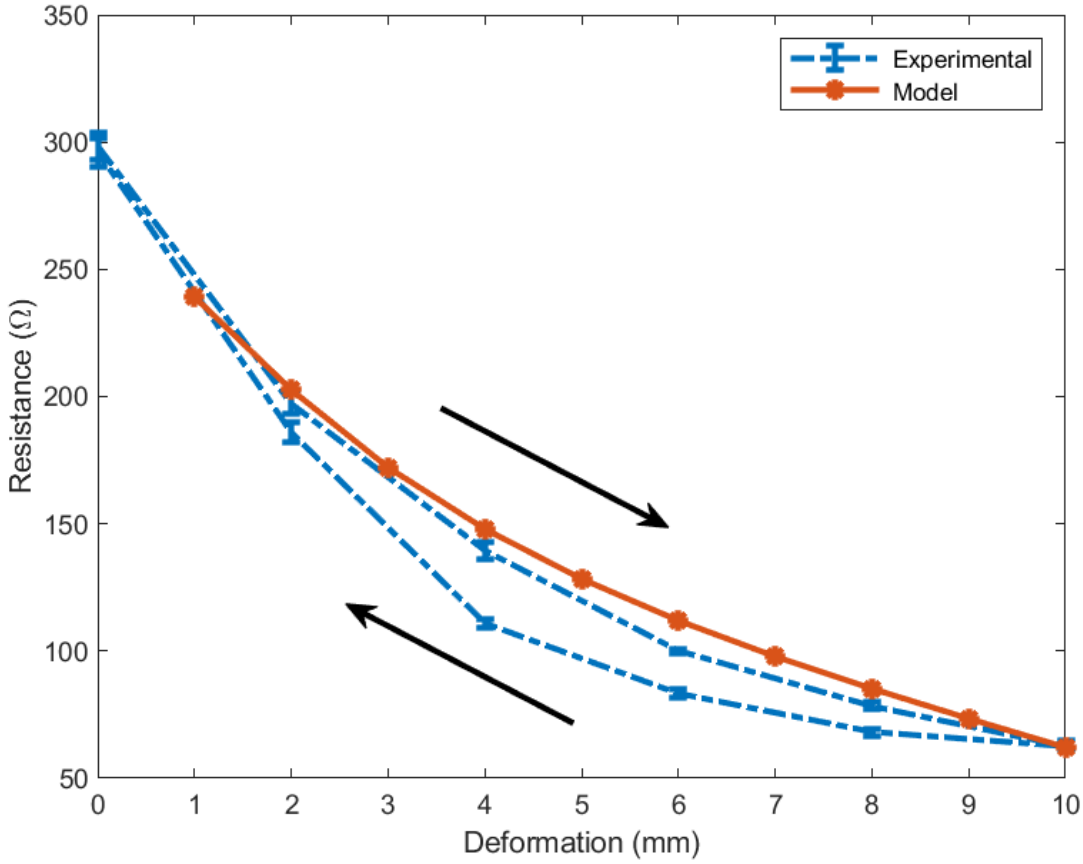


**Figure 4.12:** Measured and FEM prediction of the electrical resistance variation with respect to the deformation for the Velostat pressure sensor. The measured resistance shown is the average of five measurements; also shown is the standard deviation of those measurements at each kink deformation.

Eq. (5.1) enables one to map the elastic strain from the FEM simulation to the experimental resistance. The calculated resistance profile of the Velostat layer under a kink deformation of 10 mm deformation is shown in Figure 4.11, which indicates that the minimum resistance value is around the center of the contact area. To calculate the equivalent total resistance of the Velostat layer, the segments are considered to be in parallel connection with each other. Figure 4.12 shows the average of the five measured resistance values as the deformation is increased and then decreased, along with its comparison to the predictions by the FEM model. It can be seen that, while the FEM simulation does not capture the modest hysteresis observed in experiments, it is able to predict well

the resistance output in general, all the way up to the maximum applied kink deformation of 10 mm.

To characterize the cyclic stability, the soft pressure sensor is further tested by measuring the resistance under repeated cycles of deformation from 0 to 10 mm with a steps of 2 mm and the kink deformation speed for the experiment is 0.5 mm $s^{-1}$ as shown in Figures 4.13. The tested sensor exhibits some transient behavior, but the responses are largely stabilized after the first 2000 seconds (200 cycles). The transient time varies with the magnitude of the cyclic stimulus as presented in [89].

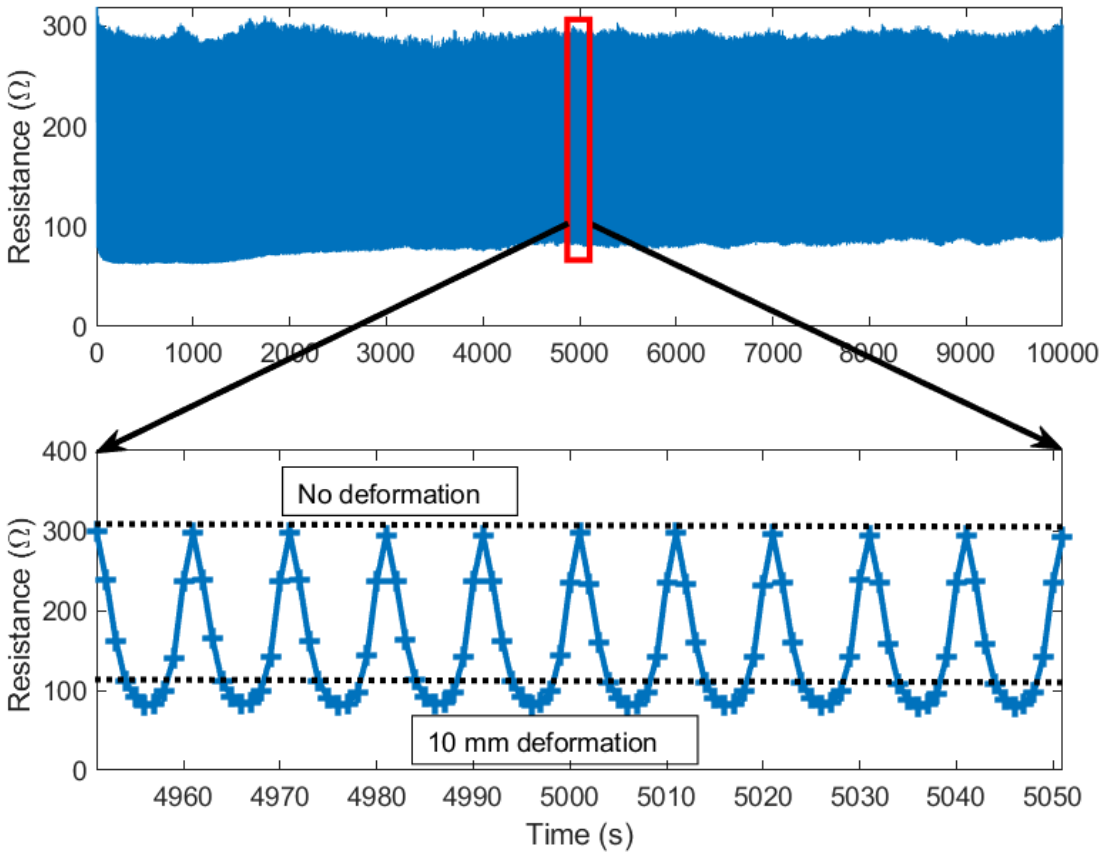


**Figure 4.13:** Change in resistance for the Velostat conductive films during cycles of applying and releasing deformation.

### 4.3.2 Experiments on Full Sensor System

Additional experiments are conducted to test the proposed sensing system composed of both sensor units as shown in Figure 4.1. The sensing system is bonded to the inflatable tube, as shown in Figure 4.14. The final dimensions of the fabricated sensor system is 35 mm wide, 500 mm long, with a total thickness of 0.7 mm. During the experiment, rigid plate-induced kink deformations of 5 mm, 10 mm, and 15 mm are applied on the tube every 10 mm along the tube, throughout the full sensor length of 500 mm. The results from the position sensors (Figure 4.15) show an almost linear relationship between the sensor output and the location of the deformation applied. In particular, it can be seen that the position sensor output is largely consistent when different magnitudes of deformation is applied at the same location, which shows the decoupling of the position sensor measurement from the applied loading. In particular, while at each location, the measured sensor output is slightly lower with a larger deformation, which is consistent with the simulation, the differences caused by the deformation magnitude is negligible, also consistent with the simulation finding.

Figure 4.16 shows the output of the deformation magnitude sensor during the same set of experiments. It can be seen that, under the same magnitude of kink deformation, the sensor output is largely consistent when the deformation is applied at different locations. The standard deviations (for five experiments) in this setup are also small. Combining the outputs from both sensors thus will provide simultaneous measurement of the position and the magnitude of the kink deformation along the inflatable structure.

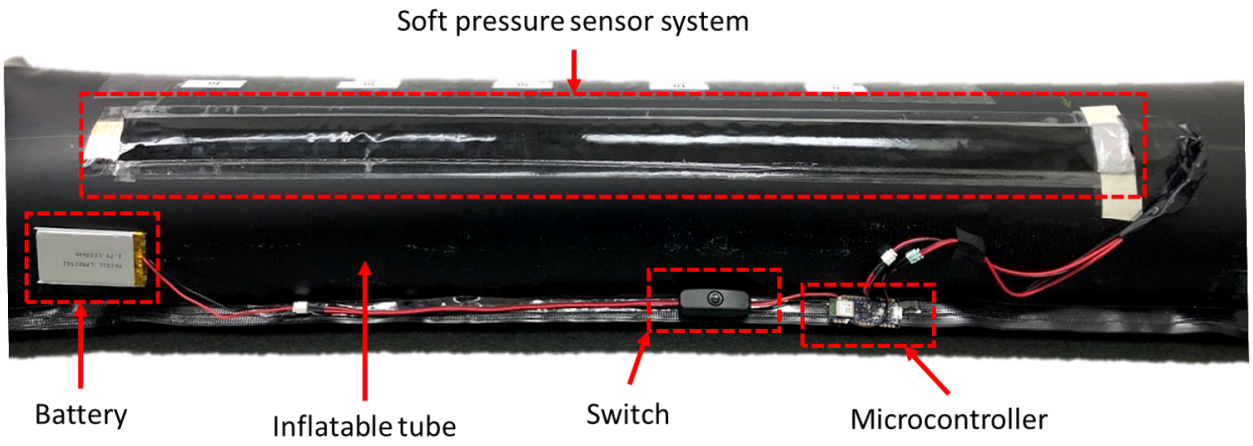


**Figure 4.14:** Experimental tube mounted with a 500 mm long sensor system.

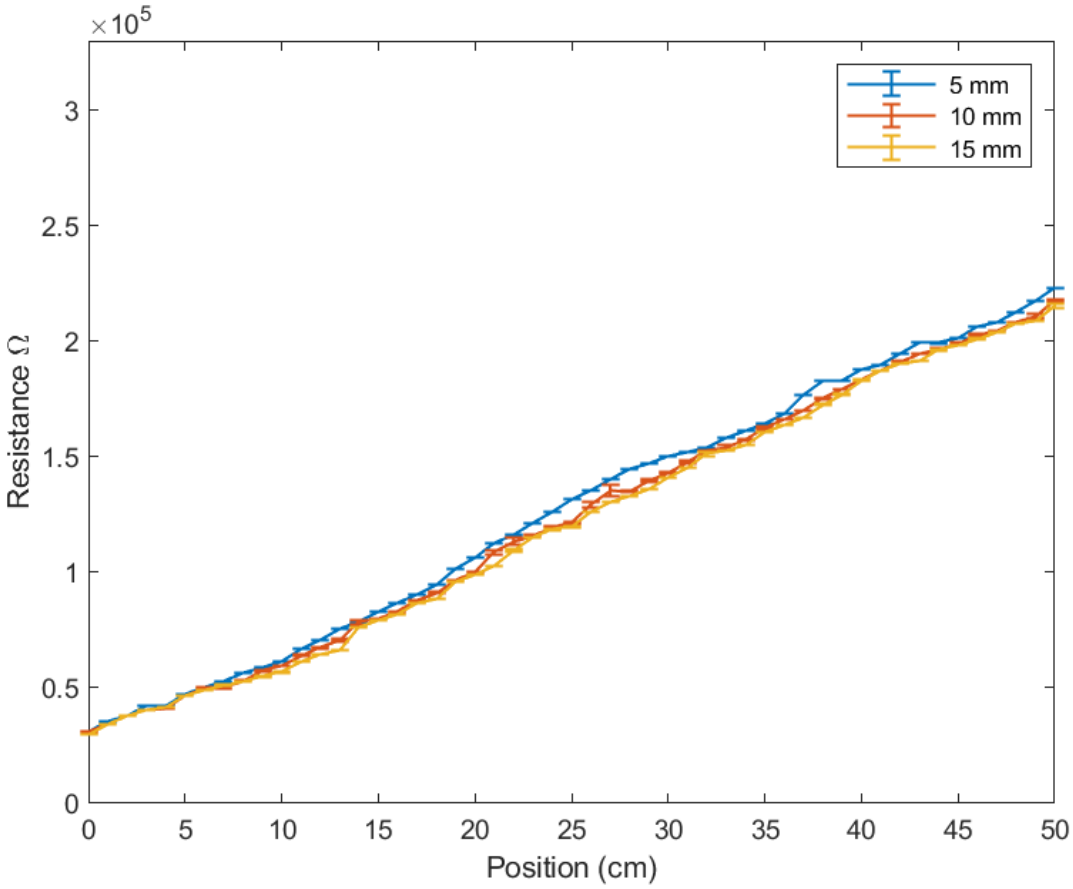


**Figure 4.15:** The position sensor output when the deformation is applied along the tube, where each curve represents the results obtained under a given amount of kink deformation.

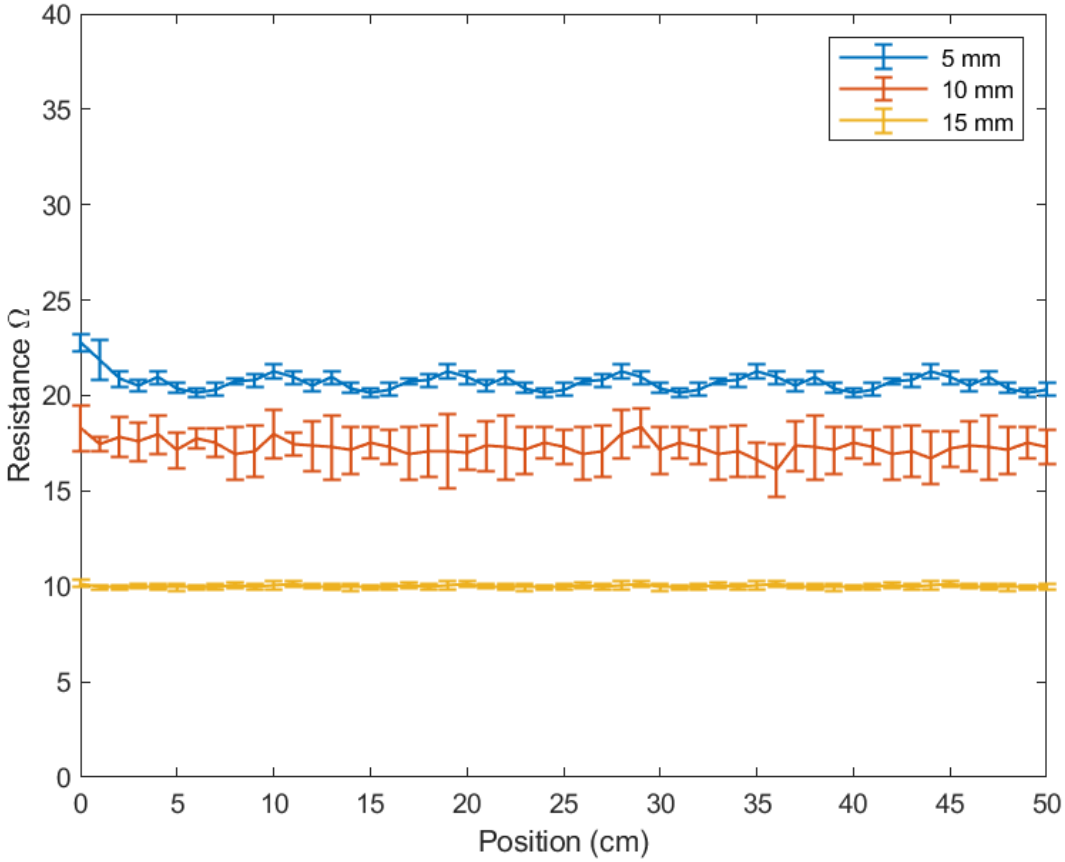


**Figure 4.16:** The magnitude sensor output when the kink deformation is applied along the inflatable tube, where the experimental curve represents the results obtained under a given amount of kink deformation and the average curve represents the average of all the data collected at the corresponding deformation.

## 4.4 Conclusion

In this chapter, we developed and investigated a soft pressure sensor system for detecting simultaneously the magnitude and location of deformation. Using FEM modeling and experiments, Velostat, was selected to demonstrate the proposed sensor system. This sensor system is useful in various applications due to its simplicity in fabrication, robust mechanical properties, and low cost. The simulation results on the sensor showed a good match with experimental measurements. A prototype of the sensor system with a length of 50 cm was constructed and evaluated experimentally.

# CHAPTER 5

# MODELING AND CONTROL OF POLYVINYL CHLORIDE (PVC) GEL ACTUATORS

In this chapter, we present a data-driven modeling approach to capture the observed nonlinear dynamics of PVC gel actuators, where the voltage input – displacement output frequency response shows pronounced dependence on the input amplitude and bias. A Hammerstein-type model is proposed, where a polynomial nonlinearity precedes a linear system, and the identification procedure for the model is presented. In particular, the linear system is identified based on the empirical frequency response of the actuator at a relatively low input amplitude, and the coefficients of the polynomial nonlinearity are determined via a least-squares minimization procedure. The effectiveness of the proposed nonlinear model is supported by its capability to predict the experimentally observed dynamic responses under inputs of different amplitudes and biases. The obtained model is used to design a control scheme for the PVC gel actuator to achieve desired motion tracking performance, as supported by experimental results.

The remainder of the chapter is organized as follows. The PVC gel membrane fabrication process is first presented in Section 5.1. The modeling approach is discussed in Section 5.2, followed by the controller design in Section 5.3. Section 5.4 presents the experimental results. Finally, concluding remarks are provided in Section 5.5.

## 5.1 PVC Gel Membrane Fabrication

The PVC gel microstructure was studied by [51]. The gel contains PVC polymer chains loosely connected via physical crosslinking, with the internal space of the polymer chain matrix being filled with a plasticizer (Fig. 5.1). When no electric field is applied, the PVC gel dipoles have no preferred orientation; however, under an applied electric field, the plasticizer molecules are polarized and dipole rotation of the PVC chains occurs, pulling the PVC gel toward the anode. PVC gel membranes are cast, with thicknesses ranging from hundreds of micrometers up to several millimeters.

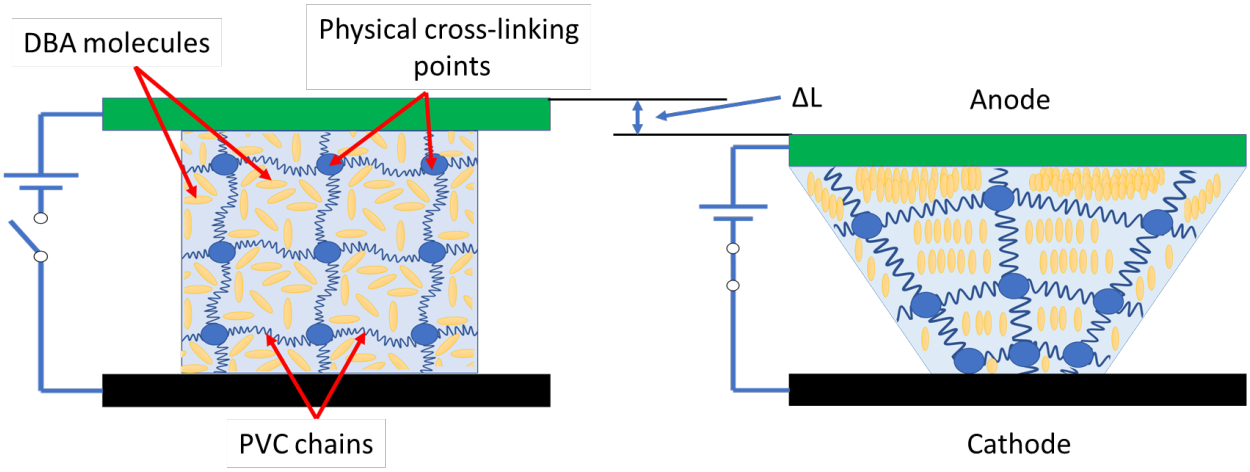


**Figure 5.1:** Schematic diagram of PVC gel internal structure and its change with an applied electric field.

The fabrication process of the electroactive PVC gel is illustrated in Fig. 5.2 (a). First, PVC powders and DBA (Sigma-Aldrich, St. Louis, MO, USA) plasticizer are poured into the tetrahydrofuran (THF) solvent (Sigma-Aldrich, St. Louis, MO, USA). The solution is stirred for four hours at 50 °C to fully dissolve the PVC and the DBA in the THF solvent. To fabricate a flat, transparent PVC gel membrane, the fully dissolved solution is then poured into a glass petri dish and sits at room temperature for approximately 48 h, until the solvent THF has evaporated.

The fabricated PVC gel membrane is transparent, soft, pliable, and lightweight; see Fig. 5.2(b). The weight ratio of PVC to DBA can be adjusted to alter the material characteristics of the membranes, and in this study a weight ratio of 1:8 (PVC to DBA) is used.

## 5.2 Modeling Approach

This section describes the proposed system identification process used to model the nonlinear dynamics of a contraction-type PVC gel actuator. Firstly, we describe the experimental setup for data collection. We then explain the nonlinear system identification approach using the describing function method [90].

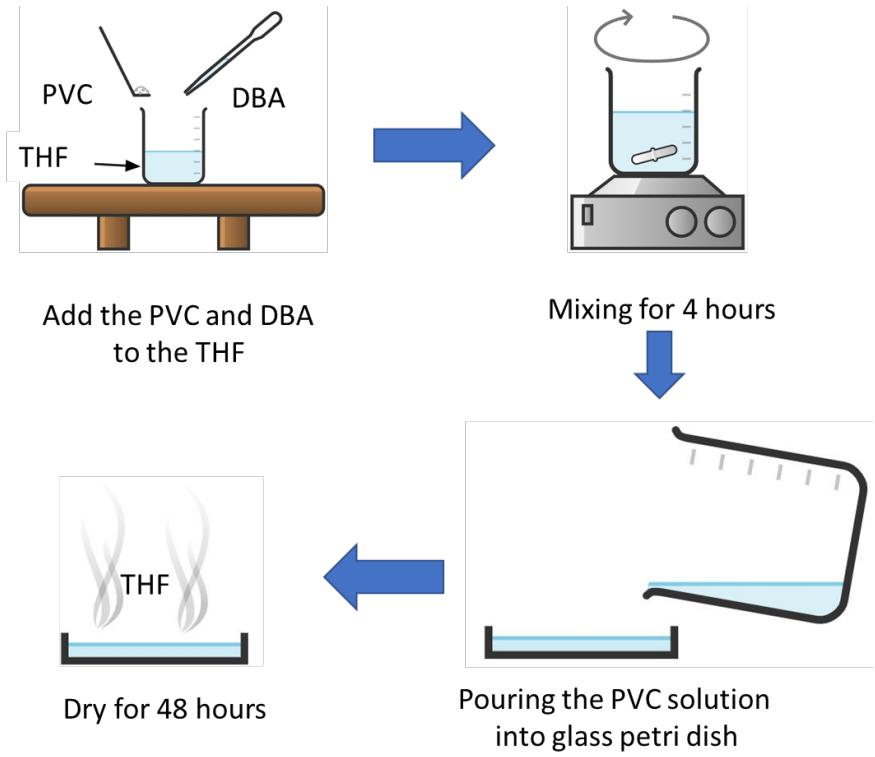


**(a)**

**(b)**

**Figure 5.2:** (a) Process of preparation of PVC gel membrane; (b) A photograph of a fabricated PVC gel membrane.

### 5.2.1 Experimental Setup

The experimental data used in this study is obtained by actuating a PVC gel actuator, where the voltage is the input and the displacement measured as the output. The experimental setup is shown in Fig. 5.3. The actuator consists of a PVC gel membrane placed between a stainless-steel mesh anode and a cathode made from stainless-steel foil, as shown in Fig. 5.3 (a). The thickness of each layer is shown in Table 5.1. When a DC field is applied, the PVC gel exhibits an anodophilic deformation onto the mesh anode, with the gel moving into the holes in the mesh. This causes a bulk contraction of actuator to occur in the thickness direction. When the DC field is removed, the actuator quickly moves back to its original shape as a result of the gel's elasticity. A laser displacement sensor (OADM20I6441/S14F, Baumer Electric) is mounted above the actuator to measure the displacement. A high voltage amplifier (AMJ-2B20 from Matsusada Precision) is used to drive the actuator. A dSPACE system is used for control signal generation, sensing data acquisition, and processing.

### 5.2.2 Dynamic Modeling

The describing function method is considered an extended version of the frequency response method, and it can be used to approximately analyze and predict nonlinear behaviors [90]. The describing function of a nonlinear system, $N(A, \omega)$, is defined to capture the gain and phase shift between the fundamental harmonic component of the output and a sinusoidal input:

$$N(A, \omega) = \frac{Y}{A} \angle \phi \tag{5.1}$$

where $A$ and $\omega$ represent the amplitude and the angular frequency of the sinusoidal input, re-

**Table 5.1:** Thicknesses of PVC gel actuator layers.

| Layer | Material | Thickness | Units |
|---|---|---|---|
| Anode | stainless steel mesh | 1 | mm |
| Membrane | PVC gel | 1 | mm |
| Cathode | stainless steel foil | 0.5 | mm |

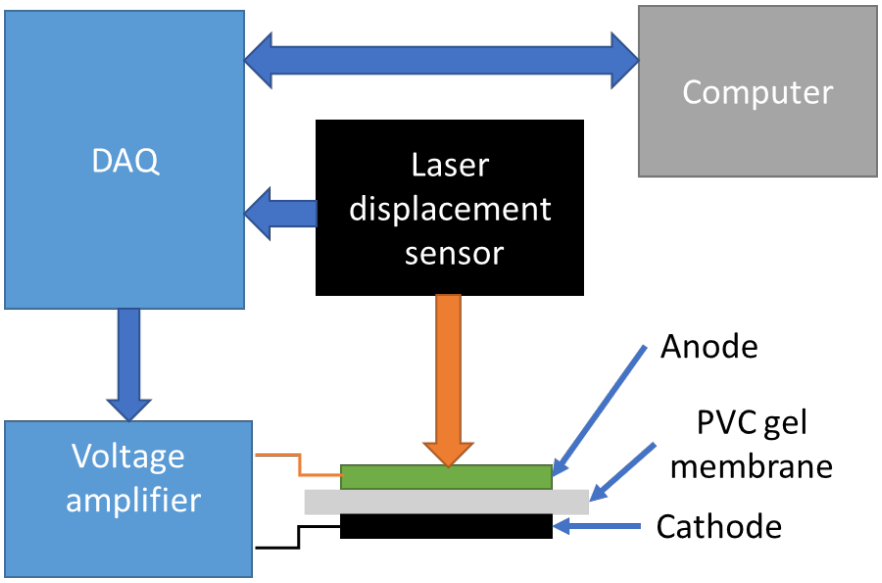


**(a)**

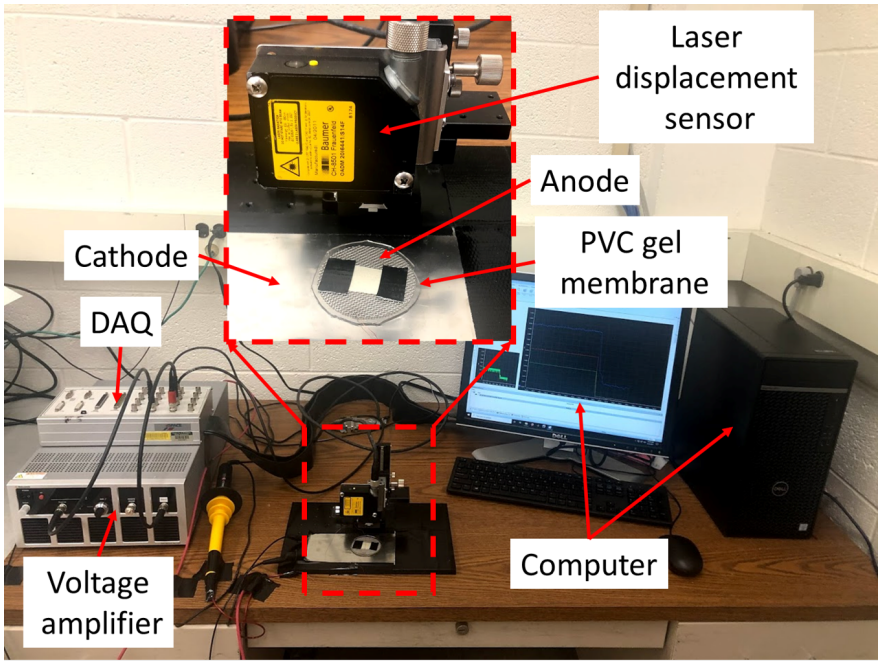


**(b)**

**Figure 5.3:** Experimental setup for characterizing the PVC gel actuator. (a) Schematic, (b) actual setup.

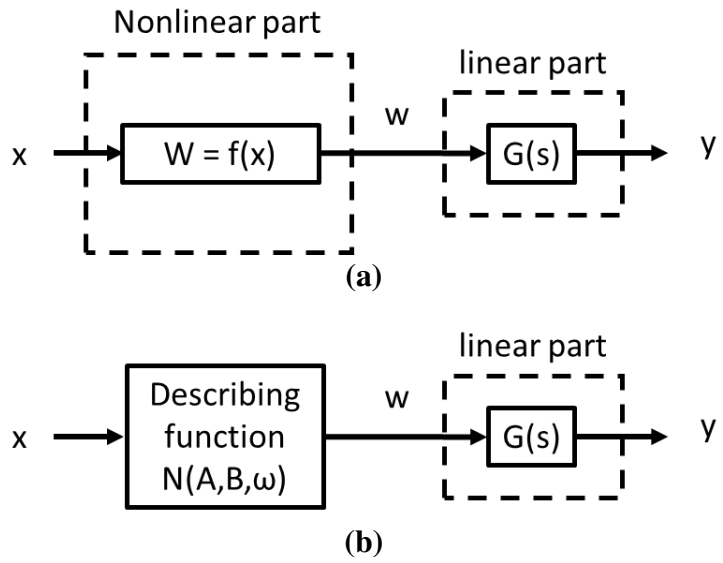


**Figure 5.4:** (a) Proposed Hammerstein model structure for PVC gel actuator dynamics; (b) Use of the describing function of the nonlinear element for system identification.

spectively, $Y$ denotes the amplitude of the fundamental harmonic component of the output, and $\phi$ denotes the phase shift of the fundamental harmonic component of the output with respect to the sinusoidal input.

The PVC gel actuator shows dynamic behavior that is dependent on the amplitude and the bias of the voltage input (see the measured frequency responses in Fig. 5.8). In this paper we propose to capture such nonlinear dynamics with a Hammerstein model structure, i.e., a static nonlinearity followed by a linear time-invariant (LTI) system, as illustrated in Fig. 5.4(a). While typical describing functions only consider the dependence on the input amplitude $A$, we introduce a describing function that depends on both the input amplitude $A$ and bias $B$, $N(A, B, \omega)$. One could have a wide range of choices for the nonlinearity $f(x)$. In this work we consider the form of odd polynomials:

$$w = f(x) = \sum_{i=1}^{n} c_i x^{2i-1} \tag{5.2}$$

for some $n \geq 1$, where $c_i$, $i = 1, \cdots, n$, are coefficients.

We first illustrate the computation of the describing function $N(A, B, \omega)$ with an example of

$n = 2$, where

$$w = c_1 x + c_2 x^3 \tag{5.3}$$

Given an input $x(t) = B + A\sin(\omega t)$, the output $w(t) = c_1(B + A\sin(\omega t)) + c_2(B + A\sin(\omega t))^3$ can be expanded as a Fourier series, with the fundamental frequency term represented as

$$w_1(t) = a_1\cos(\omega t) + b_1\sin(\omega t) \tag{5.4}$$

Because $f(x)$ is an odd function, one has $a_1 = 0$, and the coefficient $b_1$ is evaluated as

$$\begin{aligned} b_1 &= \frac{1}{\pi}\int_{-\pi}^{\pi}\left[c_1(B + A\sin(\omega t)) + c_2(B + A\sin(\omega t))^3\right]\sin(\omega t)d(\omega t) \\ &= c_1 A + 3c_2\left(B^2 + (\frac{A^3}{4})\right) \end{aligned} \tag{5.5}$$

Therefore, we have

$$w_1(t) = \left[c_1 A + 3c_2\left(B^2 + (\frac{A^3}{4})\right)\right]\sin(\omega t) \tag{5.6}$$

and the describing function as

$$N(A, \omega) = c_1 + 3c_2(\frac{B^2}{A} + (\frac{A^2}{4})) \tag{5.7}$$

Note that due to the odd nature of this nonlinearity, the describing function is real, with no phase shift between its output and input for any frequency $\omega$.

For the LTI system $G(s)$ in Fig. 5.4, one can identify it based on the measured frequency response when the input amplitude is relatively small. We now describe how to use $G(s)$, along with the describing function for the nonlinear element (parameterized with $c_i$, $i = 1, \cdots, n$), to identify $c_i$ based on experimentally measured frequency responses at different input amplitudes.

Let the frequency response of $G(s)$ be denoted as

$$G(j\omega) = M_L(\omega)\angle(\omega) \tag{5.8}$$

The overall gain for the Hammerstein system in Fig. 5.4 can be represented as

$$\begin{aligned} M_s(A, B, \omega) &= N(A, B, \omega)M_L(\omega) \\ &= \sum_{i=1}^{N} c_i h_i(A, B, \omega) \end{aligned} \tag{5.9}$$

where $h_i(A, B, \omega)$, $i = 1, \cdots, n$, represent the describing function terms associated with $c_i$. For example, when $n = 2$, from Eq. (5.7), $h_1 = 1$, $h_2 = 3(\frac{B^2}{A} + \frac{A^2}{4})$.

Now suppose that there are $N \geq n$ measurements of the overall system gain, $\{d_k(A_k, B_k, \omega_k)\}_{k=1}^{N}$, collected under different combinations of input frequencies $\omega_k$, amplitudes $A_k$, and biases $B_k$. We can then aim to find the set of coefficients $\{c_i\}_{i=1}^{n}$ by matching collectively the measurements $\{d_k\}_{k=1}^{N}$ to the model predictions $\{M_s(A_k, B_k, \omega_k)\}_{k=1}^{N}$ via the least-squares optimization. In particular, we formulate the following optimization problem

$$\min_{C} \frac{1}{2} \parallel HC - d \parallel_2^2 \tag{5.10}$$

where

$$H = \begin{bmatrix} h_1(A_1, B_1, \omega_1) & \cdots & h_n(A_1, B_1, \omega_1) \\ h_1(A_2, B_2, \omega_2) & \cdots & h_n(A_2, B_2, \omega_2) \\ \cdots & & \cdots \\ h_1(A_N, B_N, \omega_N) & \cdots & h_n(A_N, B_N, \omega_N) \end{bmatrix}, C = \begin{bmatrix} c_1 \\ c_2 \\ \cdots \\ c_n \end{bmatrix}, \text{and} \qquad d = \begin{bmatrix} d_1(A_1, B_1, \omega_1) \\ d_2(A_2, B_2, \omega_2) \\ \cdots \\ d_N(A_N, B_N, \omega_N) \end{bmatrix}$$

The above least-square optimization problem can be readily solved. In this work, the command *lsqnonlin* in Matlab is used to solve (5.10).

## 5.3 Controller Design

Aside from the nonlinear dynamics, the estimation of disturbances and model uncertainties and the mitigation of their impacts are important to achieving good control performance for soft

actuators. In this work, we propose the combination of inverse compensation, disturbance rejection, and feedback control to accommodate the system nonlinearity, inversion error, and unmodeled dynamics.

For the PVC gel actuator used in this study, the plant can be represented by a Hammerstein model, that is as a static nonlinearity ($f$) followed by a linear time-invariant (LTI) system (Fig 5.4 (a)). The nonlinearity can be compensated if the controller contains an inverse of the nonlinearity at its output end, in which case one could design $C(s)$ based on the dynamics $G(s)$. In this work, the command *finverse* in Matlab is used to compute the inverse of plant static nonlinearity ($f^{-1}$), and $C(s)$ is chosen to be a PID controller.

The design of the disturbance observer is based on the $Q$-filter and the plant model. The traditional disturbance observer [91] is designed as shown in Fig 5.5, where $G(s)$ represents the nominal model used for the controller design, $Q(s)$ is a stable filter, $u$ is the control input, $y$ is the system output, $y_r$ is the reference signal, $d$ is the lumped disturbance, and $\widehat{d_l}$ is the estimate of the lumped disturbance. With the approximate cancellation of the nonlinearity, one can represent the system as in Fig. 5.6.

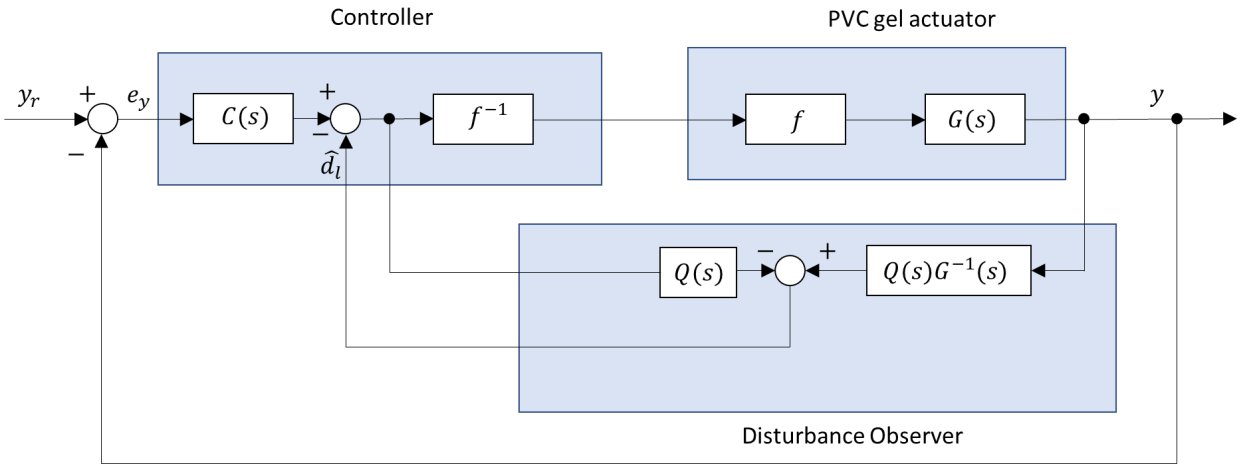


**Figure 5.5:** Proposed diagram of the inversion-based, disturbance-rejected, feedback control structure.

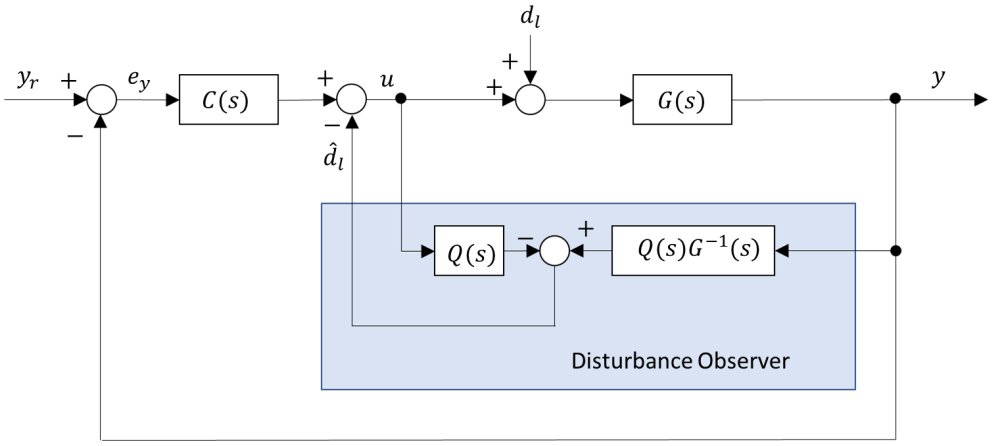


**Figure 5.6:** Diagram of the disturbance observer-based control structure.

The transfer functions from the reference $r$ and the disturbance $d_l$ to the output can be derived as

$$T_{ry}(s) = \frac{G(s)G(s)C(s)}{G_n(s)[1 + C(s)G_p(s)] + Q(s)[G_p(s) - G_n(s)]} \tag{5.11}$$

$$T_{dy}(s) = \frac{G_n(s)G_p(s)[1 - Q(s)]}{G_n(s)[1 + C(s)G_p(s)] + Q(s)[G_p(s) - G_n(s)]} \tag{5.12}$$

If $Q(s)$ is chosen as a low-pass filter with a steady-state gain of 1, i.e., $\lim_{\omega\to 0} Q(j\omega) = 1$, we can obtain

$$\lim_{\omega\to 0} T_{ry}(j\omega) = \lim_{\omega\to 0} \frac{G_n(j\omega)C(j\omega)}{1 + G_n(j\omega)C(j\omega)} \tag{5.13}$$

and

$$\lim_{\omega\to 0} T_{dy}(j\omega) = 0 \tag{5.14}$$

Assume that the transfer functions in (5.11) and (5.12) are stable. Then Eq. (5.13) implies that the real uncertain closed-loop system under the disturbance observer-based controller behaves as if it is the nominal closed-loop system in the absence of disturbance, which is also referred to as the

nominal performance recovery. It follows from (5.14) that the low-frequency disturbances can be attenuated asymptotically under the same scheme.

The performance of disturbance estimation is mainly determined by the design of low-pass filter $Q(s)$ that has to be designed such that the relative degree of $Q(s)$, should be no less than that of the model $G(s)$ to make sure that the control structure is realizable, i.e., $(Q(s)G^{-1}(s)$ should be proper).

## 5.4 Experimental Results

### 5.4.1 Model Validation

We evaluate the proposed modeling and parameter identification approach in Section 5.2 with experimental data collected on the setup shown in Fig. 5.3. Sinusoidal voltage inputs of three different amplitudes (300 V, 350 V, and 400 V), with three different DC biases of (400 V, 450 V, and 500 V), are applied to a PVC gel actuator. For each amplitude, inputs of 7 different frequencies, from 0.1 Hz to 10 Hz, are applied for 50 seconds. The corresponding actuator displacement is captured via the laser sensor. Using fast Fourier transform, we obtain the amplitude and the phase of the displacement at the input frequency, with which we further compute the overall system gain and phase shift for the given input amplitude, bias and frequency.

The measured (empirical) frequency response (both magnitude and phase responses) for the input with input amplitude of 300 V bias of and 450 V is used to identify the LTI component, $G(s)$. As shown in Fig. 5.7, the empirical response can be captured with a second-order system, identified with the Matlab function *tfest*:

$$G(s) = \frac{1146s + 1028}{s^2 + 17.11s + 8.761}$$

The nonlinear function $f$ is identified with different degrees for the polynomial, $n = 1, 2, 3$, and the corresponding identified parameters $c_i$ are listed in Table 5.2.

When $n = 1$, the nonlinear function $f$ degenerates to a linear relationship, and the resulting model is independent of the input amplitude and fails to capture the input-dependent dynamic

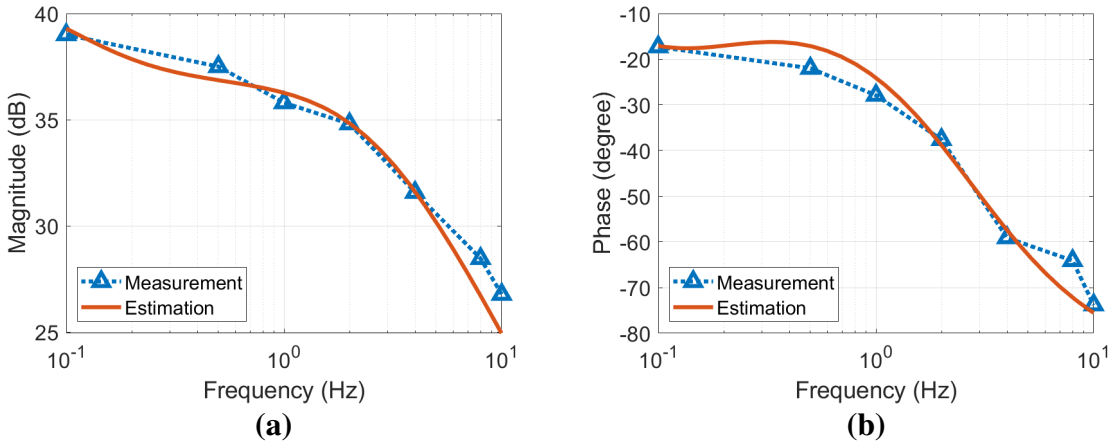


**Figure 5.7:** Measured frequency response of the PVC gel actuator for the amplitude of 300 V and bias of 450 V, and the frequency response of the identified linear model: (a) Magnitude plot; (b) phase plot.

behavior (Fig. 5.8). The model predictions for cases of $n = 2$ and $n = 3$ are shown in Fig. 5.9 and Fig. 5.10, respectively. Both models are able to capture the input-dependent dynamic behavior adequately; the model with $n = 3$ shows modest improvement over the model with $n = 2$, with the residual error norm in the least-squares estimation, Eq. (5.10), being 23% smaller than the case with $n = 2$. The phase plots for all models coincide with the one for $G(s)$ and are thus omitted for the cases of $n = 2$ and $n = 3$, and we note that the errors between the model-predicted phase and experimental measurements under different input amplitudes and biases are small in general as shown in Fig. 5.8 (b, d, and f).

**Table 5.2:** Calculated polynomial parameters.

| Polynomial | $c_1$ | $c_2$ | $c_3$ |
|---|---|---|---|
| $n = 1$ | 1.3664 | - | - |
| $n = 2$ | 0.1270 | $1.3057 \times 10^{-5}$ | - |
| $n = 3$ | 0.0721 | $2.1307 \times 10^{-5}$ | $-1.7231 \times 10^{-11}$ |

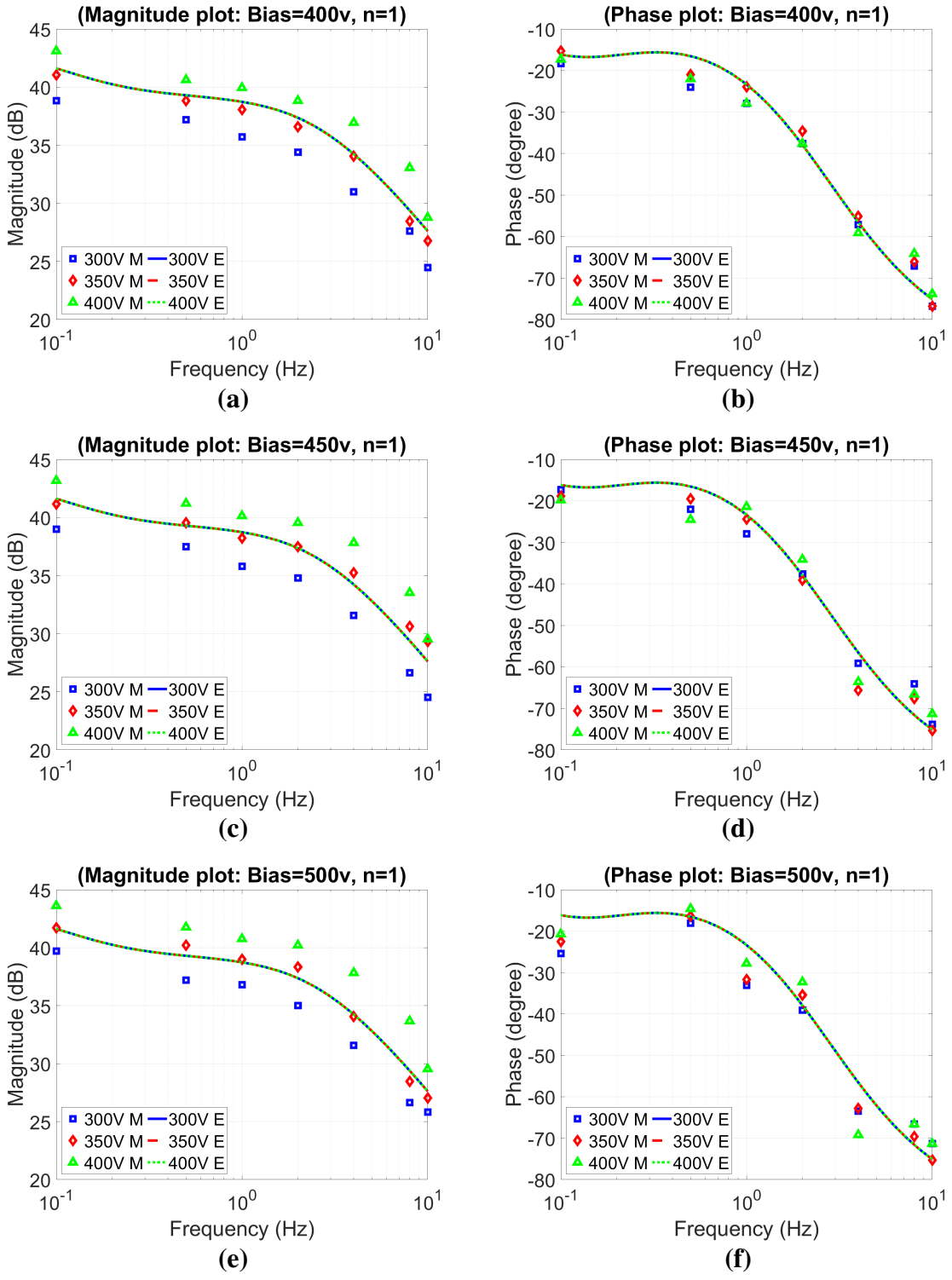


**Figure 5.8:** Comparison of measured magnitude and phase frequency responses with model-predicted frequency responses under different input amplitudes and biases ($n = 1$).

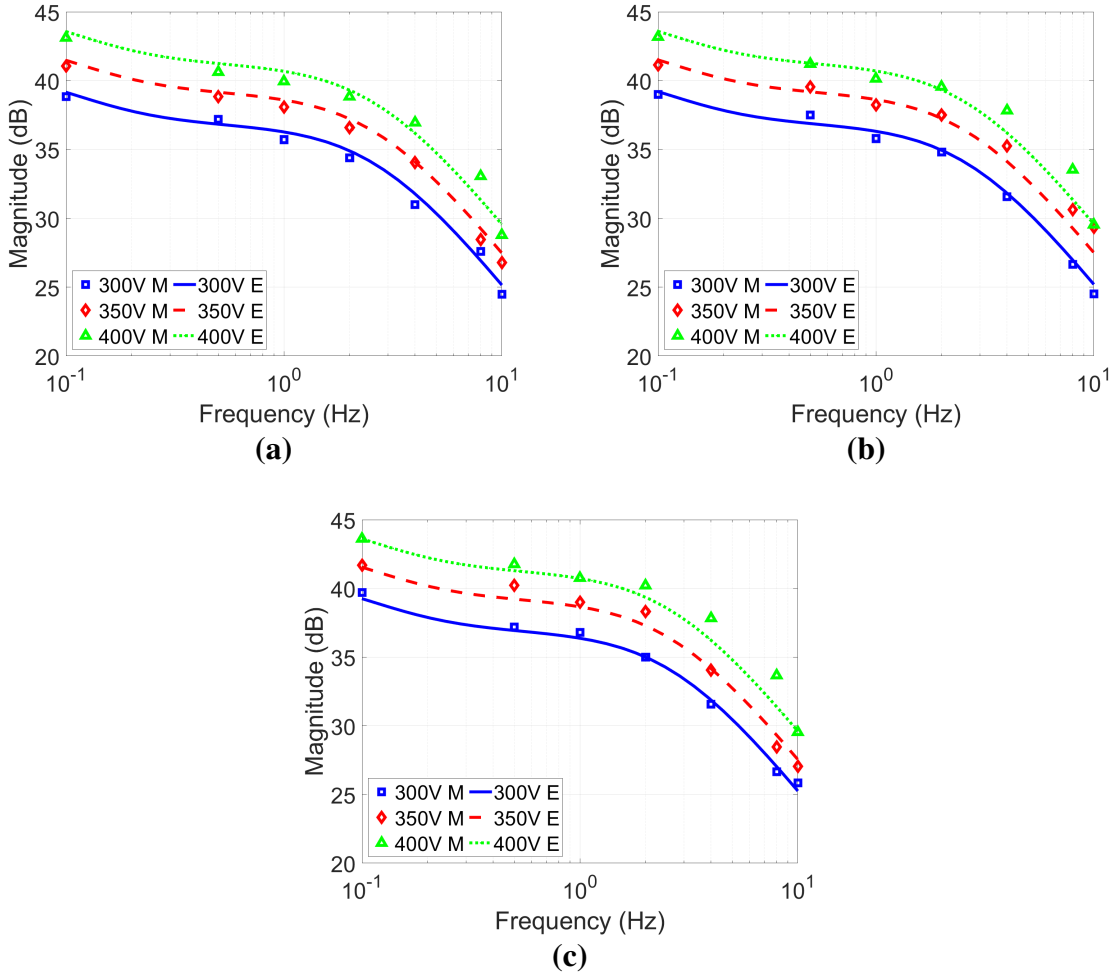


**Figure 5.9:** Comparison of measured magnitude responses at (a) bias = 400 V, (b) bias = 450 V, and (c) bias = 500 V with model-predicted frequency responses under different input amplitudes ($n = 2$).

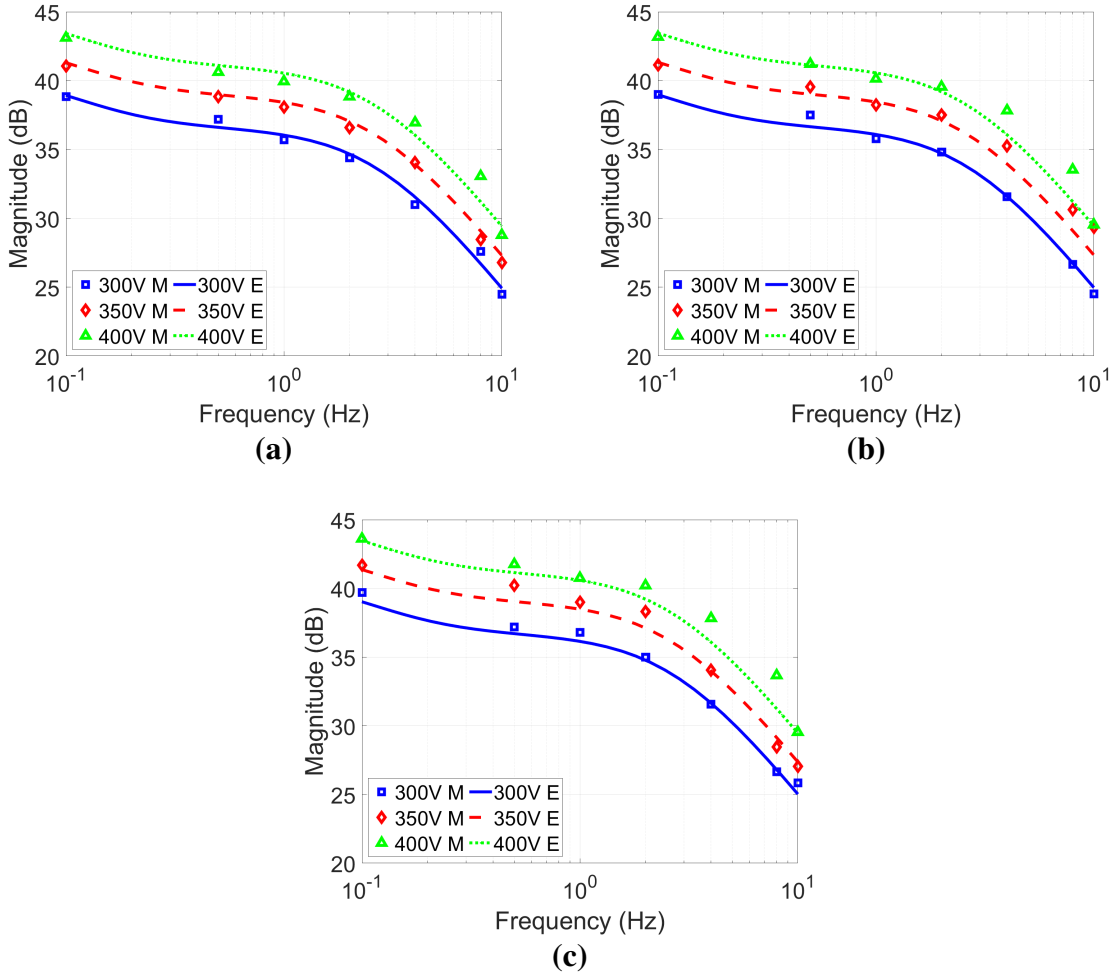


**Figure 5.10:** Comparison of measured magnitude responses at (a) bias = 400 V, (b) bias = 450 V, and (c) bias = 500 V with model-predicted frequency responses under different input amplitudes ($n = 3$).

The dynamic models are further validated with the measured time-domain data from experiment. Figs. 5.11, 5.12, 5.13 show the comparison of the measured actuator displacement and the model-predicted displacement at several different frequencies for different polynomial degrees ($n = 1, 2, 3$), for input amplitudes of 300 V, 350 V, and 400 V, respectively and bias of 450 V. These results show that, when $n = 1$ (linear model), the model is only able to predict well the displacement output under an input amplitude of 350 V, while the models with $n = 2$ and $n = 3$ are able to capture well the displacement at all three levels of input amplitude. With the negligible improvement from $n = 2$ to $n = 3$, it is determined that a model with $n = 2$ would be optimal in striking the trade-off

between model accuracy and complexity.

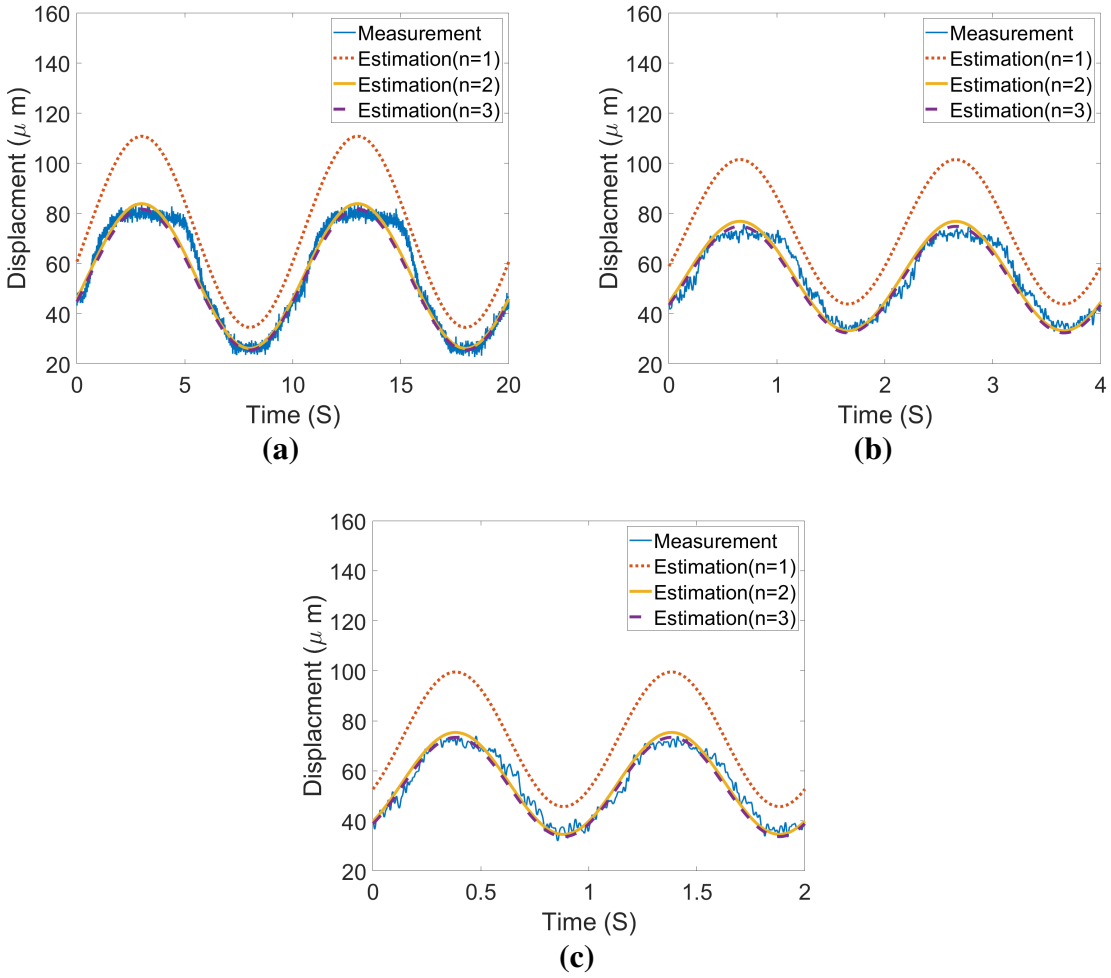


**Figure 5.11:** Model-predicted output (for $n = 1, 2, 3$) versus measured output for PVC gel actuator with input bias of 450V and amplitude of 300V: (a) 0.1 Hz, (B) 0.5 Hz, and (C) 1 Hz.

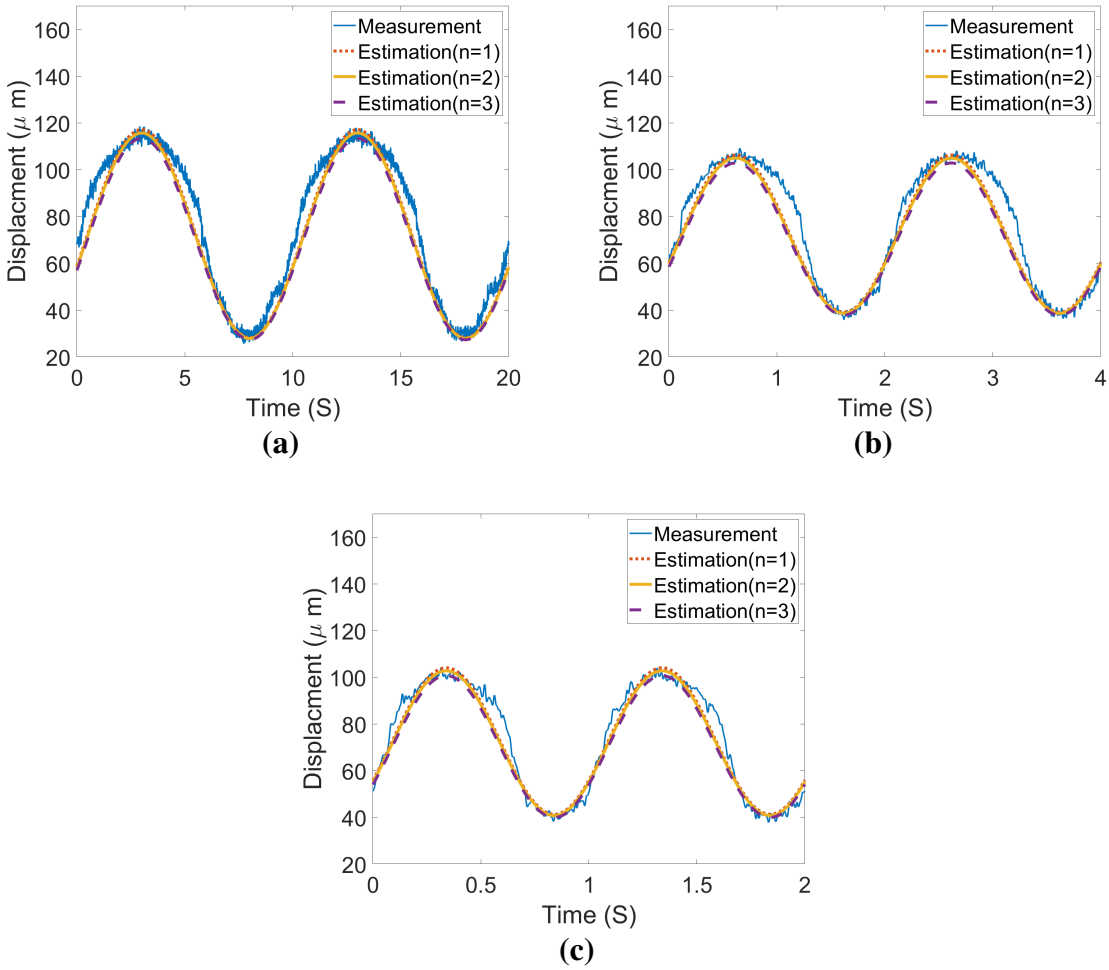


**Figure 5.12:** Model-predicted output (for $n = 1, 2, 3$) versus measured output for PVC gel actuator with input bias of 450 V and amplitude of 350 V: (a) 0.1 Hz, (B) 0.5 Hz, and (C) 1 Hz.

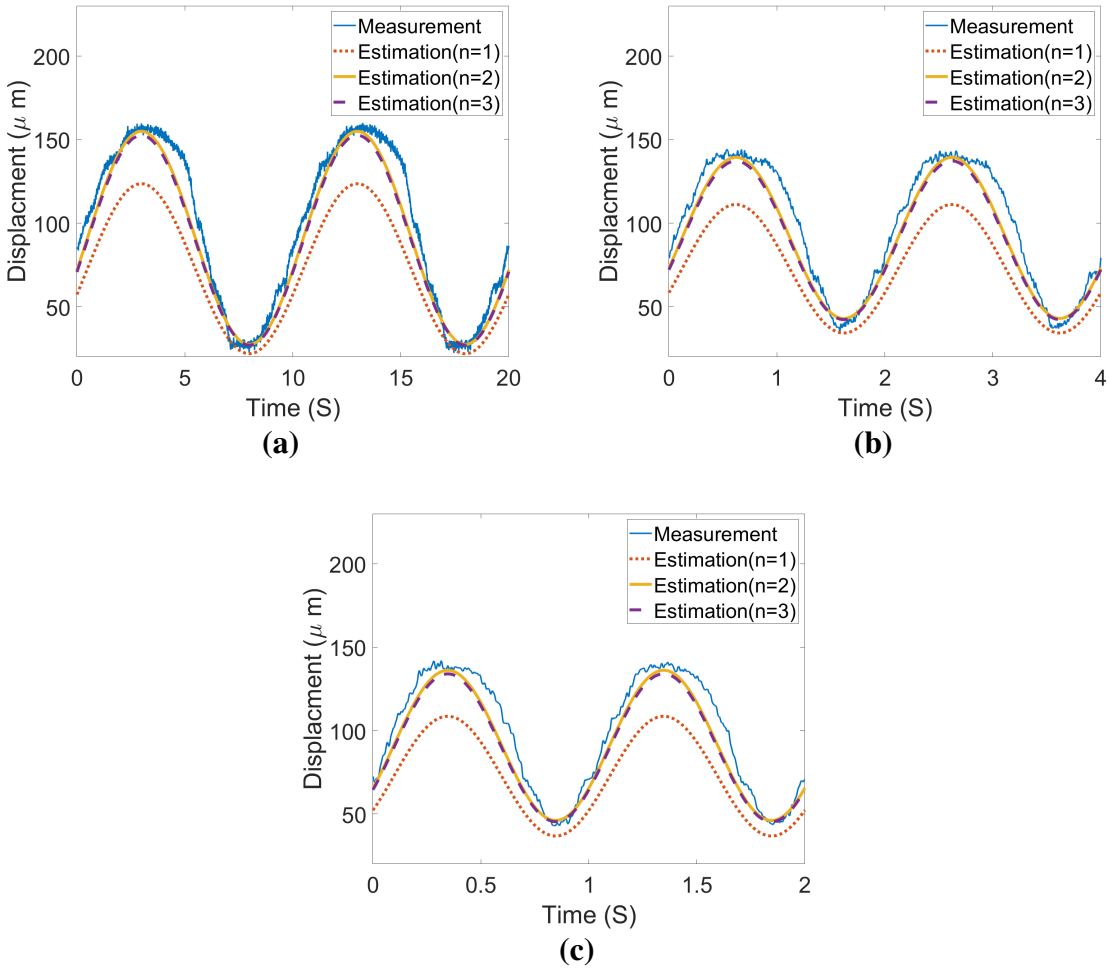


**Figure 5.13:** Model-predicted output (for $n = 1, 2, 3$) versus measured output for PVC gel actuator with input bias of 450 V and amplitude of 400 V: (a) 0.1 Hz, (B) 0.5 Hz, and (C) 1 Hz.

### 5.4.2 Control Experiments

To illustrate the feasibility and effectiveness of the proposed control scheme, several experiments are conducted using the experiment setup shown in Fig. 5.3. In our experiments, we test the proposed controller using two types of desired reference signals. The first one is a sinusoidal input defined as

$$y_{r1} = 100 + 25\sin(2\pi f t)\ \mu\text{ m}$$

and the second one is a multi-harmonic input defined as

$$y_{r2} = y_{ra} + y_{rb} + y_{rc}$$

where

$$y_{ra} = 33 + 5\sin(0.2\,\pi\, t)\ \mu\text{ m}$$

$$y_{rb} = 33 + 7\sin(\pi\, t)\ \mu\text{ m}$$

$$y_{rc} = 30 + 12\sin(2\,\pi\, t)\ \mu\text{ m}$$

For the first-type reference signal, we test it with three different frequencies = 0.1 Hz, 0.5 Hz, and 1 Hz. Three different control methods are implemented during the experiments, including a) a classical PID controller, b) inversion-based PID controller, and c) inversion-based PID controller combined with disturbance observer. The command *finverse* in Matlab is used to calculate the inverse of plant static nonlinearity Eq. (5.3). The PID controller gains are tuned with the Matlab PID tuner using the second–order system described in Section 5.4.1 and then refined through experiments runs to achieve good tracking performance. The filter $Q(s)$ can be selected as a first-order low-pass form with a steady-state gain of 1, and can be expressed as

$$Q(s) = \frac{1}{\lambda s + 1}$$

where $\lambda$ is the time constant of the first order low-pass filter with $\lambda > 0$. The estimated disturbance is obtained by the disturbance observer and then subtracted from the reference control command

**Table 5.3:** Mean tracking error under sinusoidal and Multi-Harmonic reference input for the proposed controller versus comparable methods.

| Method | PID | PID + inverse | PID + inverse + DOBC |
|---|---|---|---|
| Sinewave (0.1 Hz) | 0.6855 | 0.1308 | 0.0724 |
| Sinewave (0.5 Hz) | 1.0240 | 0.3112 | 0.1216 |
| Sinewave (1 Hz) | 0.9683 | 0.3791 | 0.1675 |
| Multi-Harmonic | 0.3945 | 0.1785 | 0.0789 |

to cancel or minimize the influences of the disturbance. A smaller filter parameter $\lambda$ will results a better transient dynamics in estimation and a smaller static disturbance estimation error, while a lager filter parameter will result in a larger disturbance estimation error [91]. In this work, $\lambda = 0.1$ was selected for the best disturbance rejection results.

Figures 5.14, 5.15, and 5.16, show a comparison between the achieved tracking error accuracy of our proposed approach and the errors under the two other control approaches for the sinusoidal reference. It can be noticed that the proposed controller outperforms the PID controller and the controller combining PID and inverse compensation (but without disturbance rejection). From Table 5.3, the average tracking error for 1 Hz reference signal is reduced by (60.84 %) from PID to inverse/PID, and by (82.7 %) from PID to inverse/PID/disturbance-rejection.

In the final set of experiments, the tracking of a multi-harmonic signal is implemented. As seen from Fig. 5.17 (e), the PVC gel output tracks the reference signal very well for proposed scheme. The inverse/PID/disturbance-rejection tracking error at the steady state is again lower than the other two control methods as shown in Table 5.3.

## 5.5 Conclusion

In this chapter, we demonstrated the feasibility of a data-driven modeling approach to capture the nonlinear dynamics of PVC gel actuators. The model, which is of Hammerstein-type, consists of a polynomial nonlinearity preceding a linear system. The empirical frequency response of the actuator at a relatively low input amplitude was used to estimate the linear system, and the coefficients of the polynomial nonlinearity were determined via a least-squares minimization procedure. The proposed model was able to predict the experimentally observed dynamic responses under inputs of different

amplitudes and biases. Finally, a trajectory-tracking controller was designed to cancel the the nonlinearity and to mitigate the influence of model uncertainties and disturbances. Experimental results have shown that the proposed controller outperforms two other different control schemes.

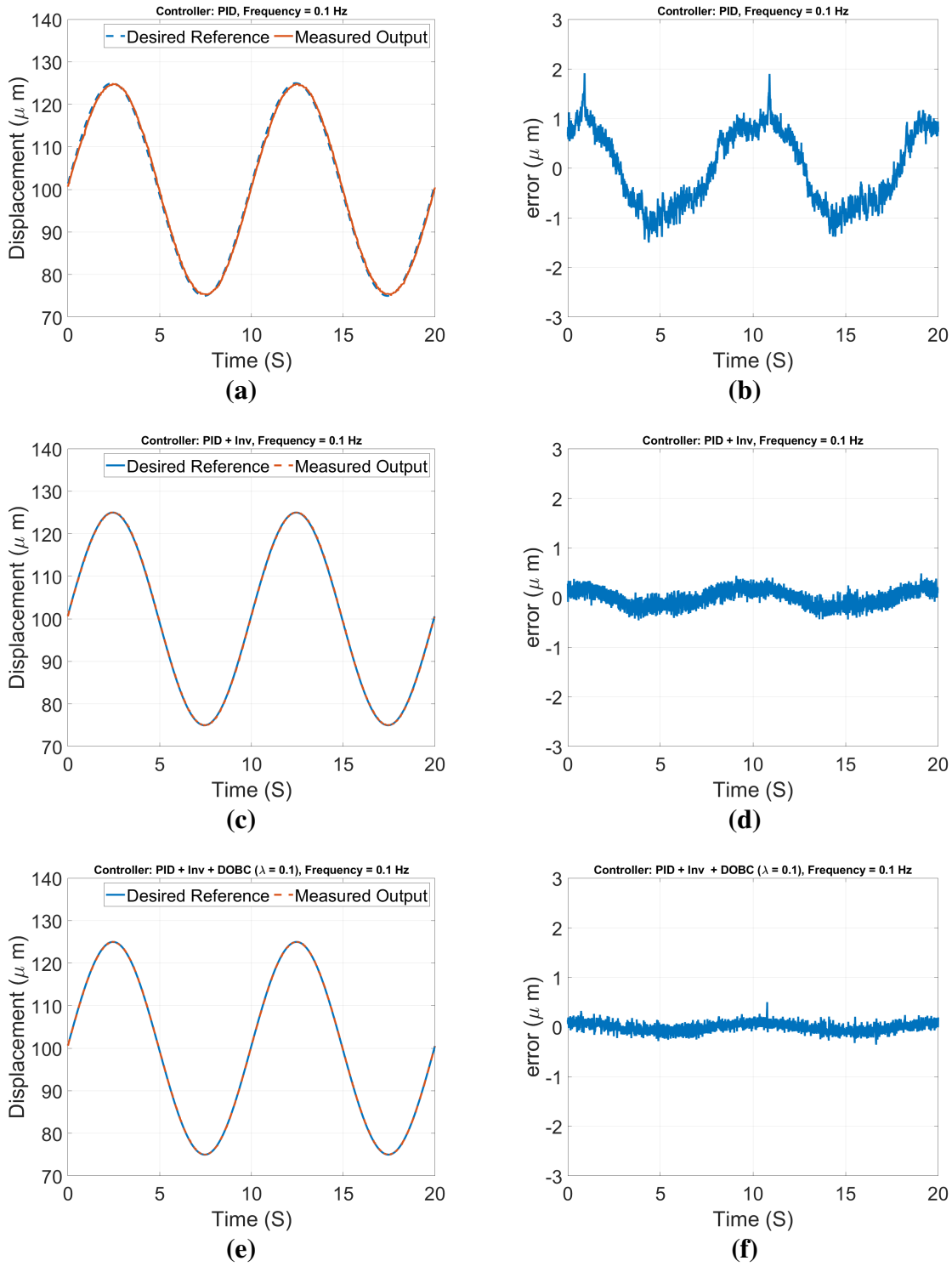


**Figure 5.14:** Measured displacement versus 0.1 Hz reference and tracking error using (a,b) PID, (c,d) PID+inversion , and (e,f) PID+inversion+DOB controller.

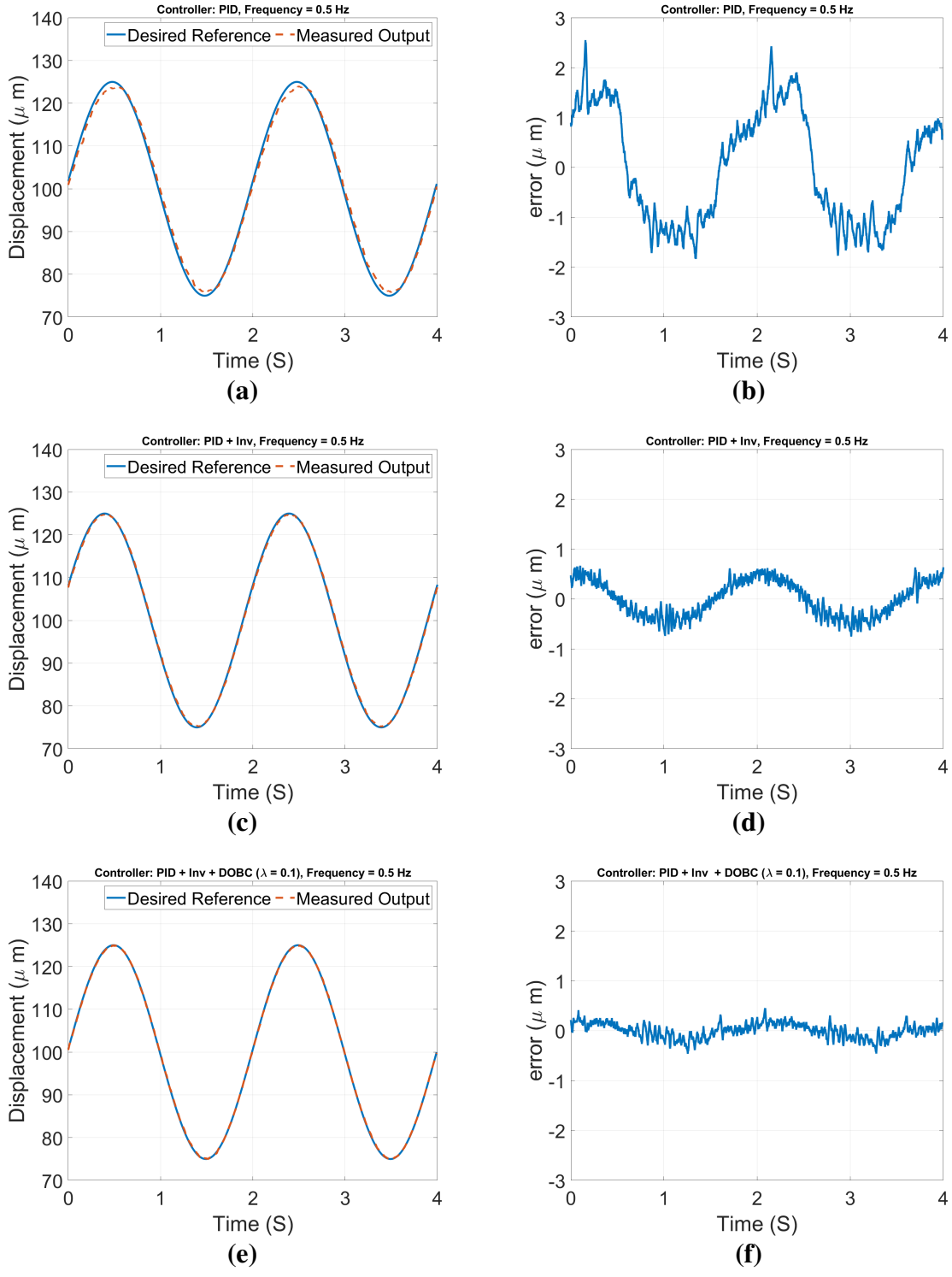


**Figure 5.15:** Measured displacement versus 0.5 Hz reference and tracking error using (a,b) PID, (c,d) PID+inversion , and (e,f) PID+inversion+DOB controller.

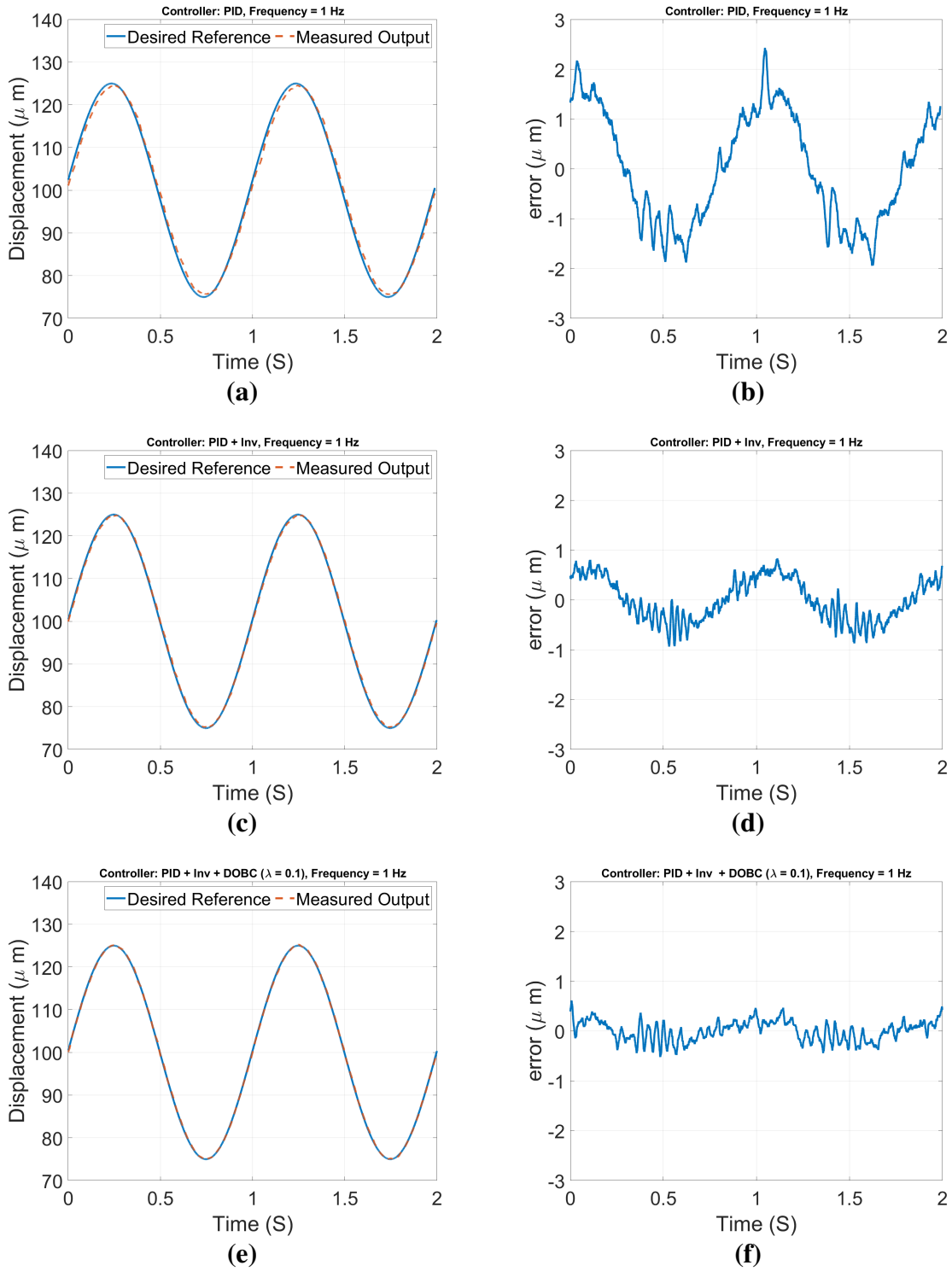


**Figure 5.16:** Measured displacement versus 1 Hz reference and tracking error using (a,b) PID, (c,d) PID+inversion , and (e,f) PID+inversion+DOB controller.

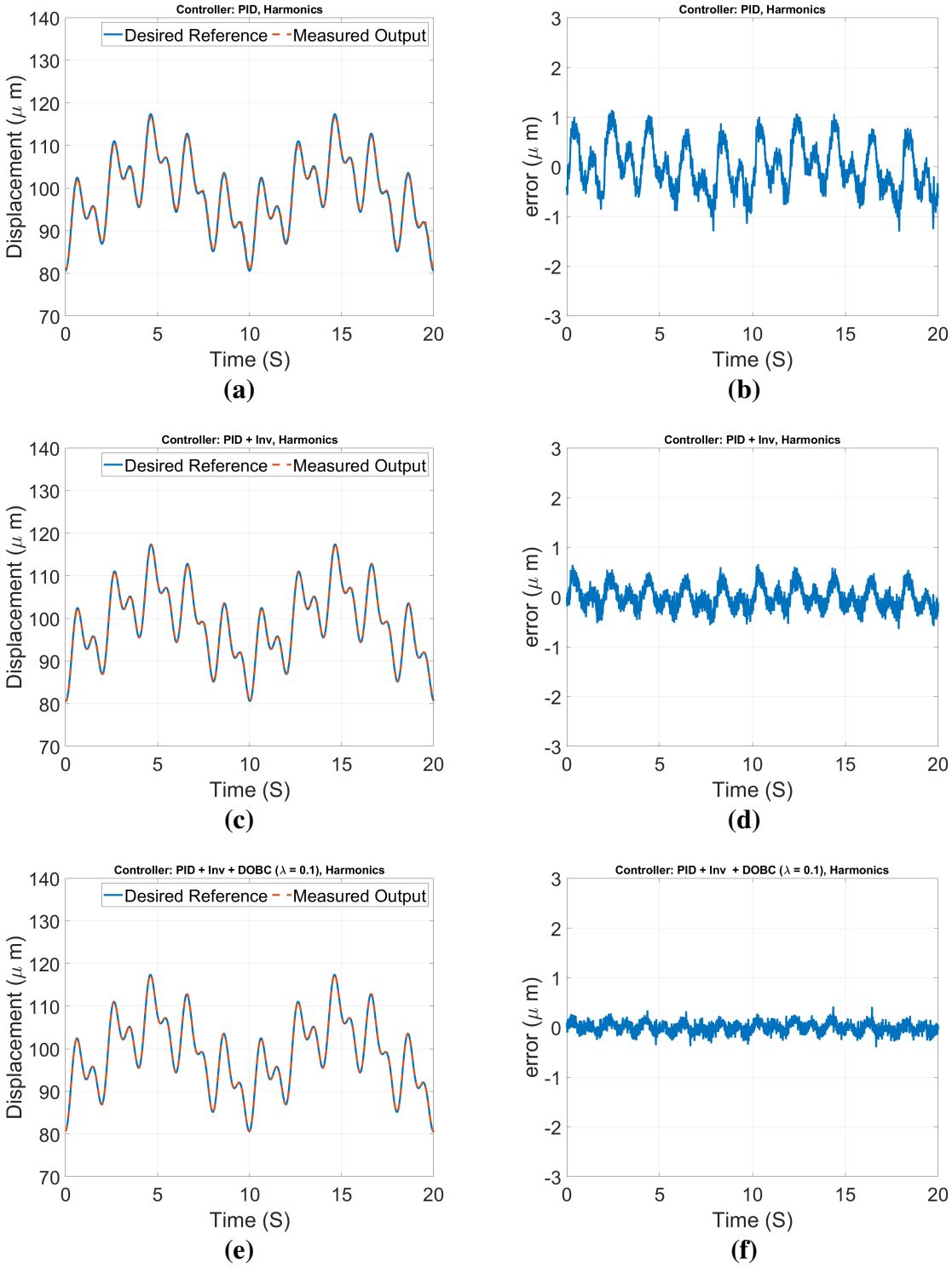


**Figure 5.17:** Measured displacement versus multi-harmonic wave desired reference and tracking error using (a,b) PID, (c,d) PID+inversion , and (e,f) PID+inversion+DOB controller.

# CHAPTER 6

# CONCLUSION AND FUTURE WORK

## 6.1 Conclusion

This work aims to explore new solutions to variable stiffness, embedded sensing, and actuation control for soft robotic systems. It tackles several key challenges in soft robotics.

Selective stiffness modulation is highly desirable for soft robots since it will allow for more controllable and versatile performance in practical applications. In this work, a novel approach to stiffness control of soft actuators was achieved using a conductive PLA material conveniently printed with an FDM 3D printer. The stiffness of CPLA can be modulated by simply applying electrical power to areas of interest. The basic thermomechanical and electrical properties of 3D-printed CPLA was investigated experimentally. The results were then used in FEM simulation of a SPA embedded with CPLA, where three hinges (places where electrical voltage could be applied) were used throughout the paper as a case study. The simulation results on the bending behavior of the actuator showed good match with experimental measurements conducted on a prototype.

In this work we also reported 3D-printed stretchable sensors with application to wind sensing. Among the three explored conductive materials, ETPU was shown to be most promising due to its larger strain range and higher sensitivity. In particular, ETPU-based sensors show a wide workable strain range, and high sensitivity. This strain sensor provides the advantages of low cost, simplicity in fabrication, robust mechanical properties, and versatility in applications. Its ability in measuring the wind velocity inside a wind tunnel was demonstrated, where the sensor showed sensitivity to the wind velocity beyond 3.5 m/s. The mechanical characterization results were then used in FEM simulation of the 3D-printed stretchable sensor, where FSI simulation was used to couple the wind load with the mechanical deformation of the sensor. The simulation results on the elastic strain behavior of the sensor showed good match with experimental measurements conducted on a prototype in the wind tunnel experiment. We also reported the fabrication of flexible strain sensors

with application to the monitoring of inflatable structures. Velostat was shown to be most promising due to its kink sensing range and high sensitivity. This strain sensor provides the advantages of low cost, simplicity in fabrication, and strain cycle stability. Its ability in detecting kink position and magnitude was demonstrated.

Finally, we have developed a framework for identifying a nonlinear dynamic model of a PVC gel actuator and used it to design an effective controller. The approach adopts a Hammerstein model structure and uses the describing function methodology to identify the nonlinear element of the model. It was shown that the proposed model, with a polynomial consisting of linear and cubic terms preceding an LTI system, was able to capture the actuator's measured responses under different input amplitudes and biases. Furthermore, a DOB-based control structure was proposed using a low pass filter to estimate and attenuate the lumped disturbances and model uncertainty. The effectiveness of the control scheme was supported by experimental results.

## 6.2 Future Work

In closing, soft robotics systems represent an exciting new paradigm in robotics that has the potential to revolutionize practices in society and industry. The work presented in this dissertation can be expanded in different directions.

First, for the SPA with tunable stiffness, it would be interesting to investigate a closed-loop control of the hinge stiffness, through the control of electrical voltages at different hinges, to achieve a more arbitrary desired shape for the SPA under a fixed pressure input. The feedback could be provided by integrating miniature temperature sensors at the hinge locations or potentially exploiting the strain sensing capability of CPLA. In addition, it will be of interest to examine the joint control of the pressure input and the electrical inputs, to realize an even broader range of shape changes. In addition, in this work grasping was only used as a proof of concept for the CPLA-enabled shape control. Another direction of our future work is to examine the optimal activation of CPLA-enabled finger joints for handling different objects.

Second, in terms of the 3D-printed strain gauges, it will be of interest to conduct additional

mechanical characterization and scanning electron microscopy experiments to understand the particular strain-resistivity behavior of ETPU material. The wind-sensing behavior of the material can be further studied to measure both wind direction and velocity via wind tunnel experiments and finite-element modeling, based on which the optimal design of the sensor in terms of dimensions and geometry could be pursued. In another direction, it would be interesting to explore different sensor geometries for detecting other deformations (wrinkles and bending angle). The optimal design of the sensor in terms of geometry and material will be further studied with finite element modeling (FEM) and experiments.

**BIBLIOGRAPHY**

# BIBLIOGRAPHY


[1] Mohammed Al-Rubaiai, Thassyo Pinto, David Torres, Nelson Sepulveda, and Xiaobo Tan. Characterization of a 3D-printed conductive PLA material with electrically controlled stiffness. In *ASME Conference on Smart Materials, Adaptive Structures and Intelligent Systems, 2017*, pages 302–309. American Society of Mechanical Engineers, 2017.

[2] Daniela Rus and Michael T Tolley. Design, fabrication and control of soft robots. *Nature*, 521(7553):467–475, 2015.

[3] Sebastian Wolf and Gerd Hirzinger. A new variable stiffness design: Matching requirements of the next robot generation. In *IEEE International Conference on Robotics and Automation, 2008.*, pages 1741–1746. IEEE, 2008.

[4] Gill A Pratt and Matthew M Williamson. Series elastic actuators. In *International Conference on Intelligent Robots and Systems, 1995*, volume 1, pages 399–406. IEEE, 1995.

[5] Yanqing Liu, Hiroshi Matsuhisa, and Hideo Utsuno. Semi-active vibration isolation system with variable stiffness and damping control. *Journal of Sound and Vibration*, 313(1-2):16–28, 2008.

[6] Nadia G Cheng, Maxim B Lobovsky, Steven J Keating, Adam M Setapen, Katy I Gero, Anette E Hosoi, and Karl D Iagnemma. Design and analysis of a robust, low-cost, highly articulated manipulator enabled by jamming of granular media. In *IEEE International Conference on Robotics and Automation, 2012*, pages 4328–4333. IEEE, 2012.

[7] Xingliang Fan, Lu Zhu, Ke Wang, Bingjie Wang, Yaozu Wu, Wei Xie, Chengyu Huang, Barbara Pui Chan, and Yanan Du. Stiffness-controlled thermoresponsive hydrogels for cell harvesting with sustained mechanical memory. *Advanced Healthcare Materials*, 6(5):1–10, 2017.

[8] M Andy McEvoy and Nikolaus Correll. Thermoplastic variable stiffness composites with embedded, networked sensing, actuation, and control. *Journal of Composite Materials*, 49(15):1799–1808, 2015.

[9] Chaoqun Xiang, Maria Elena Giannaccini, Theo Theodoridis, Lina Hao, Samia Nefti-Meziani, and Steven Davis. Variable stiffness Mckibben muscles with hydraulic and pneumatic operating modes. *Advanced Robotics*, 30(13):889–899, 2016.

[10] Lionel Pournin, Michel Tsukahara, and Th M Liebling. Particle shape versus friction in jamming. In *American Institute of Physics Conference Proceedings, 2009*, volume 1145, pages 499–502. AIP, 2009.

[11] Arjo J Loeve, Oscar S van de Ven, Johan G Vogel, Paul Breedveld, and Jenny Dankelman. Vacuum packed particles as flexible endoscope guides with controllable rigidity. *Granular Matter*, 12(6):543–554, 2010.

[12] Eric Brown, Nicholas Rodenberg, John Amend, Annan Mozeika, Erik Steltz, Mitchell R Zakin, Hod Lipson, and Heinrich M Jaeger. Universal robotic gripper based on the jamming of granular material. *Proceedings of the National Academy of Sciences*, 107(44):18809–18814, 2010.

[13] Yong-Jae Kim, Shanbao Cheng, Sangbae Kim, and Karl Iagnemma. Design of a tubular snake-like manipulator with stiffening capability by layer jamming. In *International Conference on Intelligent Robots and Systems, 2012*, pages 4251–4256. IEEE, 2012.

[14] Yong-Jae Kim, Shanbao Cheng, Sangbae Kim, and Karl Iagnemma. A novel layer jamming mechanism with tunable stiffness capability for minimally invasive surgery. *IEEE Transactions on Robotics*, 29(4):1031–1042, 2013.

[15] Thomas P Chenal, Jennifer C Case, Jamie Paik, and Rebecca K Kramer. Variable stiffness fabrics with embedded shape memory materials for wearable applications. In *International Conference on Intelligent Robots and Systems, 2014*, pages 2827–2831. IEEE, 2014.

[16] Yang Yang, Yonghua Chen, Yingtian Li, Michael ZQ Chen, and Ying Wei. Bioinspired robotic fingers based on pneumatic actuator and 3D printing of smart material. *Soft Robotics*, 4(2):147–162, 2017.

[17] Yang Yang, Yonghua Chen, Yingtian Li, Zheng Wang, and Yunquan Li. Novel variable-stiffness robotic fingers with built-in position feedback. *Soft Robotics*, 4(4):338–352, 2017.

[18] Wanliang Shan, Stuart Diller, Abbas Tutcuoglu, and Carmel Majidi. Rigidity-tuning conductive elastomer. *Smart Materials and Structures*, 24(6):065001, 2015.

[19] Al L Window. *Strain Gauge Technology*. Springer, 1992.

[20] Peter C Chang, Alison Flatau, and SC Liu. Health Monitoring of civil infrastructure. *Structural Health Monitoring*, 2(3):257–267, 2003.

[21] Derek Barke and WK Chiu. Structural health monitoring in the railway industry: a review. *Structural Health Monitoring*, 4(1):81–93, 2005.

[22] Yan Wang, Li Wang, Tingting Yang, Xiao Li, Xiaobei Zang, Miao Zhu, Kunlin Wang, Dehai Wu, and Hongwei Zhu. Wearable and highly sensitive graphene strain sensors for human motion monitoring. *Advanced Functional Materials*, 24(29):4666–4670, 2014.

[23] Bridget J Munro, Toni E Campbell, Gordon G Wallace, and Julie R Steele. The intelligent knee sleeve: A wearable biofeedback device. *Sensors and Actuators B: Chemical*, 131(2):541–547, 2008.

[24] Hideo D Kubo and Bruce C Hill. Respiration gated radiotherapy treatment: a technical study. *Physics in Medicine & Biology*, 41(1):83–91, 1996.

[25] Sumit Majumder, Tapas Mondal, and M Deen. Wearable sensors for remote health monitoring. *Sensors*, 17(1):130–137, 2017.

[26] Joo Chuan Yeo, Hong Kai Yap, Wang Xi, Zhiping Wang, Chen-Hua Yeow, and Chwee Teck Lim. Flexible and stretchable strain sensing actuator for wearable soft robotic applications. *Advanced Materials Technologies*, 1(3):160–169, 2016.

[27] Taekyoung Kim and Yong-Lae Park. A soft three-axis load cell using liquid-filled three-dimensional microchannels in a highly deformable elastomer. *IEEE Robotics and Automation Letters*, 3(2):881–887, 2018.

[28] Yong-Lae Park, Bor-Rong Chen, and Robert J Wood. Design and fabrication of soft artificial skin using embedded microchannels and liquid conductors. *IEEE Sensors Journal*, 12(8):2711–2718, 2012.

[29] Shanshan Yao and Yong Zhu. Wearable multifunctional sensors using printed stretchable conductors made of silver nanowires. *Nanoscale*, 6(4):2345–2352, 2014.

[30] Jackson Wirekoh and Yong-Lae Park. Design of flat pneumatic artificial muscles. *Smart Materials and Structures*, 26(3):35–44, 2017.

[31] Laura Paez, Gunjan Agarwal, and Jamie Paik. Design and analysis of a soft pneumatic actuator with origami shell reinforcement. *Soft Robotics*, 3(3):109–119, 2016.

[32] Dongjun Shin, Irene Sardellitti, Yong-Lae Park, Oussama Khatib, and Mark Cutkosky. Design and control of a bio-inspired human-friendly robot. *The International Journal of Robotics Research*, 29(5):571–584, 2010.

[33] Juan Miguel Àlvarez Palacio, Alain Riwan, Nazih Mechbal, Eric Monteiro, and Sébastien Voisembert. A novel inflatable actuator for inflatable robotic arms. In *International Conference on Advanced Intelligent Mechatronics (AIM), 2017*, pages 88–93. IEEE, 2017.

[34] Tommaso Ranzani, Giada Gerboni, Matteo Cianchetti, and A Menciassi. A bioinspired soft manipulator for minimally invasive surgery. *Bioinspiration & Biomimetics*, 10(3):44–53, 2015.

[35] Joseph D Greer, Tania K Morimoto, Allison M Okamura, and Elliot W Hawkes. Series pneumatic artificial muscles (sPAMs) and application to a soft continuum robot. In *International Conference on Robotics and Automation (ICRA), 2017*, pages 5503–5510. IEEE, 2017.

[36] Yong-Lae Park, Bor-rong Chen, Néstor O Pérez-Arancibia, Diana Young, Leia Stirling, Robert J Wood, Eugene C Goldfield, and Radhika Nagpal. Design and control of a bio-inspired soft wearable robotic device for ankle–foot rehabilitation. *Bioinspiration & Biomimetics*, 9(1):160–167, 2014.

[37] Yong-Lae Park, Jobim Santos, Kevin G Galloway, Eugene C Goldfield, and Robert J Wood. A soft wearable robotic device for active knee motions using flat pneumatic artificial muscles. In *International Conference on Robotics and Automation (ICRA), 2014*, pages 4805–4810. IEEE, 2014.

[38] Yiğit Mengüç, Yong-Lae Park, Hao Pei, Daniel Vogt, Patrick M Aubin, Ethan Winchell, Lowell Fluke, Leia Stirling, Robert J Wood, and Conor J Walsh. Wearable soft sensing suit for human gait measurement. *The International Journal of Robotics Research*, 33(14):1748–1764, 2014.

[39] Preston Ohta, Luis Valle, Jonathan King, Kevin Low, Jaehyun Yi, Christopher G Atkeson, and Yong-Lae Park. Design of a lightweight soft robotic arm using pneumatic artificial muscles and inflatable sleeves. *Soft Robotics*, 5(2):204–215, 2018.

[40] Ronghuai Qi, Amir Khajepour, William W Melek, Tin Lun Lam, and Yangsheng Xu. Design, kinematics, and control of a multijoint soft inflatable arm for human-safe interaction. *IEEE Transactions on Robotics*, 33(3):594–609, 2017.

[41] Elliot W Hawkes, Laura H Blumenschein, Joseph D Greer, and Allison M Okamura. A soft robot that navigates its environment through growth. *Science Robotics*, 2(8):392–400, 2017.

[42] Michael Andrew McEvoy and Nikolaus Correll. Materials that couple sensing, actuation, computation, and communication. *Science*, 347(6228):126–133, 2015.

[43] John O'Donnell, Farzad Ahmadkhanlou, Hwan-Sik Yoon, and Gregory Washington. All-printed smart structures: a viable option? In *Active and Passive Smart Structures and Integrated Systems*, volume 9057, pages 905–912. International Society for Optics and Photonics, 2014.

[44] Jesse Burstyn, Nicholas Fellion, Paul Strohmeier, and Roel Vertegaal. Printput: Resistive and capacitive input widgets for interactive 3D prints. In *IFIP Conference on Human-Computer Interaction*, pages 332–339. Springer, 2015.

[45] Hyouk Ryeol Choi, Kwangmok Jung, Sungmoo Ryew, Jae-Do Nam, Jaewook Jeon, Ja Choon Koo, and Kazuo Tanie. Biomimetic soft actuator: design, modeling, control, and applications. *IEEE/ASME Transactions on Mechatronics*, 10(5):581–593, 2005.

[46] Montassar Aidi Sharif, Hong Lei, Mohammed Khalid Al-Rubaiai, and Xiaobo Tan. Ionic polymer-metal composite torsional sensor: physics-based modeling and experimental validation. *Smart Materials and Structures*, 27(7):075039 (9 pp), 2018.

[47] Yi Li and Minoru Hashimoto. Design and prototyping of a novel lightweight walking assist wear using PVC gel soft actuators. *Sensors and Actuators A: Physical*, 239:26–44, 2016.

[48] Taeseon Hwang, Zachary Frank, Justin Neubauer, and Kwang Jin Kim. High-performance polyvinyl chloride gel artificial muscle actuator with graphene oxide and plasticizer. *Scientific Reports*, 9(1):1–9, 2019.

[49] A Furuse and M Hashimoto. Development of novel textile and yarn actuators using plasticized PVC gel. In *Electroactive Polymer Actuators and Devices (EAPAD)*, volume 10163, page 1016327 (11pp). International Society for Optics and Photonics, 2017.

[50] Yi Li, Mingfei Guo, and Yanbiao Li. Recent advances in plasticized PVC gels for soft actuators and devices: a review. *Journal of Materials Chemistry C*, 7(42):12991–13009, 2019.

[51] Mohammad Ali, Takamitsu Ueki, Daijiro Tsurumi, and Toshihiro Hirai. Influence of plasticizer content on the transition of electromechanical behavior of PVC gel actuator. *Langmuir*, 27(12):7902–7908, 2011.

[52] Toshihiro Hirai, Takafumi Ogiwara, Katsuya Fujii, Takamitsu Ueki, Ken Kinoshita, and Midori Takasaki. Electrically active artificial pupil showing amoeba-like pseudopodial deformation. *Advanced Materials*, 21(28):2886–2888, 2009.

[53] Yi Li, Yasuhiro Maeda, and Minoru Hashimoto. Lightweight, soft variable stiffness gel spats for walking assistance. *International Journal of Advanced Robotic Systems*, 12(12):175 (7pp), 2015.

[54] Won-Hyeong Park, Eun-Jae Shin, Yongjae Yoo, Seungmoon Choi, and Sang-Youn Kim. Soft haptic actuator based on knitted PVC gel fabric. *IEEE Transactions on Industrial Electronics*, 67(1):677–685, 2019.

[55] Won-Hyeong Park, Eun-Jae Shin, and Sang-Youn Kim. Enhanced design of a soft thin-film vibrotactile actuator based on pvc gel. *Applied Sciences*, 7(10):972 (12pp), 2017.

[56] Toshihiro Hirai, Mohammad Ali, Takafumi Ogiwara, Daijiro Tsurumi, Keiichi Yamamoto, Takamitsu Ueki, Hong Xia, and Minoru Hashimoto. Characteristic electrical actuation of plasticized poly (vinyl chloride): Various electrical functions in relation with the dielectric plasticizers. In *Advances in Science and Technology*, volume 79, pages 1–6. Trans Tech Publ, 2013.

[57] Hong Xia and Toshihiro Hirai. Space charge distribution and mechanical properties in plasticized PVC actuators. In *International Conference on Mechatronics and Automation*, pages 164–169. IEEE, 2009.

[58] Kinji Asaka and Minoru Hashimoto. Electrical properties and electromechanical modeling of plasticized PVC gel actuators. *Sensors and Actuators B: Chemical*, 273:1246–1256, 2018.

[59] Minami Shibagaki, Naoki Ogawa, and Minoru Hashimoto. Modeling of a contraction type PVC gel actuator. In *IEEE International Conference on Robotics and Biomimetics*, pages 1434–1439. IEEE, 2010.

[60] Yi Li and Minoru Hashimoto. PVC gel based artificial muscles: Characterizations and actuation modular constructions. *Sensors and Actuators A: Physical*, 233:246–258, 2015.

[61] Kinji Asaka and Minoru Hashimoto. Electromechanical modeling of plasticized PVC gel actuators and the improvement in their performances with the additions of ionic liquids. In *Electroactive Polymer Actuators and Devices (EAPAD) XXII*, volume 11375, page 1137511 (13pp). International Society for Optics and Photonics, 2020.

[62] Zachary Frank, Zakai Olsen, Taeseon Hwang, and Kwang J Kim. Modelling and experimental study for PVC gel actuators. In *Dynamic Systems and Control Conference*, volume 59162, page V003T20A007 (6pp). American Society of Mechanical Engineers, 2019.

[63] Bobak Mosadegh, Panagiotis Polygerinos, Christoph Keplinger, Sophia Wennstedt, Robert F Shepherd, Unmukt Gupta, Jongmin Shim, Katia Bertoldi, Conor J Walsh, and George M Whitesides. Pneumatic networks for soft robotics that actuate rapidly. *Advanced Functional Materials*, 24(15):2163–2170, 2014.

[64] Robin J Speedy. The hard sphere glass transition. *Molecular Physics*, 95(2):169–178, 1998.

[65] ISO Standard. 11357-2, 1999. *Plastics–Differential scanning calorimetry (DSC)–Part 2*.

[66] FS Senatov, KV Niaza, M Yu Zadorozhnyy, AV Maksimkin, SD Kaloshkin, and YZ Estrin. Mechanical properties and shape memory effect of 3D-printed PLA-based porous scaffolds. *Journal of the Mechanical Behavior of Biomedical Materials*, 57:139–148, 2016.

[67] SC Ma, HL Lin, and TL Yu. Glass transition temperature, free volume, and curing kinetics of unsaturated polyester. *Polymer Journal*, 25(9):897–907, 1993.

[68] Donald J Leo. *Engineering Analysis of Smart Material Systems*. John Wiley & Sons, 2007.

[69] Martin Rides, Angela Dawson, and Crispin Allen. Measurement of heat transfer coefficients for polymer processing simulation. *Polymeric Materials IAG, RAPRA*, 2007.

[70] Raymond William Ogden. Large deformation isotropic elasticity–on the correlation of theory and experiment for incompressible rubberlike solids. *Proceedings of the Royal Society of London. A. Mathematical and Physical Sciences, 1972*, 326(1567):565–584, 1972.

[71] Dónal P Holland, Evelyn J Park, Panagiotis Polygerinos, Gareth J Bennett, and Conor J Walsh. The soft robotics toolkit: Shared resources for research and design. *Soft Robotics*, 1(3):224–230, 2014.

[72] Mohammed Al-Rubaiai, Ryohei Tsuruta, Umesh Gandhi, Chuan Wang, and Xiaobo Tan. A 3D-printed stretchable strain sensor for wind sensing. *Smart Materials and Structures*, 28(8):265–274, 2019.

[73] Nanshu Lu, Chi Lu, Shixuan Yang, and John Rogers. Highly sensitive skin-mountable strain gauges based entirely on elastomers. *Advanced Functional Materials*, 22(19):4044–4050, 2012.

[74] Al L Window. *Strain Gauge Technology*. Springer, 1992.

[75] Ru Xie, Yunsong Xie, Carlos R López-Barrón, Kai-Zhong Gao, and Norman J Wagner. Ultra-stretchable conductive iono-elastomer and motion strain sensor system developed therefrom. *Technology & Innovation*, 19(3):613–626, 2018.

[76] Horacio De la Fuente, Jasen Raboin, Gerard Valle, and Gary Spexarth. TransHab-NASA's large-scale inflatable spacecraft. In *41st Structures, Structural Dynamics, and Materials Conference and Exhibit*, pages 182–192, 2000.

[77] Glen Brown, Roy Haggard, and Brook Norton. Inflatable structures for deployable wings. In *16th AIAA Aerodynamic Decelerator Systems Technology Conference and Seminar*, pages 206–214, 2001.

[78] Yuyang Song, Umesh Gandhi, and Azwan Aris. A baffled inflatable wing made from high performance textile materials: Design, analysis, and experiments. In *AIAA Scitech 2021 Forum*, pages 430–437, 2021.

[79] RE Freeland, GD Bilyeu, GR Veal, MD Steiner, and DE Carson. Large inflatable deployable antenna flight experiment results. *Acta Astronautica*, 41(4-10):267–277, 1997.

[80] Masoud Kalantari, Javad Dargahi, Jozsef Kövecses, Mahmood Ghanbari Mardasi, and Shahrzad Nouri. A new approach for modeling piezoresistive force sensors based on semi-conductive polymer composites. *IEEE/ASME Transactions on Mechatronics*, 17(3):572–581, 2011.

[81] R Berman and David Keith Chalmers Macdonald. The thermal and electrical conductivity of copper at low temperatures. *Proceedings of the Royal Society of London. Series A. Mathematical and Physical Sciences*, 211(1104):122–128, 1952.

[82] Robert Hudec, Slavomír Matúška, Patrik Kamencay, and Miroslav Benco. A smart IoT system for detecting the position of a lying person using a novel textile pressure sensor. *Sensors*, 21(1):206–212, 2021.

[83] Liyang Shen. *Real-time Mechanical and Mechano-electrical Behavior of Carbon Black Filled Films*. PhD thesis, University of Akron, 2015.

[84] Katharina Ehrmann. The forces necessary to remove adhesive tape from a horizontal surface. *International Young Physicists Tournament (IYPT)*, 33(1):122–131, 2011.

[85] Saivimal Sridar, Souvik Poddar, Yida Tong, Panagiotis Polygerinos, and Wenlong Zhang. Towards untethered soft pneumatic exosuits using low-volume inflatable actuator composites and a portable pneumatic source. *IEEE Robotics and Automation Letters*, 5(3):4062–4069, 2020.

[86] Xiang-Wu Zhang, Yi Pan, Qiang Zheng, and Xiao-Su Yi. Time dependence of piezoresistance for the conductor-filled polymer composites. *Journal of Polymer Science part B: Polymer Physics*, 38(21):2739–2749, 2000.

[87] F London. Planck's constant and low temperature transfer. *Reviews of Modern Physics*, 17(2):310–321, 1945.

[88] G Gräff, H Kalinowsky, and J Traut. A direct determination of the proton electron mass ratio. *Zeitschrift für Physik A Atoms and Nuclei*, 297(1):35–39, 1980.

[89] Andrius Dzedzickis, Ernestas Sutinys, Vytautas Bucinskas, Urte Samukaite-Bubniene, Baltramiejus Jakstys, Arunas Ramanavicius, and Inga Morkvenaite-Vilkonciene. Polyethylene-carbon composite (velostat®) based tactile sensor. *Polymers*, 12(12):2905–2915, 2020.

[90] Jean-Jacques E Slotine and Weiping Li. *Applied Nonlinear Control*, volume 199. Prentice hall Englewood Cliffs, NJ, 1991.

[91] Wen-Hua Chen, Jun Yang, Lei Guo, and Shihua Li. Disturbance-observer-based control and related methods—an overview. *IEEE Transactions on Industrial Electronics*, 63(2):1083–1095, 2015.